Thin zinc oxide and cuprous oxide films for photovoltaic applications

A DISSERTATION
SUBMITTED TO THE FACULTY OF THE GRADUATE SCHOOL
OF THE UNIVERSITY OF MINNESOTA
BY

SeongHo Jeong

IN PARTIAL FULFILLMENT OF THE REQUIREMENTS
FOR THE DEGREE OF
DOCTOR OF PHILOSOPHY

Eray S. Aydil, Advisor

August 2010

Acknowledgements

I give heartfelt thanks to all the people who gave me a great support during my time in Minnesota. I know it cannot be sufficient to express my thanks to them with words, but I believe they know my mind.

First of all, I am deeply thankful to my advisor Eray Aydil. He not only provided me a perfect support for my study but also showed me an endless passion for research and life. I am very proud of being his student.

I also would like to thank my wonderful colleagues, Mike, Janice, Kurtis, Emil, Will, Bin, Ankur, Selin, Boris, Neema, Melissa and Sriharsha. They always were willing to give me a hand and all the discussion with them was joyful and stimulated me. I cannot forget the help from the CEMS Korean students. They always supported me in and out of the school and gave me courage and support. The life in school was warm and cheerful because they were with me. I wish good luck to them all in their research.

I am also grateful to my friends and company colleagues, Inkyo, Yeonwoo, Seokho, Seokheon, Sungho. Although they are far from me, they always pray for me and show unchanged friendship. I am looking forward to seeing them all.

I have to express my appreciation to my family in Korea, parents, uncles, aunts, brothers and sisters for their love and support during my study. I could not repay their kindness.

Finally, I would like to give my deepest thanks to my wife, Sungshin and daughter, Seyoon. They are always behind me. This work would not be possible without their support and understanding. Thank you and love you.

Dedication

with love to my family

Abstract

Metal oxide semiconductors and heterojunctions made from thin films of metal oxide semiconductors have broad range of functional properties and high potential in optical, electrical and magnetic devices such as light emitting diodes, spintronic devices and solar cells. Among the oxide semiconductors, zinc oxide (ZnO) and cuprous oxide (Cu_2O) are attractive because they are inexpensive, abundant and nontoxic. As synthesized ZnO is usually an intrinsic n - type semiconductor with wide band gap (3.4 eV) and can be used as the transparent conducting window layer in solar cells. As synthesized Cu_2O is usually a p - type semiconductor with a band gap of 2.17 eV and has been considered as a potential material for the light absorbing layer in solar cells. I used various techniques including metal organic chemical vapor deposition, magnetron sputtering and atomic layer deposition to grow thin films of ZnO and Cu_2O and fabricated Cu_2O/ZnO heterojunctions. I specifically investigated the optical and electrical properties of Cu_2O thin films deposited on ZnO by MOCVD and showed that Cu_2O thin films grow as single phase with [110] axis aligned perpendicular to the ZnO surface which is (0001) plane and with in-plane rotational alignment due to $(220)_{Cu_2O} \parallel (0002)_{ZnO}$; $[001]_{Cu_2O} \parallel [1\bar{2}10]_{ZnO}$ epitaxy. Moreover, I fabricated solar cells based on these Cu_2O/ZnO heterojunctions and characterized them. Electrical characterization of these solar cells as a function of temperature between 100 K and 300 K under illumination revealed that interface recombination and tunneling at the interface are the factors that limit the solar cell performance. To date solar cells based on Cu_2O/ZnO heterojunctions had low open

circuit voltages (~ 0.3V) even though the expected value is around 1V. I achieved open circuit voltages approaching 1V at low temperature (~ 100 K) and showed that if interfacial recombination is reduced these cells can achieve their predicted potential.

Table of Contents

List of Tables

List of Figures

Chapter 1

Introduction

1.1 Cu_2O/ZnO heterojunction and solar cell application

Metal oxides exhibit a wide range of functional properties depending on their crystal structure and bonding between the metal cation and oxygen.[1,2] Indeed, the electrical properties of metal oxides range from insulating to highly conducting like a metal, or even superconducting. Some metal oxides also exhibit magnetic properties such as ferromagnetism or ferrimagnetism. Because of this diverse functionality, metal oxides have become one of the most fascinating inorganic materials in device applications such as light emitting diodes, field effect transistors, solar cells and spintronic devices.[3,4,5,6,7] Among the metal oxides, ZnO and Cu_2O are attractive because the metals are abundant on earth, inexpensive and non-toxic. Moreover, these oxides have useful optical and electrical properties suitable for a wide variety of electrical devices.

As synthesized ZnO is almost always an n-type semiconductor with high mobility (10 ~ 200 cm^2 / V sec) in thin high quality films at room temperature. ZnO is a wide band gap (3.3 eV)[8] semiconductor and therefore, it has been considered as a potential material

for transparent electrode and electronics[9,10] and widely used in solar cells as window layer and transparent thin film transistors.[11] As synthesized Cu_2O is a p-type semiconductor with band gap of 2.17 eV.[12] Although the band gap is larger than the theoretical optimum band gap (~ 1.5 eV)[13] for solar cells, Cu_2O has several advantages as a light absorbing layer in solar cells such as large absorption coefficient in the visible region (~ 10^4 cm^{-1}) and a long minority carrier diffusion length (1 ~ 4 μm).[14] Based on the fact that high quality Cu_2O can be fabricated by simple thermal oxidation at around 1000˚C from pure copper, there have been extensive studies to use Cu_2O in low cost photovoltaic power generation[15,16,17,18] for the several decades by simply forming a Cu-Cu_2O schottky junction but the overall efficiency has not reached above 2 % so far. Recently, thin film solar cells based on the heterojunction between p-type Cu_2O and n-type ZnO has received attention because of the successful demonstration of ZnO and Cu_2O thin film deposition by various methods such as molecular beam epitaxy (MBE),[19] sputtering,[20,21] chemical vapor deposition (CVD)[22] and electrochemical deposition.[23] The performance of thin film heterojunction solar cells depends on the electrical and optical properties of each layer which comprises the device and the quality of the interface between the films that form the junction. These critical properties in turn depend on the thin film deposition method and the deposition process conditions. Therefore, an in depth investigation of the relationship between the film properties and carrier transport mechanisms through the junction interface and the deposition process conditions is important and needed.

1.2 Review of relevant ZnO and Cu_2O properties

1.2.1 ZnO properties

ZnO is a II-VI semiconductor and crystallizes in three phases, wurtzite (hexagonal), zinc-blende (cubic) and rocksalt (cubic).[8] The stable phase under ambient conditions is wurtzite where each Zn cation atom is bonded with four O anion atoms which form the corners of a tetrahedron. Zinc-blende can be formed on cubic structured substrates and rocksalt can be made at high pressure (~ 100 kbar).[24] A schematic diagram of ZnO wurtzite crystal structure is shown in Figure 1.1 and selected fundamental properties of ZnO are listed in Table 1.1.[8,25]

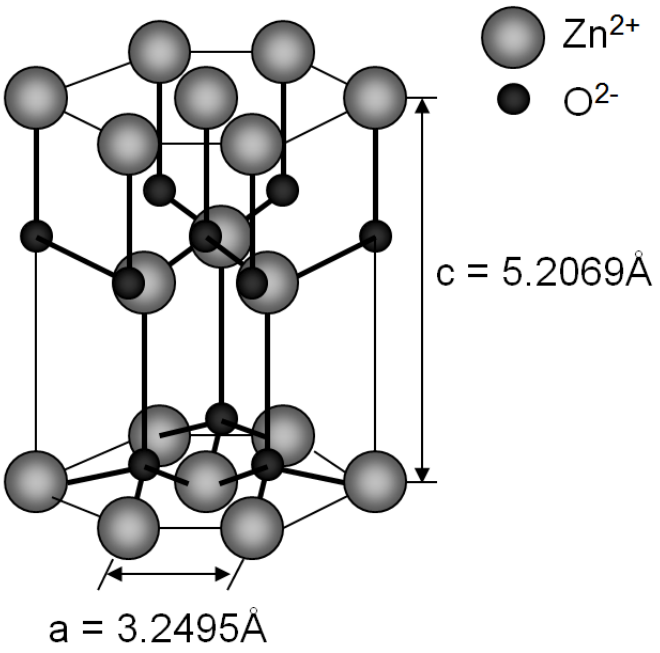

Figure 1.1. Hexagonal wurtzite crystal structures of ZnO.

ZnO is transparent in the visible region of electromagnetic spectrum and the absorption increases abruptly in the ultraviolet region for photon energies greater than 3.3 eV, the direct band gap energy. ZnO thin films are usually n-type even in the absence of intentional doping. It was reported that the main source of intrinsic donors are point defects such as oxygen vacancies or zinc interstitials[26] but recent calculations by Van de Walle shows that these kinds of defects form deep level donors which are hard to ionize and unlikely to donate electrons to the conduction band at room temperature. Van de Walle argued that the electrons originated from hydrogen impurities in ZnO and showed that H in ZnO is a shallow donor.[27] This debate is still unsettled but experimental fact is that exposing ZnO to hydrogen increases electron concentration whereas exposure to oxygen decreases it.[28]

Native donors such as oxygen vacancies, zinc interstitials and hydrogen in ZnO are unstable and their concentrations change with time and temperature. Concentrations of these native donors also depend on film deposition methods and processing conditions. To improve electrical properties of films and make them stable, intentional doping is used. The III or V elements in the periodic table can be used as n-type and p-type dopants for ZnO, respectively. For n-type doping B, Al, Ga and In etc. are used and for p-type doping N and P etc. are used. However, ZnO films almost always show n-type characteristic regardless of the type of dopants used.[29] The reason for this is that p-type dopant such as N and P is easily compensated by native defects.[30] So the difficulty in making a high quality p-type ZnO film remains a major obstacle for the widespread use of ZnO in opto-electronic device applications.

Table 1.1. Fundamental properties of ZnO. Unless indicated otherwise, all properties are at room temperature. "c" and "a" denote the [0001] and [1000] direction in hexagonal crystal structure, respectively.[8,25]

Properties	Values
Density (g/cm^3)	5.67
Melting point (K)	2242
Crystal structure	Wurtzite (Hexagonal) (Space group : $P6_3mc$ - C^4_{6v})
Lattice constant (Å)	a = 3.2495; c = 5.2069
Band gap (eV)	3.3 (Direct)
Electron Hall mobility (cm^2/V sec)	$\mu_{n\perp c}$ = 70 (film); $\mu_{n\perp c}$ = 150 (bulk); $\mu_{n\|c}$ = 170 (bulk)
Dielectric Constant	$\varepsilon_{(0)\perp c}$ = 7.8; $\varepsilon_{(\infty)\perp c}$ = 3.7; $\varepsilon_{(0)\|c}$ = 8.75; $\varepsilon_{(\infty)\|c}$ = 3.75

1.2.2 Cu_2O properties

Copper oxide has two stable phases, cuprous oxide (Cu_2O) and cupric oxide (CuO). The Cu_2O phase has reddish color with direct band gap of 2.17 eV and CuO has dark gray color with an indirect band gap of 1.4 eV. The property difference between Cu_2O and CuO is mainly due to the different Cu valence states. Copper is in Cu^+ state in

Cu_2O and in Cu^{2+} state in CuO.[31,32] Cu_2O shows spontaneous p-type semiconductor characteristics and it was shown that this p-type conductivity comes from cation-deficiency which is mainly due to the copper vacancies rather than oxygen interstitials or other defects.[33] Doping mechanism of Cu_2O is not well understood so far but several elements are known as efficient p-type dopants such as chlorine (Cl), silicon (Si) and nitrogen (N).[34,35,36] N-type doping has not been successfully demonstrated yet.

The crystal structure of Cu_2O is the cubic cuprite structure with lattice parameter 4.2696 Å. A unit cell has four copper atoms and two oxygen atoms and the oxygen atoms form body centered cubic (bcc) lattices and the copper atoms form face centered cubic (fcc) lattices as shown in Figure 1.2. Some fundamental properties of Cu_2O are listed in Table 1.2.

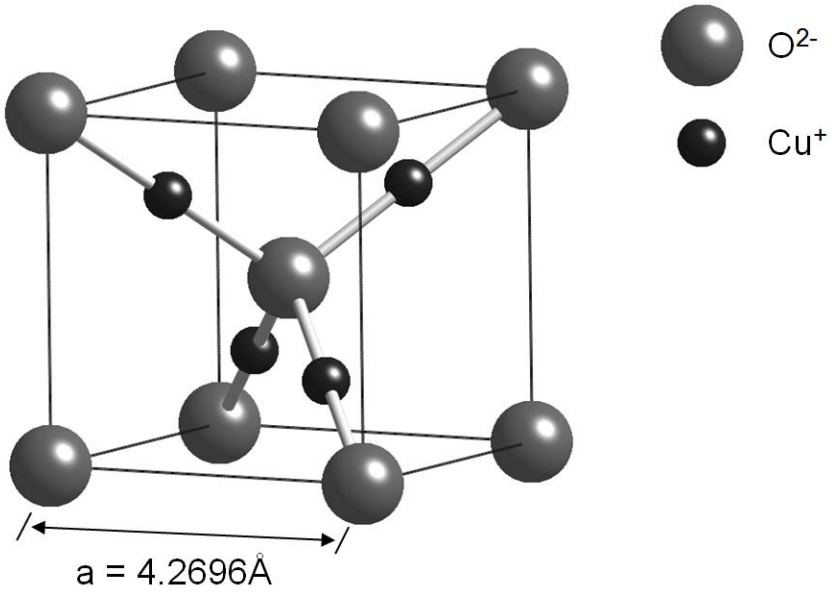

Figure 1.2. Cubic cuprite crystal structure of Cu_2O.

Table 1.2. Fundamental properties of Cu_2O. Unless indicated, all properties are at room temperature.[12,37]

Properties	Values
Density (g/cm^3)	5.749 ~ 6.14 (variation due to the presence of voids in most synthetic materials)
Melting temperature (K)	1508
Crystal structure	Cuprite (Cubic) (Space group : Pn3m - O_h^4)
Lattice constant (Å)	a = 4.2696
Band gap (eV)	2.17 (direct)
Hole Hall mobility (cm^2/V sec)	μ = 70
Dielectric constant	$\varepsilon(0) = 7.11$; $\varepsilon(\infty) = 6.46$

1.3 Thesis organization

Following introduction of chapter 1, thin film deposition of ZnO by metal organic chemical vapor deposition (MOCVD) and plasma enhanced chemical vapor deposition (PECVD) are described in chapter 2. Specifically, in chapter 2, the dependence of ZnO thin film morphology on the substrate materials and orientation was investigated. I found that ZnO thin film shows epitaxy on r-plane sapphire with $(11\bar{2}0)_{ZnO} \,||\, (1\bar{1}02)_{Al_2O_3}$ and

$[0001]_{ZnO} \perp [11\bar{2}0]_{Al_2O_3}$ and this is also discussed in detail in chapter 2.

In chapter 3, I discuss the properties of ZnO thin films deposited by radio frequency magnetron sputtering on glass substrates. Specifically the electrical, structural and optical properties of sputtered ZnO on glass are described. The effect of key process factors such as oxygen flow rate and substrate temperature was investigated. Especially I show how the various post-annealing treatments such as thermal annealing and oxygen plasma exposure affect the film properties.

In chapter 4, I describe deposition of thin Cu_2O films by MOCVD. Cu_2O was deposited on ZnO thin films to form heterojunctions and the dependence of film properties on substrate temperature and film thickness was investigated. Although Cu_2O and ZnO have different crystal structures (cubic and hexagonal), Cu_2O grows epitaxially on ZnO and I discuss the reasons for this in detail in this chapter.

In chapter 5, I describe the fabrication of Cu_2O/ZnO heterojunction thin film solar cells and show the results of photovoltaic characterization. In order to investigate the carrier transport mechanism in detail, current-voltage (*J*-*V*) characteristics in the dark and under illumination were collected and analyzed as a function of temperature between 100 K - 300 K. These measurements are presented and discussed in detail in this chapter. Finally, Chapter 6 includes summary and main conclusions along with future directions.

References

[1] David P. Norton, Mater. Sci. Eng. **R 43**, 139 (2004**).**

[2] C. N. R. Rao, B. Raveau, Transition Metal Oxides, Wiley-VCH, New York, 1998.

[3] D. C. Look, Mat. Sci. Eng. **B80**, 383 (2001).

[4] J. F. Wager, Science **300**, 1245 (2003).

[5] K. Koike, I. Nakashima, K. Hashimoto, S. Sasa, M. Inoue, M. Yano, Appl. Phys. Lett. **87**, 112106 (2005).

[6] K. Akimoto, S. Ishizuka, M. Yanagita, Y. Nawa, G. K. Paul, T. Sakurai, Sol. Energy **80**, 715 (2006).

[7] S. J. Pearton, W. H. Heo, M. Ivill, D. P. Norton, T. Steiner, Semicond. Sci. Tech. **19**, R59 (2004).

[8] U. Ozgur, Ya .I. Alivov, C. Liu, A,Teke, M.A. Reshchikov, S. Dogan, V. Avrutin, S.J. Cho, H. Morkoc, J. Appl. Phys. **98**, 041301 (2005).

[9] T. Minami, MRS Bull. **38** , August (2000).

[10] R. G. Gordon, MRS Bull. **52**, August (2000).

[11] R. L. Hoffman, B. J. Norris, J. F. Wager, Appl. Phys. Lett. **82**, 733 (2003).

[12] Otfried Madelung, Semiconductors : Data Handbook, Springer, 3rd edition, 2004.

[13] J. J. Loferski, J. Appl. Phys. **27**, 777 (1956).

[14] C. A. Dimitriadis, L. Papadimitriou, N. A. Economou, J. Mat. Sci. Lett. **2**, 691 (1983).

[15] L. C. Olsen, F. W. Addis, W. Miller, Sol. Cells **7**, 247 (1982-1983).

[16] J. Herion, E. A. Niekisch, G. Scharl, Sol. Energ. Mater. **4**, 101 (1980).

[17] L. Papadimitriou, N. A. Economou D. Trivich, Sol. Cells **3**, 73 (1981).

[18] A. E. Rakhshani, Solid State Electron. **29**, 7 (1986).

[19] J. Q. Xie, J. W. Dong, A. Osinsky, P. P. Chow, Y. W. Heo, D. P. Norton, S. J. Pearton, X. Y. Dong, C. Adelmann, C. J. Palmstrom, Mater. Res. Soc. Symp. P. **891**, 407 (2006).

[20] K. Ellmer, J. Phys. D. Appl. Phys. **34**, 3097 (2001).

[21] S. Ishizuka, K. Suzuki, Y. Okamoto, M. Yanagita, T. Sakurai, K. Akimoto, N. Fujiwara, H. Kobayashi, K. Matsubara, S. Niki, Phys. Status. Solidi. **1**, 1067 (2004).

[22] R. G. Gordon, Mater. Res. Soc. Symp. P. **426**, 419 (1996).

[23] M. Izaki, T. Shinagawa, K. Mizuno, Y. Ida, M. Inaba, A. Tasaka, J. Phys. D Appl. Phys. **40**, 3326 (2007).

[24] C. H. Bates, W. B. White, R. Roy, Science **137**, 993 (1962).

[25] Satischandra B. Ogale, Thin films and Heterostructures for oxide electronics, Chapter 10, 303 (Springer, 2005).

[26] D. C. Look, J. W. Hemsky, J. R. Sizelove, Phys. Rev. Lett. **82**, 2552 (1999).

[27] Chris G. Van de Walle, Phy. Rev. Lett. **85**, 1012 (2000).

[28] C. A. Wolden, T. M. Bames, J. B. Baxter, E. S. Aydil, J. Appl. Phys. **97**, 043522 (2005).

[29] B. Claflin, D. C. Look, S. J. Park, G. Cantwell, J. Cryst. Growth **287**, 16 (2006).

[30] Y. W. Heo, S. J. Park, K. Ip, S. J. Pearton, D. P. Norton, Appl. Phys. Lett. **83**, 1128 (2003).

[31] W. Y. Ching, Y. N. Xu, K. W. Wong, Phys. Rev. B **40**, 7684 (1989).

[32] T. ITO, H. Yamaguchi, K. Okabe, T. Masumi, J. Mater. Sci. **33**, 3555 (1998).

[33] H. Raebiger, S. Lany, A. Zunger, Phys. Rev. B **76**, 045209 (2007).

[34] A. O. Musa, T. Akomolafe, M. J. Carter, Sol. Energ. Mat. Sol. C. **51**, 305 (1998).

[35] S. Ishizuka, S. Kato, Y. Okamoto, K. Akimoto, Appl. Phys. Lett. **80**, 950 (2002).

[36] Y. Nakano, S. Saeki, T. Morikawa, Appl. Phys. Lett. **94**, 022111 (2009).

[37] G. P. Pollack, D. Trivich, J. Appl. Phys. **46**, 163 (1975).

Chapter 2

Properties of ZnO thin films deposited by metal organic chemical vapor deposition

2.1 Introduction

In this chapter, properties of ZnO thin films deposited by metal organic chemical vapor deposition (MOCVD) are described. ZnO thin films can be deposited by various techniques such as radio-frequency magnetron sputtering,[1] molecular beam epitaxy (MBE),[2] pulsed laser deposition (PLD),[3] chemical vapor deposition (CVD),[4] electrochemical deposition[5] and spray pyrolysis.[6] Applications in opto-electronic devices require high quality epitaxial thin films and among these methods, MBE, PLD and CVD can produce epitaxial ZnO films. CVD is particularly attractive because it can be scaled up for mass production. For this reason, it is one of the most popular deposition techniques in the semiconductor industry.

ZnO has wurtzite hexagonal crystal structure and tends to grow in columnar morphology because growth rate in c-axis direction is much faster than the growth rate of basal planes.[7] Because of this anisotropic growth and columnar morphology, it is difficult to deposit films with smooth surface. However, many device applications require thin films with smooth surface so that abrupt and smooth heterojunctions can be formed. I

deposited ZnO thin films on various substrates including amorphous glass, silicon and sapphire (a-plane and r-plane, Figure 2.1) by MOCVD and investigated the dependence of the structure and morphology of ZnO thin films on the substrate. All the zinc oxide thin films deposited on amorphous glass, silicon and a-plane sapphire shows textured structure with (0002), (c-axis) parallel to the substrate normal but the films deposited on r-plane sapphire have the c-axis parallel to substrate surface. ZnO has epitaxial relationship with r-plane sapphire and this is described in detail in this chapter including the dependence of morphology on the deposition temperature.

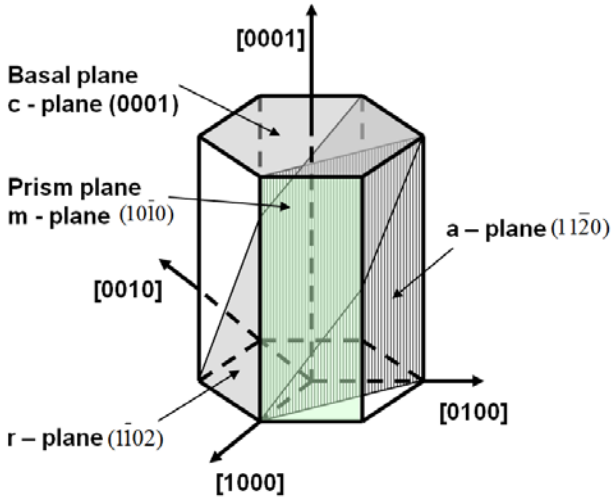

Figure 2.1. Hexagonal crystal structure unit cell and planes.

To control the morphology of ZnO thin films, plasma enhanced chemical vapor deposition (PECVD) was also investigated. PECVD has several advantages that may improve the deposited film quality and morphology.[8] Specifically, high energetic particle

bombardment from plasma can affect surface reactions and dissociate metal organic precursors. The dependence of the structure and morphology of ZnO films deposited by PECVD on process parameters such as applied power and process pressure was investigated and this is described in this chapter.

2.2 Metal organic chemical vapor deposition of ZnO thin films

2.2.1 Chemical vapor deposition (CVD) process

Chemical vapor deposition (CVD) makes use of chemical reactions on a hot surface. The steps that lead to the deposition of a thin film in CVD are shown in figure 2.2.[9] Typically the film precursors are delivered to the deposition chamber by a carrier gas and react with other gases on the heated substrate surface to nucleate and grow the desired film. The volatile by-products of the reactions are pumped out.

Several important factors affect the quality of the film deposited by CVD. These include the properties of the precursor, the substrate, the deposition temperature, the process pressure, the carrier gas flow rate and the chamber geometry. To deposit ZnO films by CVD, a zinc containing precursor and an oxygen source are needed. Metal-organic compounds such as diethyl zinc [$Zn(C_2H_5)_2$, DEZ], dimethyl zinc [$Zn(CH_3)_2$, DMZ], zinc acetate [$Zn(CH_3COO)_2$] and zinc acetylacetonate [$Zn(C_5H_7O_2)_2$, $Zn(acac)_2$] have been used as zinc precursors. Oxygen sources that have been used in conjunction with these zinc precursors include O_2, CO_2, H_2O, N_2O and NO_2.[10]

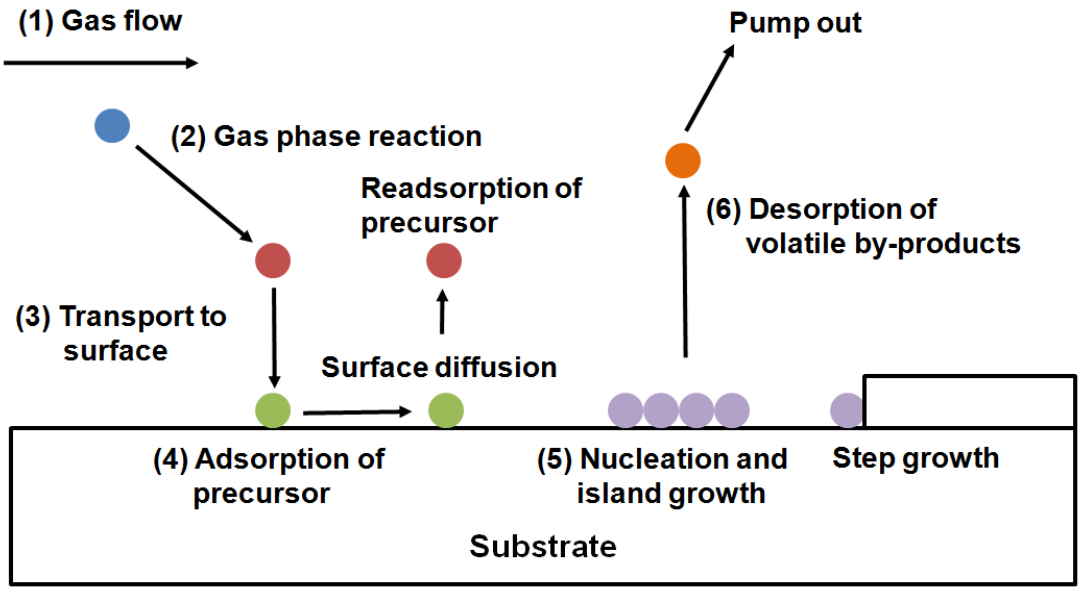

Figure 2.2. Sequential process steps that lead to chemical vapor deposition (CVD) of thin films on a substrate. The steps are (1) transport of the precursor from gas inlet to reaction region, (2) chemical reaction in gas phase to produce new reactive species, (3) transport of reactive species to the substrate surface, (4) adsorption of reactive species on the substrate and surface diffusion, (5) nucleation and growth to form film and (6) desorption of by-products and pumping out from the reaction region. This figure is adopted from reference 9.

Among the zinc precursors, DEZ is used most widely because it leads to high quality films with O_2 as the oxidizing gas and DEZ vapor flow and hence the deposition rate can be controlled easily. However, DEZ is pyrophoric which makes its use and delivery difficult. Instead, I used a solid precursor, zinc acetylacetonate ($Zn(C_5H_7O_2)_2$, $Zn(acac)_2$) because it is stable in ambient conditions and does not react with atmospheric oxygen or water. Thus, the manipulation of $Zn(acac)_2$ is easier than DEZ.

2.2.2 Chemical vapor deposition (CVD) system

I designed and set up a high vacuum CVD system for ZnO thin film deposition. A schematic of this system is shown in Figure 2.3 and photographs are shown in Figure 2.4. The 4-inch diameter cylindrical deposition chamber is evacuated through a side port located just below the sample stage by a turbo molecular pump (TMP) which provides a base pressure of 3×10^{-7} Torr. Rotary mechanical pumps are used for TMP backing and initial chamber pumping from atmosphere to around 50 mTorr. The flow rate of gases (argon for carrier gas, O_2 for process and N_2 for venting) are controlled by mass flow controller (MFC) from zero to 3000 standard cubic centimeter per minute (sccm). Substrate is placed on the sample stage which can be heated up to 1000˚C by resistance heater and the substrate temperature is controlled by K-type thermocouple and close loop feedback controller.

The precursor [$Zn(acac)_2$] is placed in a stainless steel tank [Figure 2.4 (c)] with one inlet for the carrier gas (Ar) and an outlet that led to the deposition chamber. The precursor tank is surrounded by a band heater and a thermocouple is attached at the bottom of the tank for independent temperature control. Sublimed precursors flow downward from the top flange through a showerhead. During the deposition, the valve in front of TMP is closed and pumping through the rotary pump is used. Process pressure is adjusted using a butterfly valve located between the chamber and the rotary pump in the range of 1 - 10 Torr and a capacitance manometer gauge is used for the accurate measurement of the process pressure. The precursor and oxygen gases are fed into the deposition chamber through separate lines to prevent the premature reaction between the two gases. The gas line that connects the precursor tank to the showerhead is heated to

150˚C to prevent the condensation of sublimed precursor.

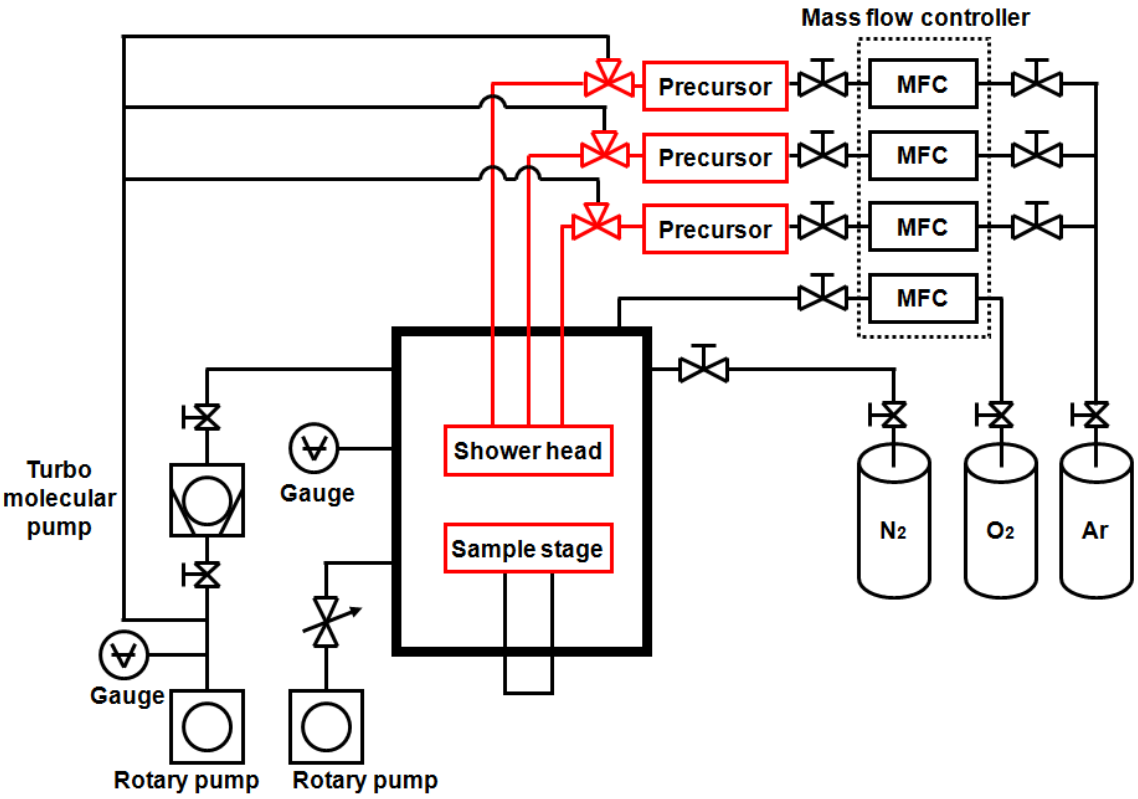

Figure 2.3. Schematic of the CVD system for ZnO thin film deposition. Red lines indicate heated lines.

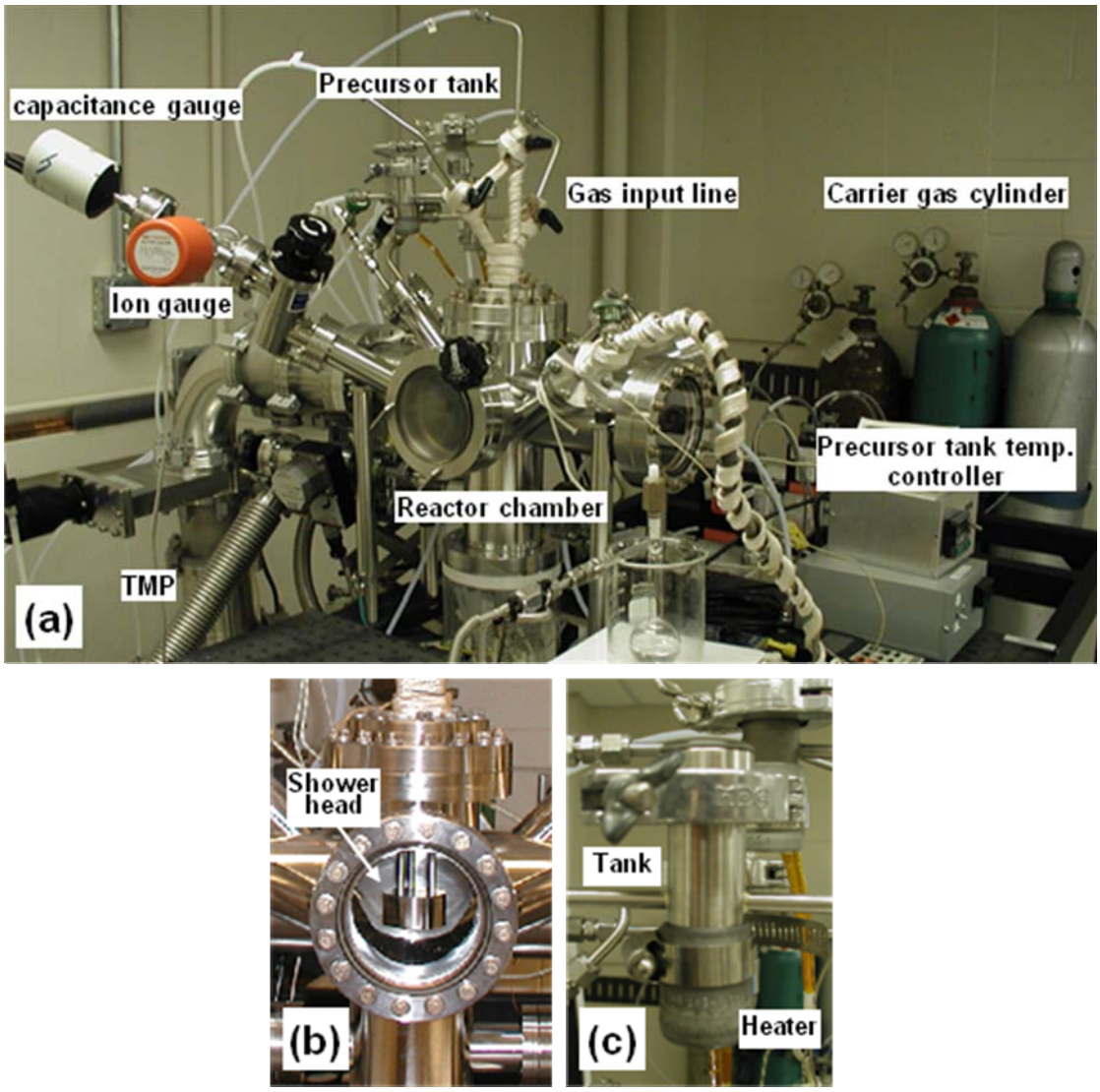

Figure 2.4. (a) CVD system for ZnO thin film deposition ; (b) shows the shower head ; (c) shows the solid precursor tank where the bottom of the precursor tank is surrounded by a heater.

2.2.3 ZnO film deposition kinetics

The deposition rate of ZnO thin films by MOCVD from $Zn(acac)_2$ and oxygen on silicon substrate was investigated. The process conditions used in this investigation are summarized in Table 2.1. Figure 2.5 shows dependence of the deposition rate on the substrate temperature between 573 K and 873 K. The deposition rate below 773 K shows Arrhenius behavior indicating that the process may be surface-reaction-limited. The slope of the deposition rate versus 1/T line is reduced above 773 K which indicates the process may become mass-transport-limited at high temperature. From the slope of the line in the low temperature region (573 K ~ 773 K), an activation energy of 96 kJ/mol is extracted.

Table 2.1. MOCVD process conditions for ZnO thin film.

Process condition	Values
Deposition temperature (K)	573 - 873
Precursor sublime temperature (˚C)	90 - 110
Carrier gas (Ar) flow rate (sccm)	10 - 200
O_2 flow rate (sccm)	300
Process pressure (Torr)	1 - 10

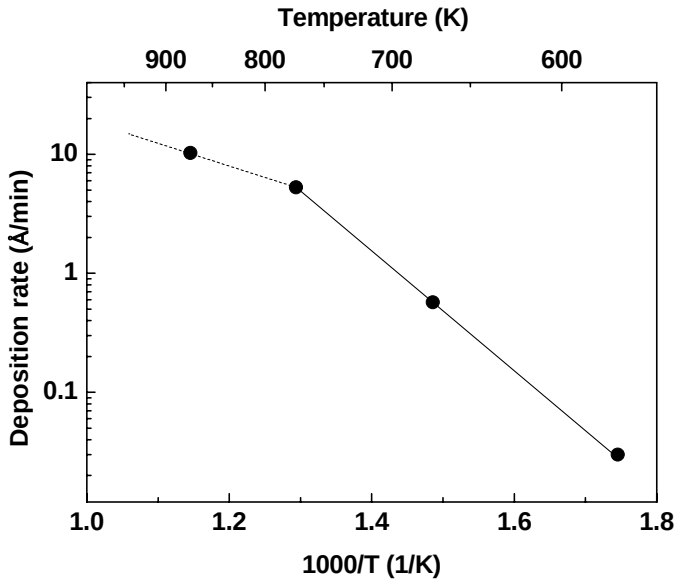

Figure 2.5. Arrhenius plot of the deposition rate versus the substrate temperature (1000/T). The substrates were Si wafers. Solid line shows the linear fit to the data between 573 K and 773 K.

Figure 2.6 shows the dependence of the deposition rate on the ratio of the carrier gas (Ar) flow rate to the oxygen gas flow rate at constant process pressure (~ 5 Torr) and constant substrate temperature (773 K). The Ar to O_2 flow rate ratio is a measure of the ratio of zinc precursor to O_2 partial pressure in the reactor. Increasing this ratio increases both the Zn precursor flow rate into the chamber and the ratio of the Zn precursor partial pressure to O_2 partial pressure. The deposition rate increases with Ar to O_2 flow rate ratio up to ~ 0.35 and then saturates. This behavior indicates that the process may be limited by zinc precursor partial pressure when the Ar-to-O_2 flow rate ratio is below 0.35. The dependence of deposition rate on total process pressure (Figure 2.7) shows that it has a maximum value at around 5 Torr.

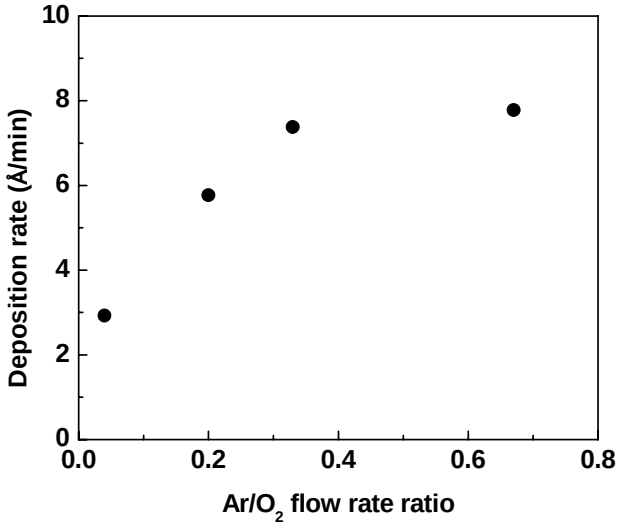

Figure 2.6. ZnO deposition rate versus Ar-to-O_2 flow rate ratio. The substrate temperature and process pressure were kept constant at 773 K and 5 Torr, respectively.

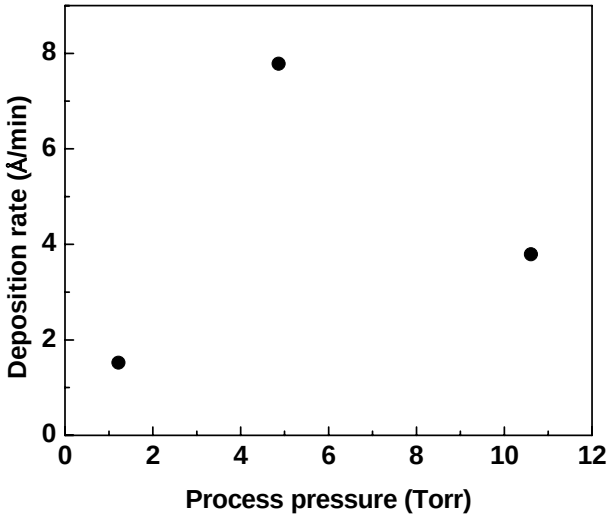

Figure 2.7. ZnO deposition rate versus the process pressure. The flow rates of the carrier gas (Ar) and oxygen were kept at 200 sccm and 300 sccm, respectively. The substrate temperature was 773 K.

2.3 The dependence of ZnO film morphology on the substrates

The X-ray diffractions of ZnO thin films deposited by MOCVD on various substrates are shown in Figure 2.8. The substrates included amorphous glass, (100) oriented Si, (111) oriented Si, a-plane sapphire and r-plane sapphire. With the exception of r-plane sapphire, the XRD from films deposited on all these substrates show only the substrate peaks and the $(0002)_{ZnO}$ peak. The film deposited on r-plane sapphire substrate shows $(11\bar{2}0)_{ZnO}$ diffraction in addition to the substrate peaks. Ohotomo et al. also observed the same in ZnO thin films grown by pulsed laser deposition (PLD). Thin ZnO films grown by PLD showed that [0002] axis is parallel to the substrate surface normal except on r-plane sapphire.[3]

The fact that ZnO has a preferred growth direction regardless of substrates indicates that this is not due to the epitaxy between the film and the substrates but is an intrinsic tendency of ZnO to grow anisotropically with its c-axis oriented parallel to the surface normal. ZnO has wurtzite hexagonal crystal structure and the surface energies are anisotropic. Specifically, the surface formation energies are higher in the order of (0002), $(10\bar{1}1)$ and $(10\bar{1}0)$ planes. The plane with lower formation energy is likely to grow larger in size, while the planes with higher formation energies tend to minimize their area during film growth. Therefore, the fastest growth direction will be the normal direction of the plane with the highest formation energy. This makes the ZnO [0002] direction (c-axis) the fastest growth direction.[11]

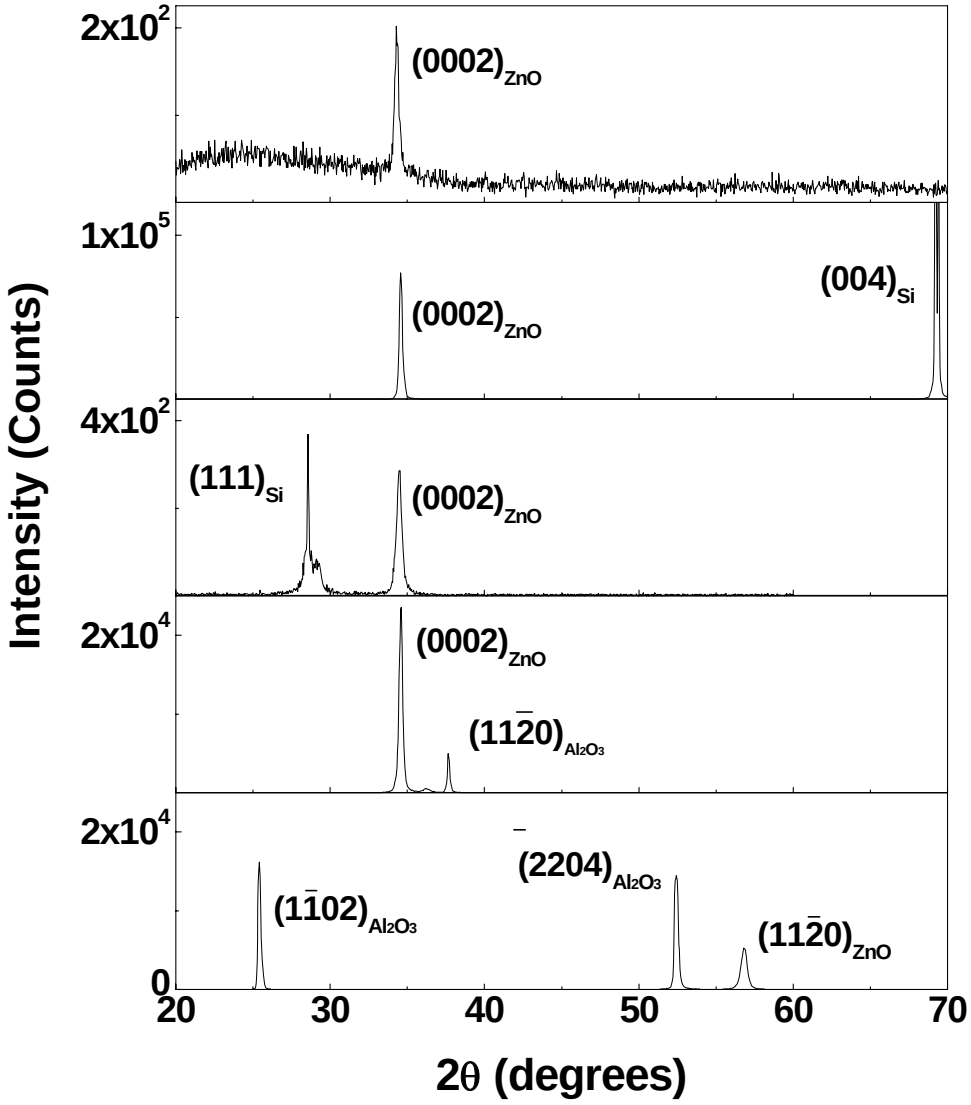

Figure 2.8. X-ray diffraction from ZnO films deposited by MOCVD on various substrates. (a) Glass, (b) (100) oriented Si, (c) (111) oriented Si, (d) a-plane sapphire and (e) r-plane sapphire.

ZnO and sapphire have the same crystal structure (hexagonal wurtzite) while Si has a different (cubic) structure. Thus, we would expect that the ZnO films deposited on sapphire to have better crystallinity than those deposited on Si. Indeed, this expectation is

consistent with the XRD of film deposited on sapphire and Si. Figure 2.9 shows the XRD rocking curves for thin ZnO films deposited on (111) oriented Si, a-plane sapphire and r-plane sapphire. The full widths of the rocking curves at half the maximum intensity (FWHM) are 6.7˚, 1˚ and 0.5˚ for films grown on (111)-oriented Si, a-plane sapphire and r-plane sapphire, respectively. A smaller FWHM value of XRD rocking curves indicates better crystallinity. Hence, the highest crystallinity films are grown on r-plane sapphire followed by a-plane sapphire and (111)-oriented silicon. These results are also consistent with the morphologies seen in SEM images displayed in Figure 2.10. These SEM images show that the ZnO films on silicon substrates have a rough surface morphology while the film deposited on a-plane and r-plane sapphire substrates show columnar growth and smooth and dense morphology, respectively.

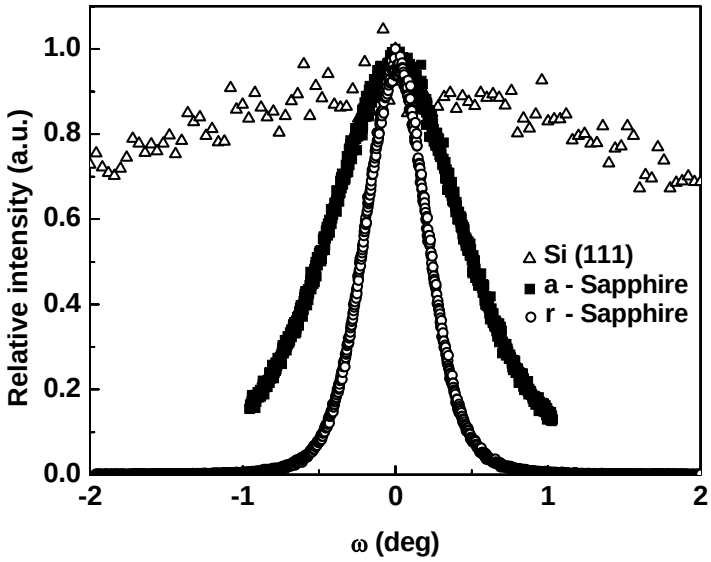

Figure 2.9. XRD rocking curves of ZnO thin films deposited on Si (111), a-plane sapphire and r-plane sapphire. The process pressure and substrate temperature were kept constant at 5 Torr and 600 ˚C, respectively.

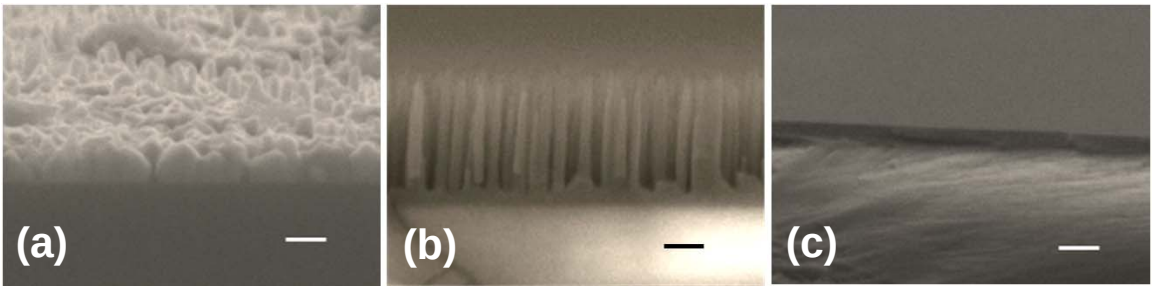

Figure 2.10. SEM images of ZnO thin films deposited on (a) (111)-oriented Si, (b) a-plane sapphire and (c) r-plane sapphire. The scale bars are 100 nm.

2.4 Structural properties of ZnO thin films grown on r-plane sapphire

Since ZnO films tend to grow in columnar structures on many substrates with c-axis perpendicular to the substrate surface, it is difficult to deposit films with smooth surface.[7] In contrast, ZnO films grow on r-plane sapphire with their c-axis, the preferred growth direction, parallel to the substrate surface. Resulting films exhibit smooth surfaces. In this section, structural properties of ZnO films on r-plane sapphire including epitaxial relationship and surface morphology are described. Specifically I focus on the substrate temperature between 400˚C and 700˚C.

The epitaxial relationship between films and substrates was characterized using XRD θ-2θ scan and ϕ-scan measurements and crystal quality was examined through XRD rocking curve measurements. Surface roughness was measured by atomic force microscopy (AFM) and surface morphology was investigated by SEM.

2.4.1 Epitaxy between ZnO and r-plane sapphire

Figure 2.11 shows the result of XRD from a film deposited on r-plane sapphire at 600 ˚C. All other films deposited on r-plane sapphire between 400 ˚C ~ 700 ˚C showed same XRD pattern. The positions of the three peaks are at 25.6˚, 52.6˚ and 56.7˚ which correspond to the $(1\bar{1}02)_{Al_2O_3}$, $(2\bar{2}04)_{Al_2O_3}$ and $(11\bar{2}0)_{ZnO}$, respectively. This indicates that one component of the epitaxial orientation relationship is $(11\bar{2}0)_{ZnO} \parallel (1\bar{1}02)_{Al_2O_3}$.

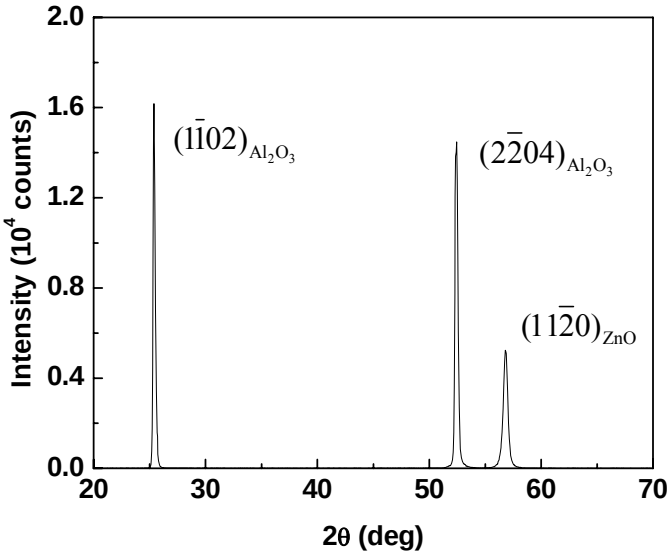

Figure 2.11. XRD θ-2θ scan of ZnO film deposited on r-plane sapphire. The process pressure and substrate temperature were 5 Torr and 600 ˚C, respectively.

In-plane orientation of the ZnO films on r-plane sapphire was investigated using XRD ϕ-scan measurements. Two ϕ-scans were conducted, one scan with 2θ fixed at 41.7˚ [$(0006)_{Al_2O_3}$ diffraction] and another with 2θ fixed at 31.8˚ [$(10\bar{1}0)_{ZnO}$ diffraction]. These two ϕ-scans are shown in Figure 2.12. The $(0006)_{Al_2O_3}$ diffraction peak from sapphire

substrate is separated from the two $(10\bar{1}0)_{ZnO}$ diffraction peaks by 90˚. The zone axis of sapphire (0006) and $(1\bar{1}02)$ planes is the $[11\bar{2}0]$ direction, whereas the zone axis of ZnO $(10\bar{1}0)$ and $(11\bar{2}0)$ planes is the [0001] direction which leads to the conclusion that sapphire $[11\bar{2}0]$ must be perpendicular to the ZnO [0001]. Therefore, combining this result with the result of θ-2θ scan, $(11\bar{2}0)_{ZnO} \| (1\bar{1}02)_{Al_2O_3}$ the complete epitaxial relation between r-plane sapphire and ZnO is determined to be $(11\bar{2}0)_{ZnO} \| (1\bar{1}02)_{Al_2O_3}$ and $[0001]_{ZnO} \perp [11\bar{2}0]_{Al_2O_3}$.

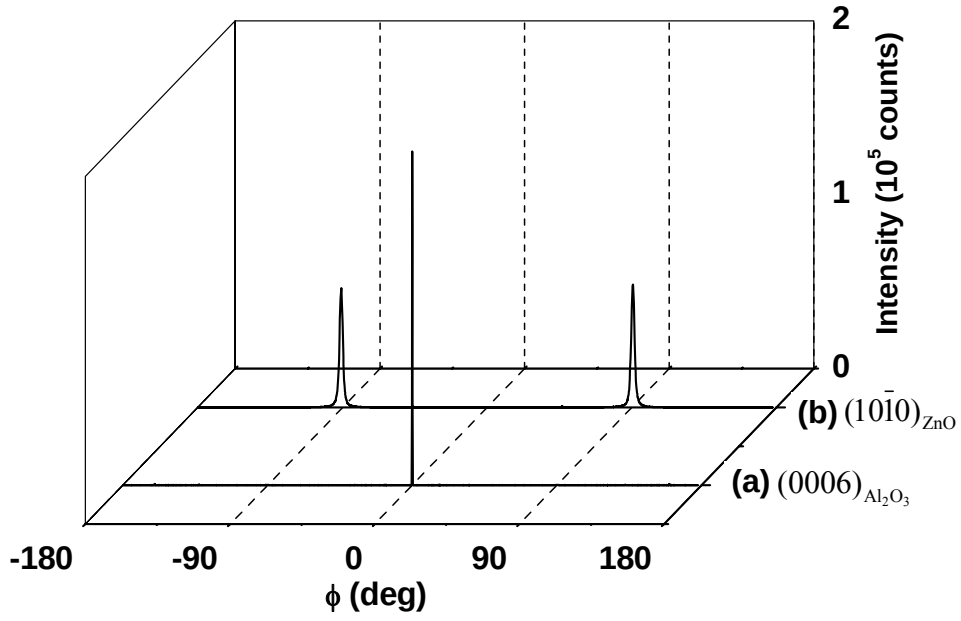

Figure 2.12. XRD in-plane ϕ-scan. (a) is the scan of $(0006)_{Al_2O_3}$ peak from sapphire substrate and (b) is the scan of $(10\bar{1}0)_{ZnO}$ peak form ZnO film.

This epitaxial relationship agrees with the growth mechanism proposed by Kung et al.[12] who developed a model of the epitaxial growth of wurtzite type thin films on r-

plane sapphire. According to this model, the surface of the r-plane sapphire is oxygen-terminated and the oxygen atoms are aligned on the surface along the $[\bar{1}101]$ direction as shown in Figure 2.13. The oxygen atoms on $(11\bar{2}0)_{ZnO}$ plane are also aligned along the $[0001]$ direction and when ZnO films are deposited on r-plane sapphire, rows of oxygen atoms are deposited along the valley between oxygen ridges on sapphire substrate. Therefore, ZnO films grow with c-axis parallel to the sapphire $[\bar{1}101]$ which is equivalent to $[0001]_{ZnO} \perp [11\bar{2}0]_{Al_2O_3}$.

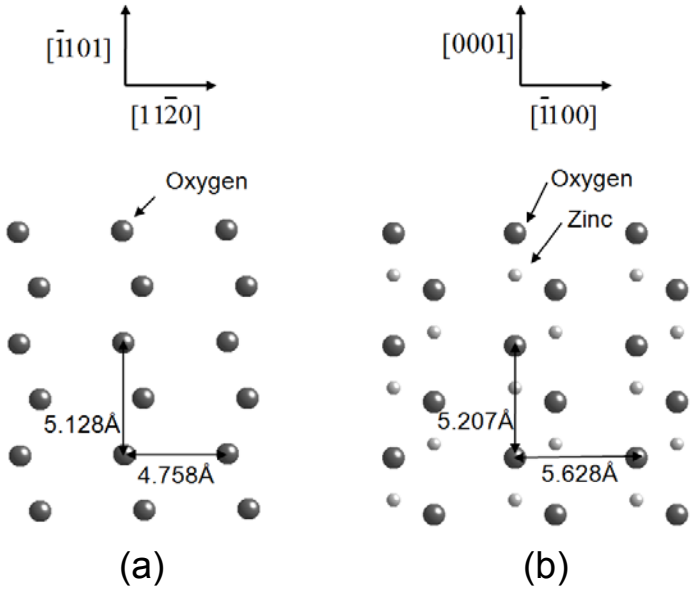

Figure 2.13. Atomic arrangement of (a) sapphire $(1\bar{1}02)$ (r-plane) and (b) ZnO $(11\bar{2}0)$ crystal planes, respectively. In-planar directions are denoted on top of each diagram. Based on this epitaxial relationship, the lattice mismatches between ZnO and sapphire are 1.53 % along ZnO c-axis and 18.3 % perpendicular to the ZnO c-axis.

Figure 2.14 illustrates the XRD in-plane scan for $(10\bar{1}0)_{ZnO}$ plane used in this experiment. Figure 2.14 (a) and (b) shows the XRD geometry and the geometry of the

ZnO film with the $(11\bar{2}0)_{ZnO}$ plane parallel to the r-plane sapphire. Initially, the film surface is parallel to the X-ray incident plane which is defined by the incident and diffracted X-ray beams. Starting with this configuration, the sample is tilted by 60˚ in the ψ direction to bring the $(10\bar{1}0)_{ZnO}$ plane normal to the X-ray scattering vector [Figure 2.14 (c)]. If we set θ-2θ value as the Bragg angle of the ZnO $(10\bar{1}0)$ plane (2θ = 31.8˚), Bragg's diffraction condition is satisfied in this situation. If we measure X-ray diffraction pattern in the range of ϕ between 0˚ and 360˚ while keeping 2θ = 31.8˚, we get 2 peaks whose positions are separated by 180˚ because two sets of $\{10\bar{1}0\}$ planes can satisfy the Bragg condition during the ϕ-scan. XRD in-plane scan for Al_2O_3 (0006) plane was conducted with a similar manner.

2.4.2 Dependence of crystallinity on deposition temperature

Figure 2.15 shows the XRD rocking curves for $(11\bar{2}0)_{ZnO}$ peaks of ZnO films deposited at various substrate temperatures. The FWHM's for these curves are 1˚, 0.5˚ and 0.9˚ for films deposited at 500˚C, 600˚C and 700˚C, respectively. Figure 2.15 shows the temperature dependence of the FWHM values for both the XRD peaks (θ-2θ scan) and the rocking curves. The FWHM values for both decrease as temperature increases from 400 ˚C to 600 ˚C. However, these trends diverge as temperature is increased further to 700˚C : The FWHM value for the rocking curve increases while the FWHM of the XRD peak (θ-2θ scan) remains unchanged. The decrease in FWHM of both XRD peaks and rocking curves is consistent with increasing grain size and improved epitaxial

alignment of the films up to 600˚C. However, it appears that this alignment deteriorates above 600˚C.

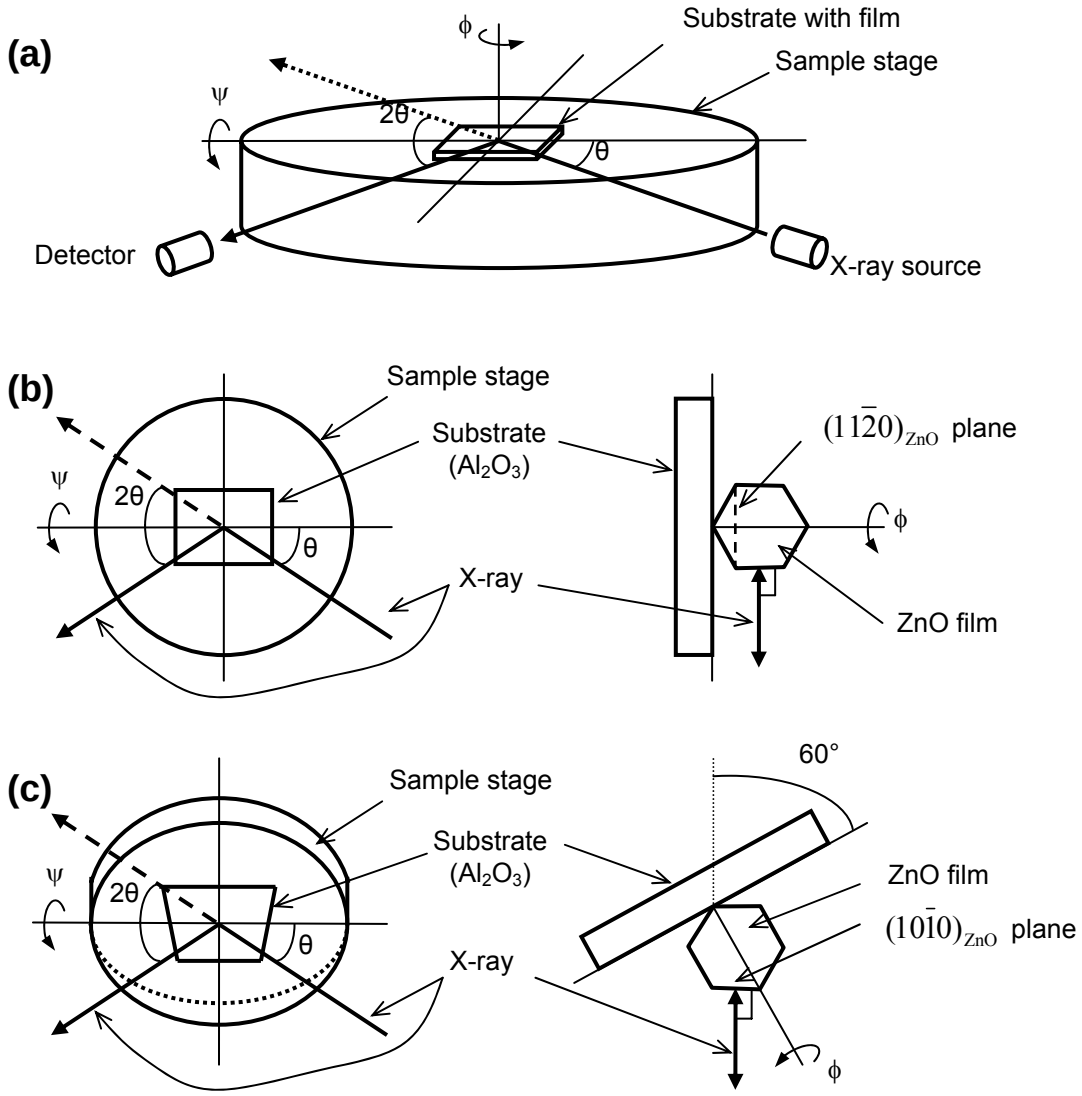

Figure 2.14. Illustration of the in-plane ϕ-scan measurement. (a) An illustration of the XRD geometry and the definition of the angle θ, ϕ and ψ. (b) Shows the ZnO film on r-plane sapphire with $(11\bar{2}0)$ plane parallel to r-plane as determined in θ-2θ scan. (c) Shows the situation when sample is tilted by 60° along with ψ direction.

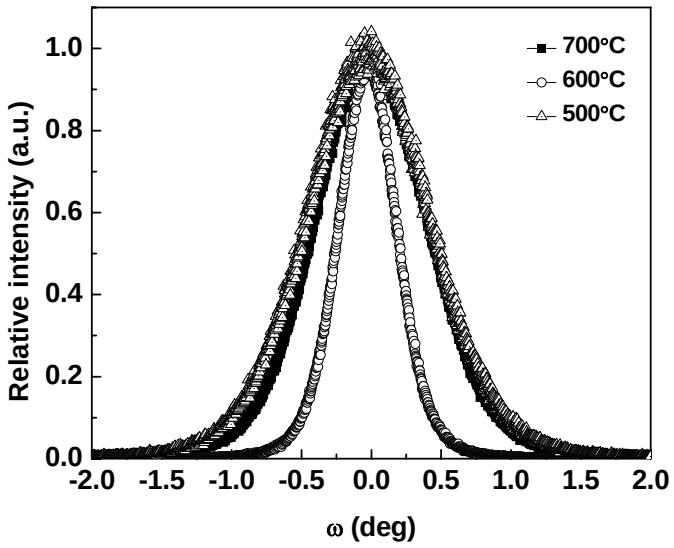

Figure 2.15. XRD rocking curves for $(11\bar{2}0)_{ZnO}$ peak of ZnO films deposited at 500˚C, 600°C and 700˚C.

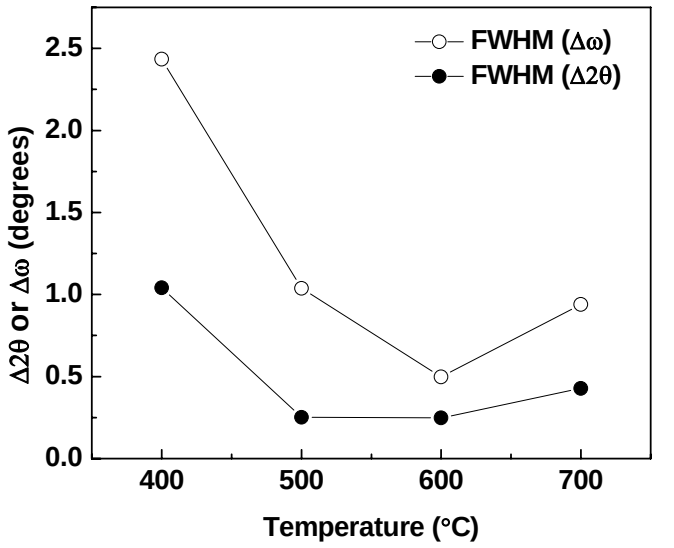

Figure 2.16. Temperature dependence of FWHM values of XRD rocking curves (Δω) and XRD diffraction peaks in the θ-2θ scan (Δ2θ).

2.4.3 Surface morphology

The SEM images of ZnO films deposited at 500 ˚C, 600 ˚C and 700 ˚C are shown in Figure 2.17. SEM images reveal that the film deposited at 500 ˚C has very smooth surface [Figure 2.17 (a)] but as the deposition temperature increases, poles growing out of the substrate plane appear. Figure 2.17 (b) shows a few poles on the surface of the film deposited at 600 ˚C. The density of poles is much larger on the film deposited at 700 ˚C [Figure 2.17 (c)].

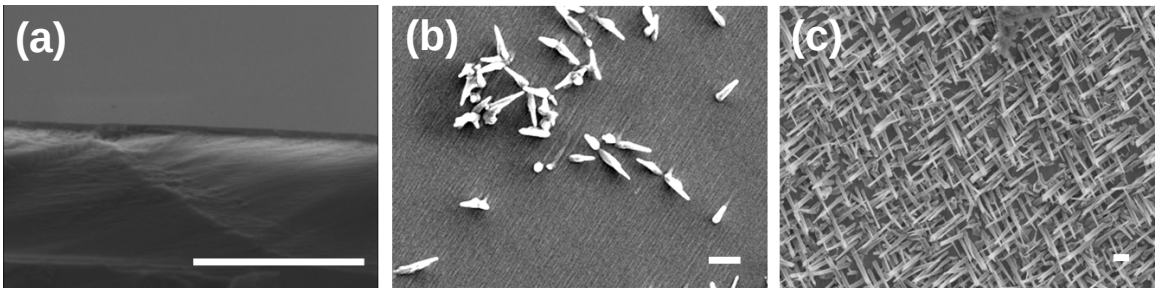

Figure 2.17. SEM images of ZnO films deposited at (a) 500 ˚C, (b) 600 ˚C and (c) 700 ˚C. SEM in (a) is the cross section image so that bottom is sapphire substrate and upper is film. SEMs shown in (b) and (c) are the top views. During deposition, Ar flow rate, O_2 flow rate and pressure are kept at 100 sccm, 300 sccm and 5.4 Torr, respectively. The scale bars are 1 μm.

Figure 2.18 shows the AFM images of the ZnO film surfaces. The root-mean-square surface roughness values are 0.394 nm, 0.391 nm and 5.49 nm over 1 μm × 1 μm area for 400˚C, 500˚C, and 600˚C, respectively. The surfaces are very smooth at 400˚C and 500˚C while the surface of the sample grown at 600˚C has grooves and ridges aligned in a specific direction. It was not possible to do AFM on the 700 ˚C as the surface was extremely rough with poles sticking off the surface. Xie et al. also observed such grooves and ridges parallel to $[\bar{1}101]$ direction of the sapphire substrate.[13] I believe that this morphology is developed by anisotropic growth of epitaxial ZnO islands on r-plane sapphire. ZnO grows much faster along the c-axis than $[10\bar{1}0]$ direction.[7] Since the c-axis of ZnO is parallel to the r-plane sapphire surface, after the nucleation of a ZnO island on the substrate surface, the islands grow anisotropically and give rise to this ridge morphology.

In addition to the ridge morphology, the films deposited above 600°C have poles growing out of the film surface. I think these poles are the result of strain relief. The lattice mismatch between the ZnO film and the r-plane sapphire is 1.53 % along the c-axis and 18.3 % perpendicular to the c-axis (Figure 2.13) and these mismatches cause strain in the deposited films. Figure 2.19 shows the lattice parameter of the ZnO films as a function of the deposition temperature. The lattice parameter approaches to the value for bulk ZnO (3.2496 Å)[14] as temperature increases. Although the films deposited at low temperature (below 500˚C) have smooth surface they are severely strained. The strain is reduced and poles appear as the deposition temperature increases.

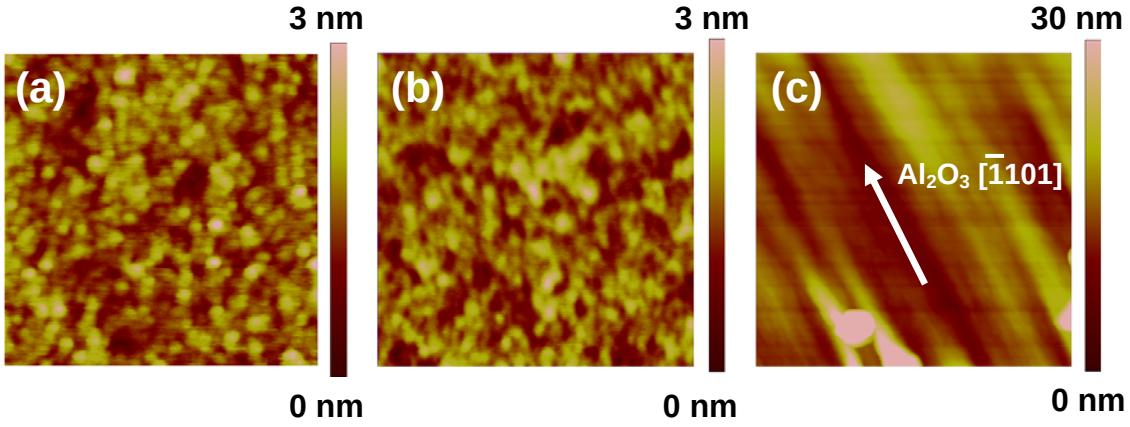

Figure 2.18. AFM images of ZnO films deposited (a) at 400˚C, (b) at 500˚C and (c) at 600˚C. The scan area is 1 μm × 1 μm.

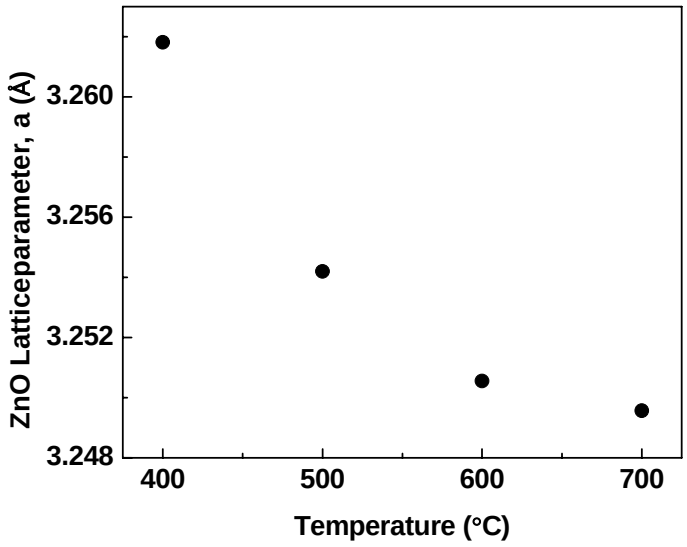

Figure 2.19. Dependence of the ZnO lattice parameter, a, on the deposition temperature. Lattice parameters are calculated from the XRD $(11\bar{2}0)_{ZnO}$ peak positions.

2.4.4 Two-step deposition

For applications requiring smooth epitaxial films, it is desired to suppress the nucleation and growth of poles shown in Figure 2.17 (c). A possibility is that the poles nucleate and grow directly from the substrate at high temperatures. If this is the case, it may be possible to suppress the poles by first growing a film at low temperature and then continuing the growth at high temperature. To test this hypothesis, I grew films while the substrate temperature was changed between two values. For the first two hours the substrate temperature was kept at 500 ˚C. Following the temperature was changed to 600 ˚C or 700 ˚C and the deposition was continued for an additional two hours.

Figure 2.20 shows the SEM images of two films. One of the films was grown for 2 hours at 500 ˚C followed by 2 hours at 600 ˚C [Figures 2.20 (a) and (c)]. The other film was grown for 2 hours at 500 ˚C followed by an additional 2 hours at 700 ˚C [Figures 2.20 (b) and (d)]. Comparison of Figures 2.20 (a) and (b) with Figures 2.17 (b) and (c) shows that the number density of poles was reduced in both cases compared to films deposited at 600 ˚C and 700 ˚C. In this two-step deposition process, the smooth film deposited during the first step acts as a buffer layer between the sapphire substrate and film deposited during the high temperature (600˚C or 700 ˚C) period. The buffer layer plays an improtant role in the morphology of films.[15] It seems that there is a competetion between two types of morphologies during ZnO film growth, poles and smooth films. The films with a buffer layer which is composed of same materials with the film will have small lattice mismatch between films and buffer layer and will be grown to smooth films. On the other hand, the films without buffer layer will have large lattice mismatch

and this prevents the film growth and increases the number of poles.

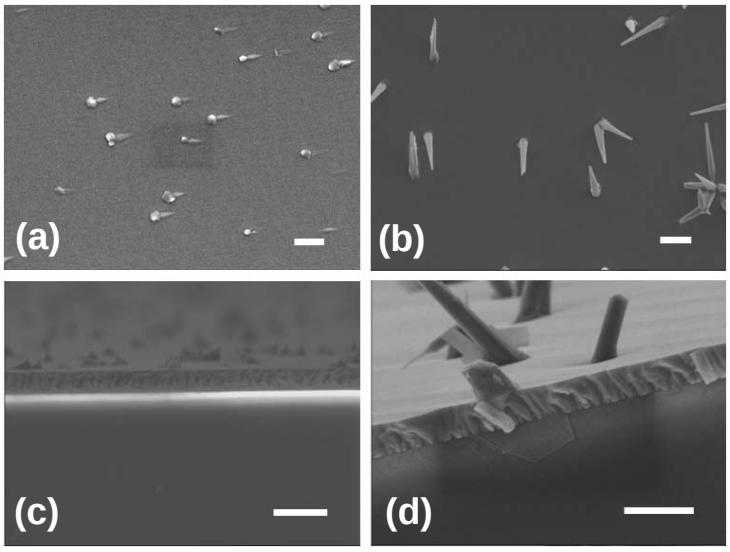

Figure 2.20. SEM images of ZnO films deposited at step temperature profile. (a) and (c) are the top view and cross section images of a film deposited at 500˚C/2hrs - 600˚C/2hrs. (b) and (d) are the top view and cross section images of a film deposited at 500˚C/2hrs - 700˚C/2hrs. The scale bar is 1 μm.

2.5 Plasma enhanced chemical vapor deposition of ZnO

It has been reported that the morphology of ZnO thin films can be changed and high quality ZnO thin films can be deposited at low deposition temperature through plasma enhanced chemical vapor deposition (PECVD).[16,17,18,19] It seems that energetic ion bambardment onto film surface and radicals generated in a plasma play an important role in determining the morphology of the ZnO films. Herein, I describe the properties of ZnO thin films deposited by PECVD.

2.5.1 Morphology of ZnO thin films deposited by PECVD

To generate plasma over a substrate, a 3.5 inch diameter ring type electrode was placed between showerhead gas distributor and the heated substrate stage in the MOCVD deposition chamber (section 2.2.2). Radio frequency (rf) power was used to maintain the plasma. The schematic of PECVD system is shown in Figure 2.21 and process conditions used in this study are summarized in Table 2.2. ZnO films were deposited under various conditions in the ranges presented in Table 2.2. Films deposited at 600 ˚C with 20 W rf power plasma maintained at 3.5 Torr while flowing 200 sccm Ar (carrier gas) and 300 sccm O_2 resulted in continuous and smooth films. These process conditions were set as standard and film properties were investigated by varying one of the process parameters from this standard conditions.

Table 2.2. PECVD process conditions for ZnO thin film.

Process condition	Values	Standard Values
Deposition temperature (˚C)	500 ~ 600	600
Precursor sublime temperature (˚C)	100	100
Carrier gas (Ar) flow rate (sccm)	100 ~ 200	200
O_2 flow rate (sccm)	300	300
Process pressure (Torr)	1 ~ 10	3.5
Plasma power (W)	20 ~ 40	20

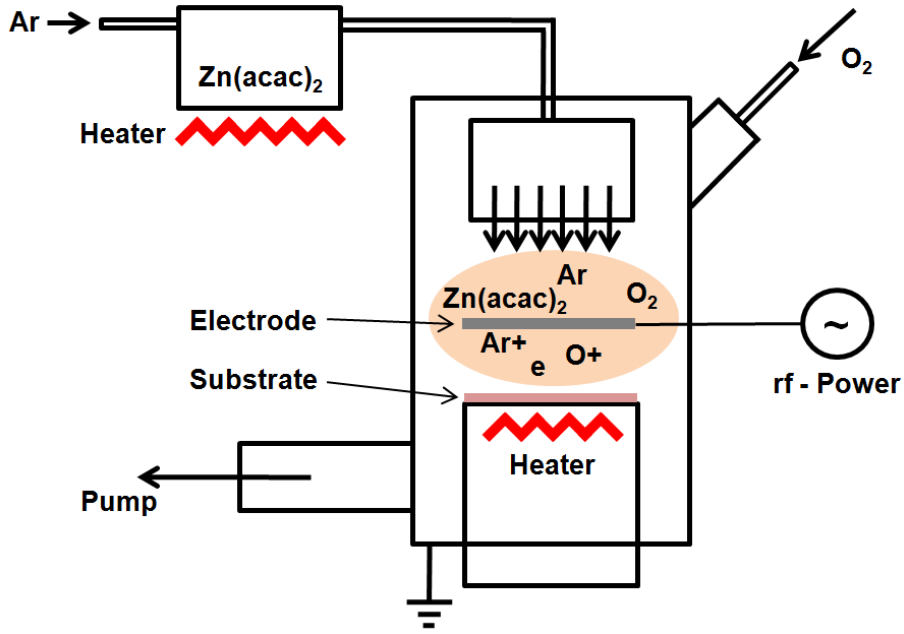

Figure 2.21. Schematic of PECVD system for ZnO thin film deposition. Argon and oxygen plasma is maintained during deposition by radio frequency power.

Figure 2.22 shows the SEM images of ZnO thin films deposited by PECVD on silicon substrates at 600 ˚C while maintaining the plasma at 3.5 Torr with RF power ranging from 20 W to 40 W. While typical ZnO thin films deposited on silicon without plasma exhibit rough mormophology [Figure 2.10 (a)], films deposited by PECVD seem to have continuous cross section. The films deposited at rf power of 20 W and 30 W look continuous and have smooth surfaces. However, the film morphology becomes columnar and surface roughness increases at 40 W. The anisotropic growth of ZnO seems to be surpressed at low rf power (below 30 W) but growth again becomes directional at high rf power (40 W).

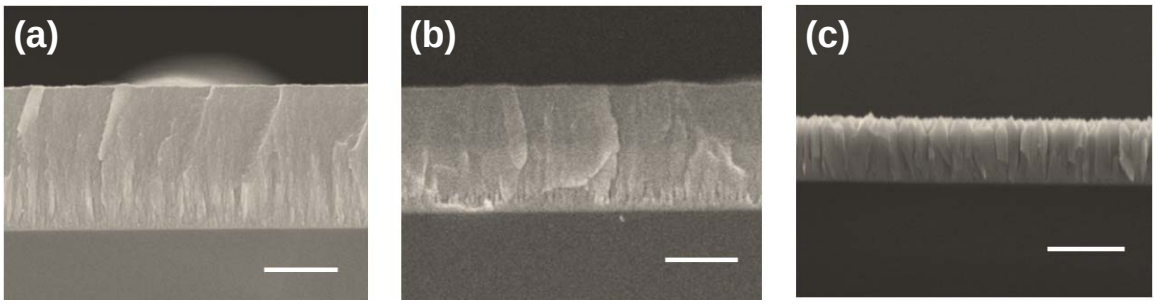

Figure 2.22. SEM images of ZnO thin films deposited by PECVD at 600˚C and 3.5 Torr. The applied rf powers were (a) 20 W, (b) 30 W and (c) 40 W, respectively. The scale bars are 500 nm.

Volintiru et al. suggested a tentative model for the ZnO film growth by PECVD. They suggested that the electrical and structural properties of films evolve as film growth goes on.[17] To investigate the evolution of film morphology with film thickness, different thickness ZnO films were deposited at the standard process conditions (Table 2.2) by adjusting the deposition time. The cross sectional SEM images of these films with different thicknesses are shown in Figure 2.23. After initial film growth [Figure 2.23 (a)], the film grows in columnar morphology [Figure 2.23 (b)] but then becomes continuous after its thickness reaches > 300 nm [Figure 2.23 (c) and (d)]. The two film growth modes, columnar and contimuous morphology, seem to compete each other in ZnO depostion by PECVD. The growth with columnar structure is dominant below 300 nm thickness but continuous morphology becomes dominant as the film thickness increases above 300 nm. Figure 2.24 shows the FWHM of the XRD peaks ($\Delta 2\theta$) and rocking curves ($\Delta\omega$). The XRD measurements show that the FWHM of both the XRD peaks and the rocking curves decrease with increasing film thickness until the films reach ~ 500 nm. However, further film growth increases the FWHM. The grain size increases and

crystallinity improves during the initial film growth until the film thickness reaches ~ 500 nm but further film growth decreases the grain size and crystallinity worsens.

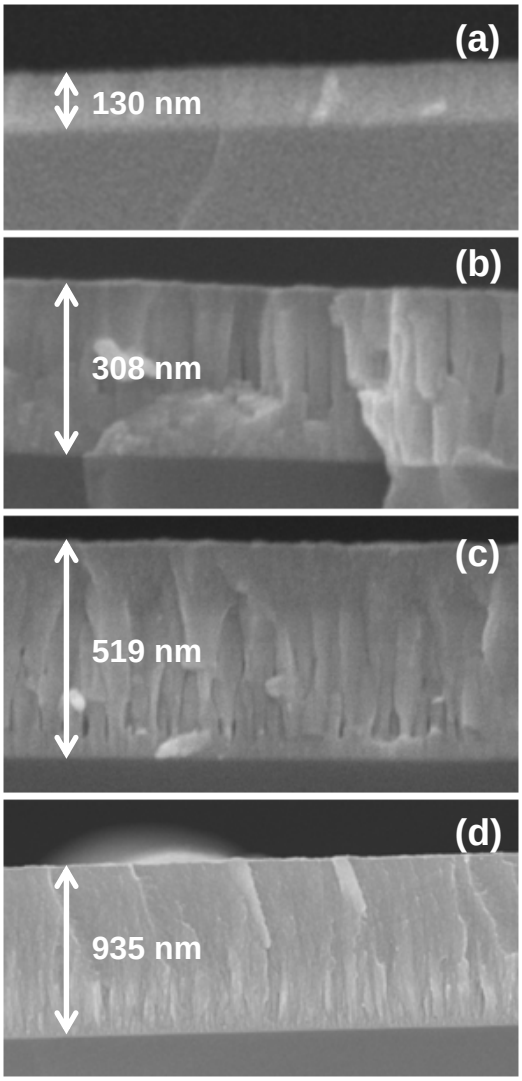

Figure 2.23. The cross sectional SEM images of ZnO films deposited by PECVD with different thicknesses. The films were deposited at standard conditions (Table 2.2) for (a) 30 min, (b) 60 min, (c) 90 min and (d) 120 min.

To investigate the dependence of the electrical properties on film thickness, carrier concentration, mobility and resistivity were determined by using Hall-effect measurements with Van der Pauw configuration. Figure 2.25 shows the mobility, carrier concentration and resistivity as a function of film thickness. The mobility increases and carrier concentration decreases with increasing film thickness from ~ 100 nm to ~ 900 nm. The mobility of polycrystalline thin film is affected by carrier scattering mechanisms such as grain boundary scattering and ionized defect scattering.[20,21,22] The increase in mobility with increasing film thickness may be due to the reduced grain boundary scattering because of the grain size increase which is indecated by the narrowed FWHM of XRD peaks [Figure 2.24].

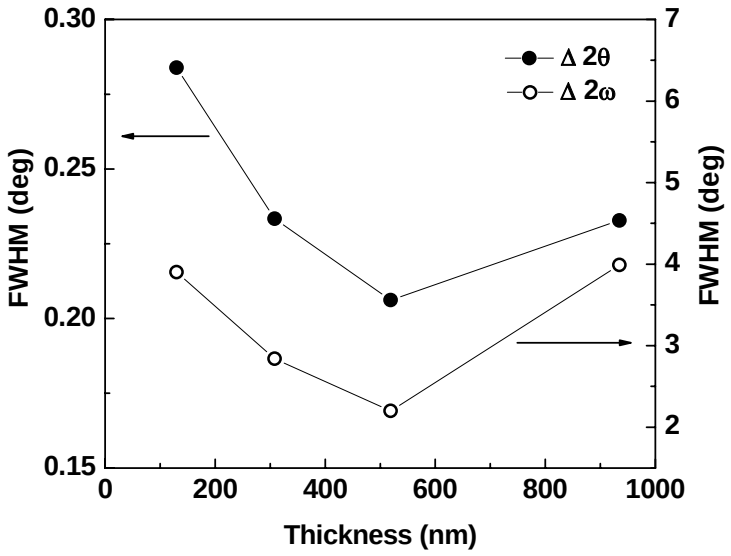

Figure 2.24. The plot of FWHM of XRD θ-2θ scans and rocking curves of ZnO films versus film thickness. The measurements were conducted on the same films in Figure 2.23.

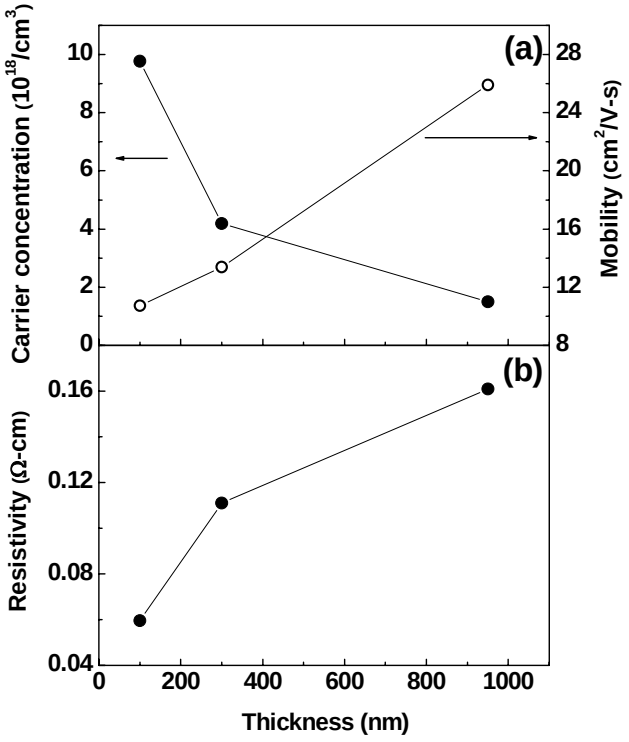

Figure 2.25. (a) Carrier concentration and mobility and (b) resistivity as a function of ZnO film thickness. Films were deposited by PECVD on silicon under standard process conditions (Table 2.2). Film thickness was varied by adjusting the deposition time : 30 min, 60 min and 120 min, respectively in the order of thickness.

2.5.2 Effect of deposition pressure on the film morphology and optical transmittance

Volintiru et al. reported that the pressure plays an important role in determining the ZnO film morphology in PECVD.[17] Specifically, deposition at low pressures produces films with smooth surfaces and small grains while deposition at high pressures

produces films with rough surfaces and large grains. To investigate the effect of pressure on the film morphology, ZnO films were deposited under standard conditions (Table 2.2) but at 3.6 Torr and 1.5 Torr. The SEM images and XRD from the films are shown in Figure 2.26 and Figure 2.27, respectively. The film deposited at high pressure (3.6 Torr) shows columnar morphology and an intense XRD peak while the film deposited at low pressure (1.5 Torr) shows a continuous cross section with smooth surface but a very weak XRD peak. The FWHM of the $(0002)_{ZnO}$ XRD peak increases as deposition pressure decreases. Although the film deposited at low pressure shows smooth surface and continuous cross section, the grain size decreases and the film crystallinity becomes worse.

Optical transmittance of ZnO films were measured by depositing films on glass substrates. Figure 2.28 shows the effect of deposition pressure on the optical transmittance of films. The films with smooth surface continuous cross sections (deposited at 1 Torr and 1.5 Torr) were brown colored and the film transmittances were significantly reduced in the visible region. The film with columnar morphology (deposited at 3.7 Torr) is transparent above 380 nm (~ 3.4 eV, ZnO band gap). The absorption of the ZnO films in the visible region may be due to carbon incorporation into the growing film at low pressure. The metal-organic precursor may not be completely oxidized at low deposition pressure. In conclusion, deposition at low pressure yields continuous and smooth film but the transmittance of the films in the visible region is severely reduced.

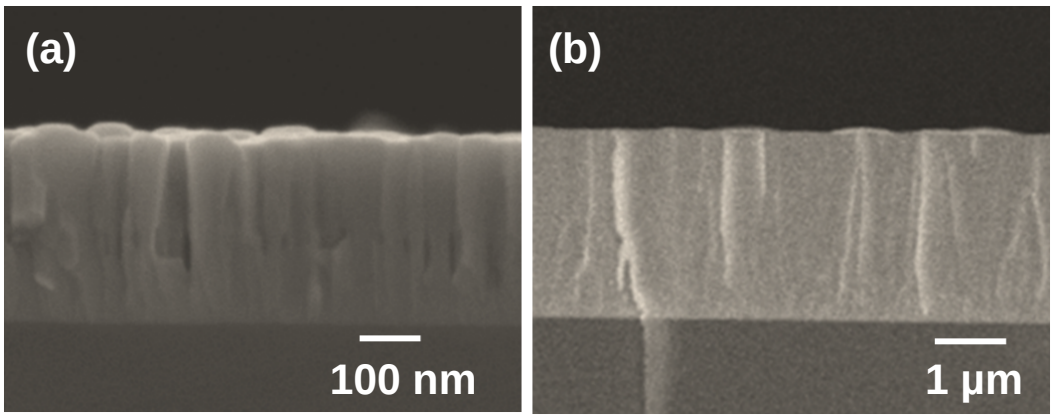

Figure 2.26. The SEM images of ZnO thin films deposited by PECVD on silicon. The films were deposited under standard conditions (Table 2.2) but at (a) 3.6 Torr and (b) 1.5 Torr.

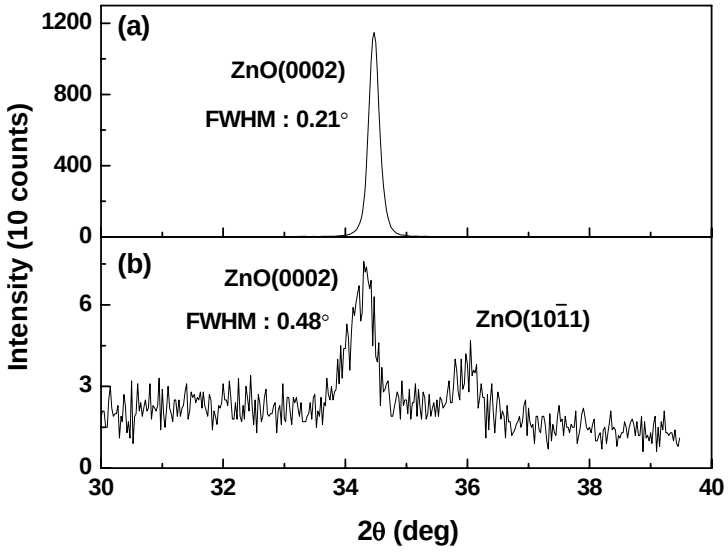

Figure 2.27. The XRD of films deposited under standard conditions (Table 2.2) but at (a) 3.6 Torr and (b) 1.5 Torr. The measured films are same as shown in Figure 2.26.

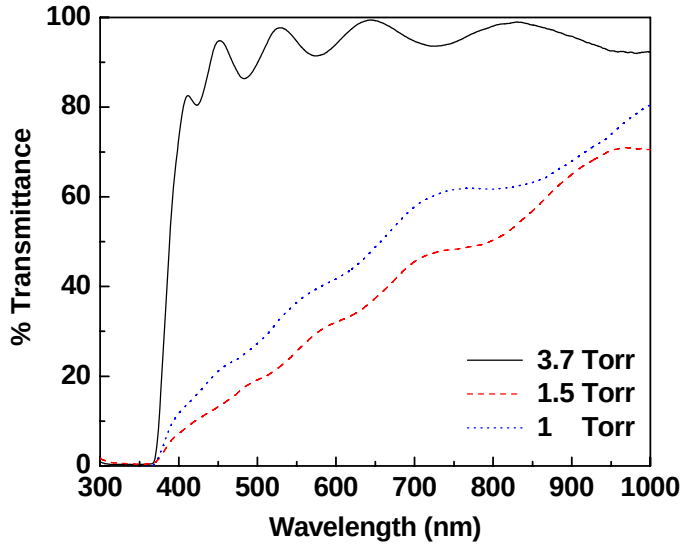

Figure 2.28. The effect of pressure on the optical transmittance of thin ZnO films deposited by PECVD on glass.

References

[1] Klaus Ellmer, J. Phys. D Appl. Phys. **33**, R17 (2000).

[2] Y. Chen, D. M. Bagnall, H. Koh, K. Park, K. Hiraga, Z. Zhu, T. Yao, J. Appl. Phys. **84**, 3912 (1998).

[3] A. Ohtomo, A. Tsukazaki, Semicond. Sci. Tech. **20**, S1 (2005).

[4] B.P. Zhang, N.T. Binh, K. Wakatsuki, N. Usami, Y. Segawa, Appl. Phys. A **78**, 25 (2004).

[5] B. Cao, W. Cai, H. Zeng, G. Duan, J. Appl. Phys. **99**, 073516 (2006).

[6] J. B. Mooney, S. B. Radding, Annu. Rev. Mater. Sci. **12**, 81 (1982).

[7] J. B. Baxter, E. S. Aydil, J. Cryst. Growth **274**, 407 (2005).

[8] B. S. Li, Y. C. Liu, Z. S. Chu, D. Z. Shen, Y. M. Lu, J. Y. Zhang, X. W. Fan, J. Appl. Phys. **91**, 501 (2002).

[9] M. Ohring, Materials Science of Thin Films, Academic press, USA, P. 279, 2002.

[10] R. Triboulet, 10th European Workshop on MOVPE, Lecc (Italy) 8-11 June (2003).

[11] M. Kim, Y. Hong, J. Yoo, G. Yi, G. Park, K. Kong, H. Chang, Phys. Stat. sol. (RR) **2**, 197 (2008).

[12] P. Kung, C.J. Sun, A. Saxler, H. Ohsato, M. Razeghi, J. Appl. Phys. **75**, 4515 (1994).

[13] J. Q. Xie, J. W. Dong, A. Osinsky, P. P. Chow, T. W. Heo, D. P. Norton, S. J. Pearton, X. Y. Dong, C. Adelmann, C. J. Palmstrom, Mater. Res. Soc. Symp. P. **891**, 407 (2006).

[14] H. Karzel, W. Potzel, M. Köfferlein, W. Schiessl, M. Steiner, U. Hiller, G. M. Kalvius, D. W. Mitchell, T. P. Das, P. Blaha, K. Schwarz, M. P. Pasternak, Phys. Rev. B **53**, 11425 (1996).

[15] D. C. Kim, B. H. Kong, H. K. Cho, D. J. Park, J. Y. Lee, Nanotechnology **18**, 015603 (2007).

[16] J. H. Park, S. J. Jang, S. S. Kim, B. T. Lee, Appl. Phys. Lett. **89**, 121108 (2006).

[17] I. Volintiru, M. Creatore, B. J. Kniknie, C. I. M. A. Spee, M. C. M. Sanden, J. Appl. Phys. **102**, 043709 (2007).

[18] B. S. Li, Y. C. Liu, D. Z. Shen, Y. M. Lu, J. Y. Zhang, X. G. Kong, X. W. Fan, Z. Z. Zhi, J. Vac. Sci. Technol. A **20**, 265 (2002).

[19] Y. J. Kim, H. J. Kim, Mater. Lett. **21**, 351 (1994).

[20] T. Minami, MRS Bull. **25**, 38 (2000).

[21] K. Ellmer, G. Vollweiler, Thin Solid Films **496**, 104 (2006).

[22] M Chen, Z L Pei, X Wang, Y H Yu, C Sun, L S Wen, J. Phys. D Appl. Phys. **33**, 2538 (2000).

Chapter 3

Properties of ZnO thin films deposited by radio frequency magnetron sputtering

3.1 Introduction

Magnetron sputtering is a physical vapor deposition (PVD) method which makes use of the ions created in a plasma to transfer materials from a source called target to a substrate. Ions are accelerated towards to target by an electric field and sputter material by impinging on the target. Ejected material is deposited on substrates placed across from the target. A major difference between magnetron sputtering and other thin film deposition techniques such as thermal evaporation and chemical vapor deposition is that much higher energy can be input into the growing films with low substrate temperature because high energy ions in plasma also impinge on the growing film. Thus, the deposition of high quality films with low substrate temperature is possible.[1,2] In addition to the low deposition temperature, magnetron sputtering has advantage on alloy and compound deposition by making use of compound target or co-sputtering and it is easy to scale up to the large size substrate.

Metal oxide thin film deposition by magnetron sputtering can be achieved in two ways. First, a metal oxide target same as the material to be deposited is used. Second

method is called reactive sputtering wherein a metal target is sputtered in the presence of a reactive gas such as oxygen.[3,4] Metal oxide target is usually an insulator and sputtering requires radio frequency (rf) power. While this lowers the deposition rate, the process is simple and easy. Reactive sputtering allows one to vary the electrical and optical properties of the deposited films in a wide range by adjusting the process conditions[5,6] such as the reactive gas partial pressure, substrate to target distance and applied power.

In this chapter, the structure and optical and electrical properties of ZnO thin films deposited by rf magnetron sputtering are described. The dependence of film properties on key process parameters such as oxygen to argon gas flow rate ratio and deposition temperature is discussed and the effects of post treatments such as thermal annealing and oxygen plasma exposure on the film properties are also presented.

3.2 Radio frequency magnetron sputtering for ZnO thin film

Zinc oxide thin films were deposited by rf magnetron sputtering system (AJA international inc., ATC 2000) from an undoped ZnO target (Williams advanced materials, ZnO 99.995%) on soda lime glass substrates (microscope slides). The bell jar type deposition chamber is evacuated by a cryogenic pump which provides a base pressure of ~ 10^{-7} Torr. The sputtering system has 4 shuttered guns (2 dc-powered guns and 2 rf-powered guns). A 3-inch-diameter ZnO target is equipped to one of the rf guns. The 3-inch-diameter target is positioned off the chamber center axis to accommodate four guns and the target face is tilted toward the sample stage as illustrated in Figure 3.1. To improve the uniformity of the film thickness, the sample stage is rotated during the

deposition. Three process gases (Ar, O_2 and N_2) can be introduced into the deposition chamber through separate lines and the flow rates are controlled independently by mass flow controller (MFC). During sputtering Ar plasma was maintained with 200 W of rf-power at 5 mTorr pressure. The substrate was heated with halogen lamps located at beneath the substrate holder and the temperature was controlled by a closed-loop feedback controller in conjunction with a K-type thermocouple. The sputtering system is computer operated and process recipes could be programmed and executed automatically. The diagram of the sputter deposition system is showed in Figure 3.1 and the process conditions used in this study are listed in Table 3.1.

Table 3.1. Sputtering process conditions for ZnO thin film. The target is undoped ZnO and substrates are soda lime glasses (microscope slides).

Process factor	values
rf power (W)	200
Deposition temperature (˚C)	Room temperature, 350
Ar / O_2 flow rate (sccm)	20/0, 19/1, 17/3, 15/5
Process pressure (mTorr)	5

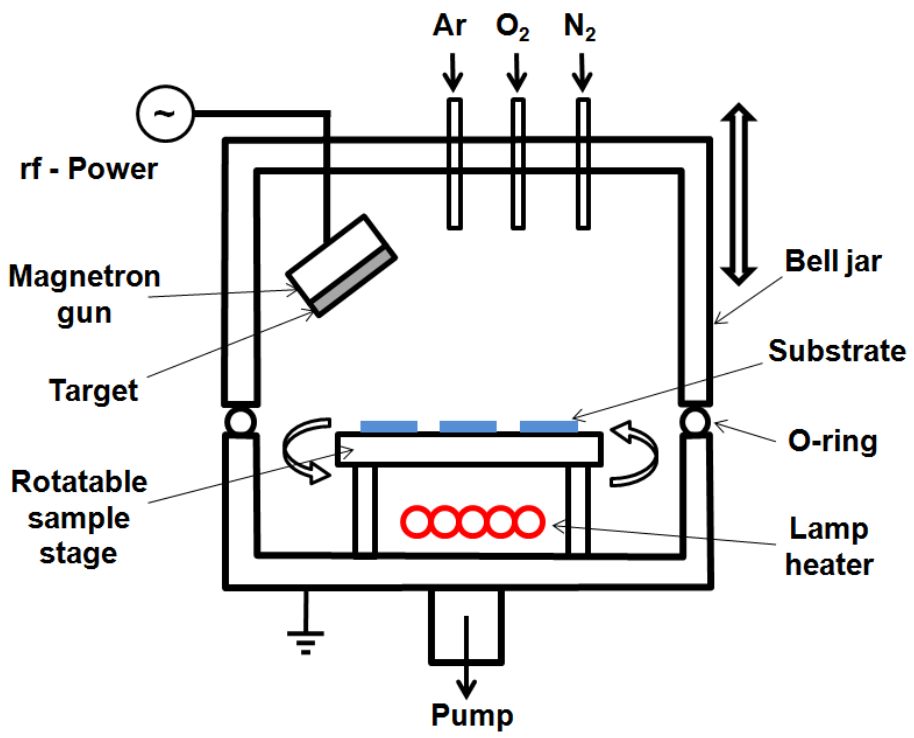

Figure 3.1. A schematic of the magnetron sputtering system for ZnO thin film deposition.

3.3 The structure and optical properties of sputtered ZnO films

Figure 3.2 and 3.3 show a typical XRD and an SEM cross sectional image of a ZnO film sputtered onto a glass substrate. The films deposited under different process conditions within the process parameter range shown in Table 3.1 resulted films with similar XRD and looked the same under SEM. Specifically the XRD shows only the $(0002)_{ZnO}$ diffraction indicating a textured structure with c-axis perpendicular to the substrate surface. SEM images support this conclusion and show a columnar film morphology with smooth surface.

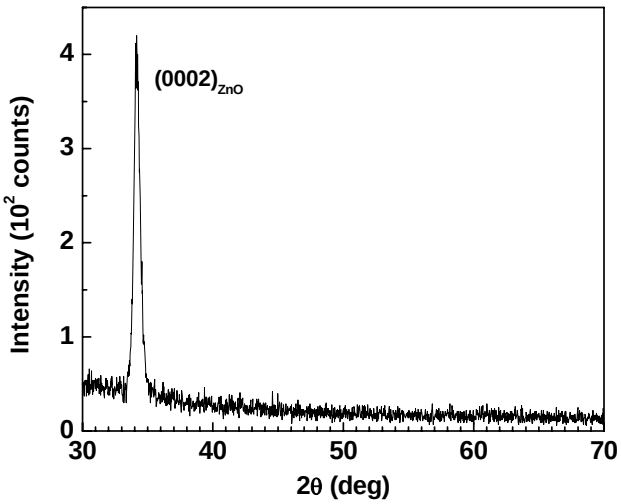

Figure 3.2. XRD from a ZnO thin film sputtered at room temperature on glass substrate. The argon and oxygen flow rates were 19 and 1 sccm, respectively.

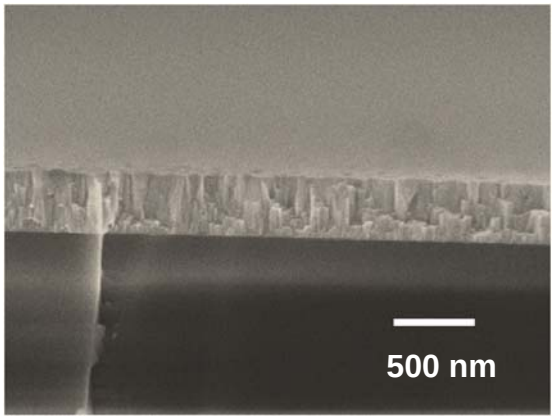

Figure 3.3. SEM image of a ZnO film sputtered onto a glass substrate at room temperature. The argon and oxygen flow rates were 19 and 1 sccm, respectively and the deposition time was 7560 seconds.

Figure 3.4 shows the optical transmittance of three sputtered ZnO films. The three films had different thickness which was varied by adjusting the deposition time.

Sputtering for 1680 s, 3360 s and 7560 s resulted in films that were 133 nm, 277 nm and 386 nm, respectively. The average sputtering rate was ~ 5 nm/min during the first ~ 10 minutes but decreases for longer deposition time to ~ 3 nm/min. The transmittance is almost zero in the ultra violet (UV) region and increases abruptly at around 380 nm indicating the optical band gap of ~ 3.4 eV. The flims are transparent in visible region for wavelength > 400 nm. The 133 nm thick flim is still transparent below 380 nm because the film is still to thin to absorb all the incident light. The interference fringes apprear in thicker films (277 nm and 386 nm) above 380 nm and indicate that the films have smooth surface. The spacing of the fringes are consistent with the film thickness which was determinted by SEM.[7]

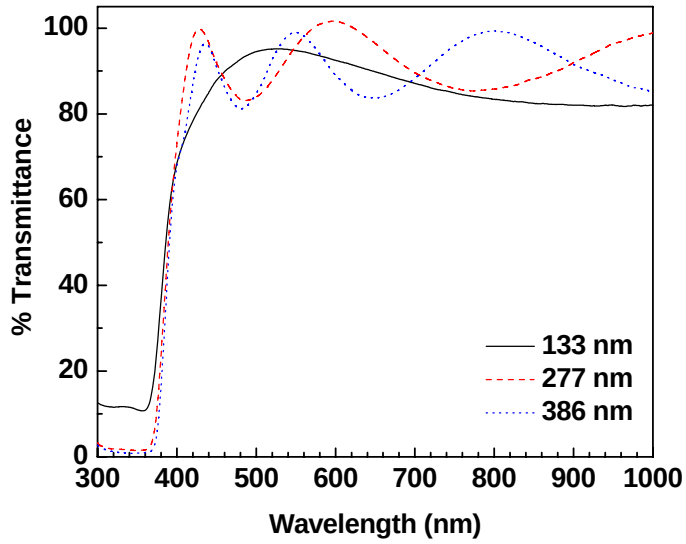

Figure 3.4. The transmittance of ZnO films of varying thickness sputtered at room temperature on glass. The argon and oxygen flow rates were 19 sccm and 1 sccm, respectively.

The ratio of oxygen-to-argon gas flow rate is known as one of the critical process parameters in oxide thin film deposition.[8,9] Accordingly we investigated the dependence of the film structure and optical properties on the ratio of oxygen-to-argon gas flow rates. ZnO films were sputtered under various gas flow rate ratios (Table 3.1). The films were deposited on glass substrate at room temperature for 1680 sec at an average rate of ~ 4 nm/min. Figure 3.5 shows the lattice parameter, c and grain sizes of the ZnO films deposited at various gas flow rate ratios. The lattice parameters are calculated from the $(0002)_{ZnO}$ XRD peak position and grain sizes were estimated from the FWHM of the same peaks using Debye-Scherrer formula. The lattice parameters for all the films were around 5.250 ± 0.003 Å which is different from the equilibrium value, 5.2038Å.[10] This lattice parameter offset from the equilibrium value may be due to stress in the films. Assuming that the volume of unit cell is the same, the larger lattice parameter, c, implies that the lattice is compressed in the a-direction and the films sputtered at room temperature seem to be under compression parallel to the a-direction.

Figure 3.6 shows the deposition rate as a function of O_2 concentration in the feed gas. The deposition rate decreases as the concentration of oxygen in the feed gas increases and this is a typical trend of reactive sputtering with O_2. In reactive sputtering from a metal target, the taget surface remains metallic under low oxygen partial pressure and the deposition rate remains high because of the high sputtering yield of metals. However, as the oxygen partial pressure increases the target surface oxidizes which reduces the sputtering and, hence, the deposition rate.[1,11]

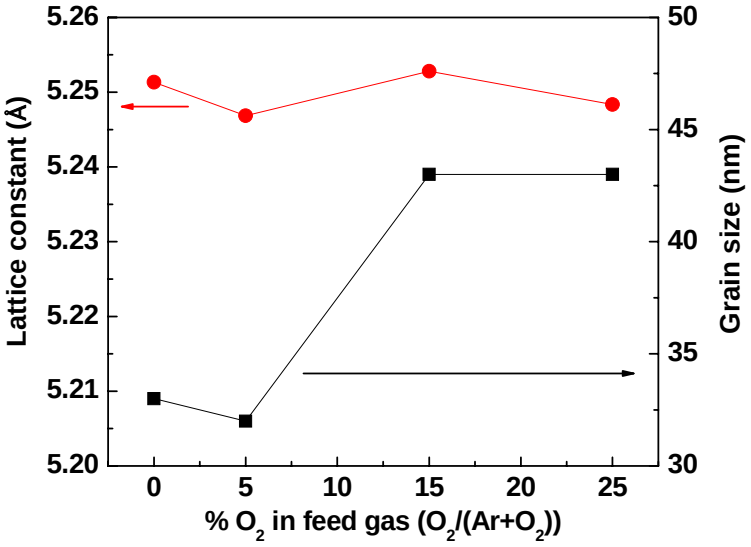

Figure 3.5. The plot of lattice constant, c, and grain sizes of ZnO films versus the concentration of O_2 in feed gas. The grain sizes are calculated by Sherrer's formula from FWHM's of $(0002)_{ZnO}$ peaks.

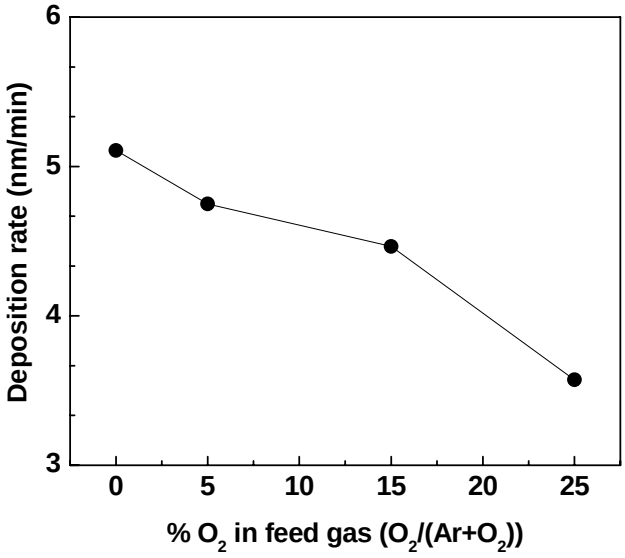

Figure 3.6. The plot of film deposition rate versus the concentration of O_2 in feed gas.

3.4 Effect of post sputtering annealing on the structure and electrical properties of ZnO thin films

The fact that deposition temperature and oxygen partial pressure during deposition have an important role on the structure and electrical properties of sputtered ZnO thin films[12,13,14] hints that the film quality can be improved by post-deposition annealing. Two kinds of post deposition annealing were tried here, thermal annealing and oxygen-plasma annealing.[15,16] To investigate the effect of these post-deposition annealing treatments on the films' electrical and structural properties, ZnO films were sputtered at room temperature while varying the concentration of O_2 in the feed gas. Following, two types of annealing were implemented. One set of films were thermal annealed at 600˚C for 2 hours in vacuum. A second set of films were exposed to oxygen plasma at 600˚C for 2 hours. For both annealing treatments, the PECVD chamber described in section 2.5 was used. Oxygen plasma was generated at ~ 4.5 Torr with 40 W rf-power applied through the ring type electrode located 0.5 inch above sample surface. Oxygen gas flow rate was 400 sccm.

Figure 3.7 shows the lattice parameter, c, and the grain size of post treated ZnO films extracted from XRD $(0002)_{ZnO}$ peak as a function of oxygen concentration in the feed gas for ZnO sputtering after thermal annealing with and without oxygen plasma. The lattice parameters of the as-deposited films are far above the relaxed value of 5.2038 Å indicating that these films are stressed. The stress seems to be relieved after the annealing steps : the lattice parameter, c, relaxes to 5.2 Å. The relaxation seem to be due to thermal annealing since annealing without oxygen plasma also relaxes the stress in the films

[Figure 3.7 (a)]. The grain sizes increase by both thermal annealing with and without oxygen plasma as shown in Figure 3.7 (b).

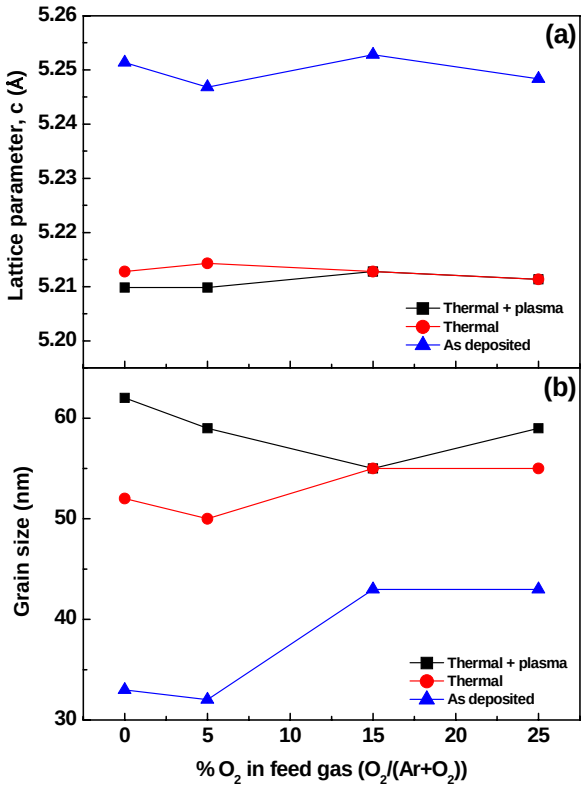

Figure 3.7. The plot of (a) lattice constant "c" and (b) grain sizes of as-deposited, thermal annealing treated and oxygen plasma with thermal annealing treated ZnO thin films versus the concentration of O_2 in feed gas.

Figure 3.8 shows the effect of the thermal annealing in presence of oxygen plasma on the lattice parameter, c, and grain size as a function of the film thickness. The lattice parameter, c, for as-deposited films decreases with increasing film thickness indicating

within the films, stress relaxes as the films get thicker. After annealing, the lattice parameter of the films approaches to the equilibrium value indicating that the film stresses are relaxed upon thermal annealing in presence of an oxygen plasma. This stress relief is much more effective on thin films (133 nm). Thicker films still exhibit lattice parameter values larger than the equilibrium value even after annealing. Annealing also increases the grain size in films as shown in Figure 3.8 (b).

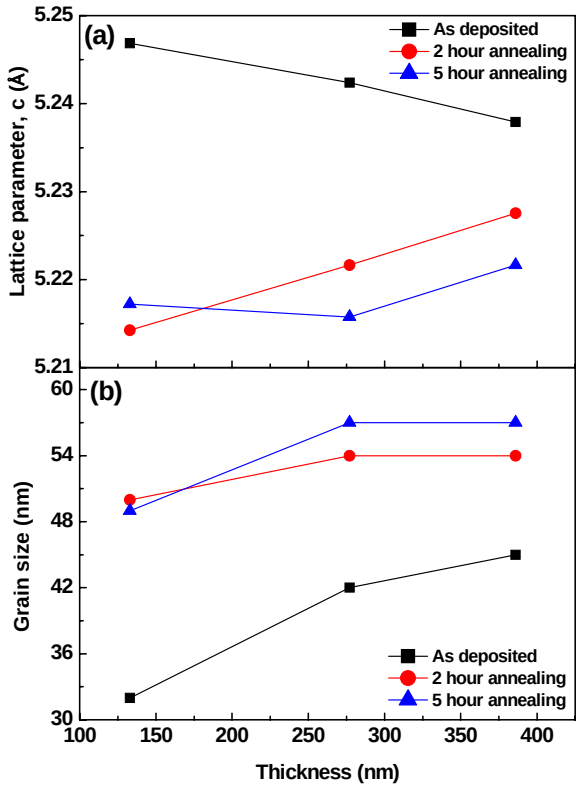

Figure 3.8. (a) Lattice parameter, c and (b) grain size of as-deposited ZnO films before and after 2 hour and 5 hour thermal annealing in presence of an oxygen plasma as a function of film thickness.

To investigate the dependence of film structure on thermal annealing temperature, ~ 100 nm thick ZnO thin films were sputtered at room temperature for 1680 sec and then thermally annealed in vacuum for 1 hour at different temperatures (150, 250, 350 and 450˚C). Figure 3.9 shows the lattice parameter, c, and grain size within these films as a function of the annealing temperature.

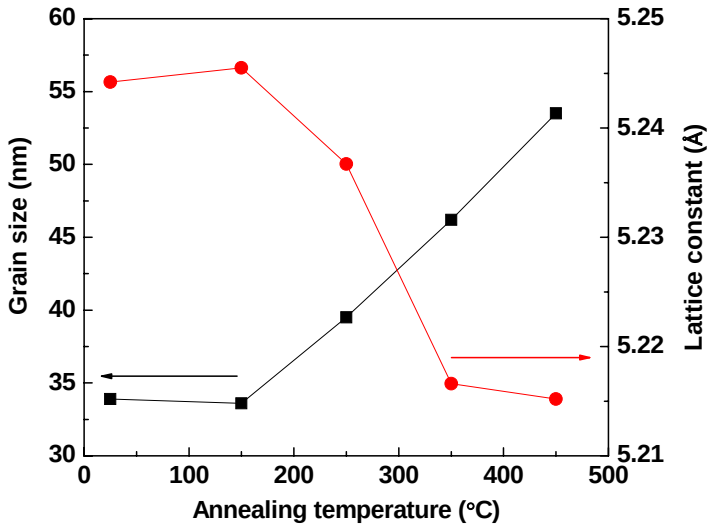

Figure 3.9. The grain size and lattice parameter, c, of ZnO films as a function of annealing temperature. The films were deposited on glass substrates at room temperature while flowing argon and oxygen at 19 sccm and 1sccm, respectively. Annealing was conducted under vacuum for 1 hour.

The lattice parameter of the films annealed at room temperature and 150˚C were approximately the same and greater than the equilibrium value. The lattice parameter decreased with annealing temperature above 150˚C and then saturated at approximately

350˚C. The grain size within these films increased monotonically with annealing temperature. The fact that the grain size and lattice parameters are similar for the films deposited at room temperature and annealed at 150˚C may be due to inevitable heating of the substrate during sputtering at room temperature : The substrate temperature is likely higher than room temperature and may be closer to 150˚C.

The surface roughness and electrical resistivity of as-deposited and thermally annealed films, both with and without oxygen plasma, were measured and are listed in Table 3.2. The films were deposited at room temperature using 19 sccm Ar and 1 sccm O_2 in feed gas. The root mean square (RMS) surface roughness was measured using atomic force microscopy (AFM) in contact mode over a 3 μm × 3 μm area. The electrical resistivity of the films was measured using contacts in the Van der Pauw configuration with current-voltage source and measure unit (Keithley 2400).

The RMS roughness of the as-deposited films was ~ 3 nm. Thermal annealing in absence of oxygen plasma had no effect on the value but when thermal annealing was done in presence of an oxygen plasma the roughness increased dramatically to ~ 8 nm. The electrical resistivity of the as-deposited films were above the limit of the measurement system (~ 10^7 Ω-cm) and thermal annealing with or without oxygen plasma did not decrease the resistivity below this limit. Conductive ZnO films are obtained only when films are sputtered at high temperature. For example, sputtering at 350˚C reduces the resistivity by 4 orders of magnitude. These results were independent of film thickness in the range ~ 100 nm - 400 nm.

Table 3.2. Surface roughness and electrical resistivity of as-deposited and thermally annealed films. For comparison, the values for a film deposited at 350˚C are also presented. Film thickness is the sample thicknesses which are used in resistivity measurement.

Sample	RMS roughness (nm)	Resistivity (Ω-cm)	Film thickness (nm)
As deposited at RT	2.7	$> 10^7$	100/125/133/143
Thermal annealing (at 600˚C for 2hrs)	3.9	$\sim 10^7$	133/277/386
Oxygen plasma with thermal annealing (at 600˚C for 2hrs)	7.9	$> 10^7$	133
As deposited at 350˚C	7.7	4×10^3	544

References

[1] K. Ellmer, J. Phys. D Appl. Phys. **33**, R17 (2000).

[2] M. Ohring, Materials Science of thin films, Academic press, USA, 2002.

[3] Q. Ma, Z. Ye, H. He, L. Zhu, J. Wang, B. Zhao, Mater. Lett. **61**, 2460 (2007).

[4] S. B. Krupanidhi, M. Sayer, J. Appl. Phys. **56**, 3308 (1984).

[5] V. Tvarozek, K. Shtereva, I. Novotny, J. Kovac, P. Sutta, R. Srnanek, A. Vincze, Vacuum **82**, 166 (2008).

[6] M.Chen, Z. L. Pei, X. Wang, C. Sun, L. S. Wen, J. Vac. Sci. Technol. A **19**, 963 (2001).

[7] R. Swanepoel, J. Phys. E Sci. Instrum. **16**, 1214 (1983).

[8] M. Chen, Z. L. Pei, C. Sun, J. Gong, R. F. Huang, L. S. Wen, Mater. Sci. Eng. **B85**, 212 (2001).

[9] S. Brehme, F. Fenske, W. Fuhs, E. Nebauer, M. Poschenrieder, B. Selle, I. Sieber, Thin Solid Films **342**, 167 (1999).

[10] R. T. Downs, K. L. Bartelmehs, G. V. Gibbs, Am. Mineral. **78**, 1104 (1993).

[11] Z. Li, W. Gao, Mater. Lett. **58**, 1363 (2004).

[12] E. Mirica, G. Kowach, P. Evans, H. Du, Cryst. Growth Des. **4**, 147 (2004).

[13] N. Tsuji, H. Komiyama, K. Tanaka, J. J. Appl. Phys. **29**, 835 (1990).

[14] G. Xiong, J. Wilkinson, B. Mischuck, S. Tuzemen, K. B. Ucer, R. T. Williams, Appl. Phys. Lett. **80**, 1195 (2002).

[15] M. Liu, H. K. Kim, Appl. Phys. Lett. **84**, 173 (2004).

[16] B. Angadi, H. C. Park, H. W. Choi, J. W. Choi, W. K. Choi, J. Phys. D Appl. Phys. **40**, 1422 (2007).

Chapter 4

Properties of Cu_2O thin film deposited on ZnO by metal organic chemical vapor deposition*

4.1. Introduction

Cuprous oxide (Cu_2O) is one of the oldest known and studied semiconductors and may find applications in light emitting diodes[1], spintronics,[2] catalysis[3] and solar cells.[4,5,6] Cu_2O has been considered as a potential light absorber in solar cells[4,5,6] because it has high optical absorption coefficient,[7] high room temperature mobility and long minority carrier diffusion length.[8] Cu_2O thin films grown by methods such as thermal oxidization of copper[9], sputtering[10] and electrodeposition[11], have been used make solar cells.[12,13,14] The first Cu_2O solar cells were Schottky diodes based on metal-Cu_2O junctions but these suffered from high density of interfacial states and consequently poor photovoltaic properties. A homo p-n junction could not be constructed because as deposited Cu_2O films are always p-type and a reproducible n-type Cu_2O could not be made.[15]

Recently, solar cells based on metal oxides and in particular, heterojunctions of Cu_2O with other n-type oxides are attracting attention because of their abundance and nontoxicity.[16] ZnO-Cu_2O heterojunction may be particularly attractive because, unlike

* Portions of this chapter were published in: S. Jeong, E. S. Aydil, J. Cryst. Growth **311**, 4188 (2009)

Cu_2O, as-deposited ZnO films are always n-type.[17,18] Although the theoretical power conversion efficiency limit based on the Shockley-Queissier limit is ~ 20 %,[19] the reported efficiencies have not yet exceeded 2 %. Poor quality of films and the resulting heterointerface have been blamed for the low efficiency and these properties depend critically on the deposition methods and conditions. ZnO-Cu_2O heterojunction may also find applications in optoelectronic devices such as light emitting diodes.

In this chapter, the properties of Cu_2O thin films deposited by metal organic chemical vapor deposition (MOCVD) on ZnO coated glass substrates are described. Using X-ray diffraction (XRD) and Hall-effect measurements, the dependence of structural and electrical properties of films on substrate temperature and film thickness was investigated. Especially it is shown that Cu_2O thin films grown by MOCVD on ZnO have heteroepitaxy, $(220)_{Cu2O} \parallel (0002)_{ZnO}$; $[001]_{Cu2O} \parallel [1\bar{2}10]_{ZnO}$, in spite of the fact that Cu_2O and ZnO have different crystal structures, cubic and hexagonal.

4.2. The structure and electrical properties of Cu_2O films on ZnO

4.2.1. Experiment

ZnO coated glass substrates were prepared by radio frequency (rf) magnetron sputtering from undoped ZnO target at room temperature. Microscope slide glasses were

used as substrates. During sputtering, the argon plasma was maintained using 200 W rf power at 5 mTorr. The ZnO film thickness varied from 100 to 300 nm by changing the deposition time; the sputtering rate was ~ 3.6 nm/min. Cu_2O films were deposited on these ZnO-coated glass substrates using the MOCVD system shown in Figure 4.1 from copper(II) hexafluoroacetylacetonate [$Cu(C_5HF_6O_2)_2$, $Cu(hfac)_2$]. Solid $Cu(hfac)_2$ powder was placed in a small cylindrical copper container and heated up to 65˚C. The sublimed $Cu(hfac)_2$ vapor was delivered by flowing 5 sccm (standard cubic centimeter per minute) argon gas through this $Cu(hfac)_2$ container. The $Cu(hfac)_2$ vapor with Ar carrier gas flowed into the reaction chamber through a 3"-diameter showerhead type gas distributor placed 2.5 cm across from substrate. Both oxygen gas (300 sccm) and water vapor (~ 120 sccm) were also introduced into the chamber as oxidants but through separate inlets from the $Cu(hfac)_2$ to prevent premature homogeneous gas phase reactions in the feed lines. Argon (carrier gas) and oxygen flows were controlled by mass flow controller (MFC) while water vapor flow rate was controlled using a needle valve. The water vapor flow rate was estimated from the pressure increase in the chamber. Water vapor was necessary to get high deposition rates. No deposition was observed even after 60 minutes without water. $Cu(hfac)_2$ and water vapor feed lines were heated to prevent condensation. Substrate was placed on top of a heated stage whose temperature was controlled using a feedback temperature controller. During deposition the total chamber pressure was controlled by butterfly valve in front of the pump.

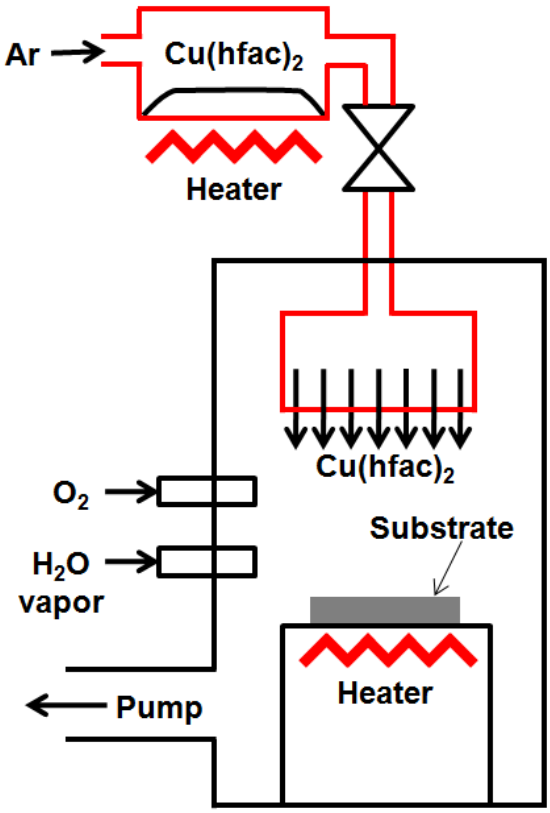

Figure 4.1. Schematic of the MOCVD system for Cu_2O deposition.

Crystal structure of the deposited films were investigated using XRD and in particular diffraction of CuKα1 radiation from the films. Film morphology was examined using scanning electron microscopy (SEM). Carrier density and mobility were determined from room temperature Hall-effect measurements using the Van-der-Pauw configuration and gold contacts. Optical absorption was measured in transmission using a combination of deuterium and tungsten halogen lamps (DH–2000–BALL) and a spectrometer (Ocean Optics HR2000) in the 200 – 1100 nm range.

4.2.2. Results and discussion

ZnO thin films sputtered on amorphous glass substrates show textured structure with (0002) direction parallel to substrate normal. XRD from Cu_2O films deposited on these substrates by MOCVD show only the Cu_2O phase without any detectable CuO and the films have preferred orientation with $(220)_{Cu_2O} \parallel (0002)_{ZnO}$ [Figure 4.2 (a)]. If the ZnO film surface was rough the deposited Cu_2O also showed the orientation of $(200)_{Cu_2O} \parallel (0002)_{ZnO}$. It was discovered that smooth ZnO surfaces with root mean square (RMS) roughness smaller than 4 nm across a 3 μm × 3 μm area consistently lead to Cu_2O films with $(220)_{Cu_2O} \parallel (0002)_{ZnO}$ [Figure 4.2(a)] whereas Cu_2O films deposited on rougher ZnO surfaces grew with $(200)_{Cu_2O} \parallel (0002)_{ZnO}$ orientation [Figure 4.2 (b)]. Examination of the films with SEM showed that the Cu_2O films are facetted [Figure 4.2 (c)] and consisted with a polycrystalline film.

No film deposition was observed at or below a substrate temperature of 250˚C but deposition rate increased to 2.2, 4.6 and 14.3 nm/min at 300˚C, 350 and 400˚C, respectively with pressure kept at 2 Torr. The activation energy of the reaction that limits the deposition rate was estimated from an Arrhenius' plot of the deposition rate vs. 1/T and was found to be 60 kJ/mol (Figure 4.3). This value is close to the apparent activation energy of Cu_2O deposition from copper acetylacetonate $[Cu(C_5H_7O_2)_2]$, a precursor nearly identical to $Cu(hfac)_2$ wherein the F atoms are replaced by H; Condorelli et al. found this activation energy to be 48 kJ/mole and interpreted it as the activation energy for dissociative adsorption of $Cu(C_5H_7O_2)_2$.[20]

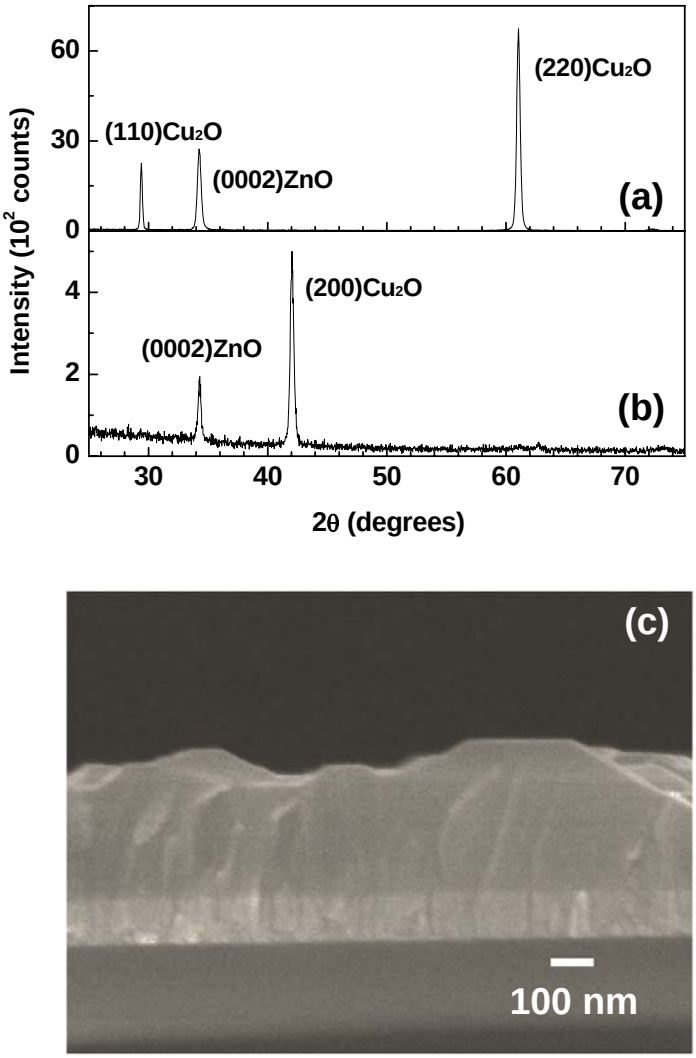

Figure 4.2. (a) and (b) are typical XRD from Cu_2O thin films deposited at 400˚C on ZnO film. (a) shows XRD of a Cu_2O film deposited on a smooth ZnO surface. The RMS roughness was 3.5 nm and (b) shows XRD from a Cu_2O film deposited on a rough ZnO surface with RMS roughness of 7.7 nm. (c) Typical SEM image of a Cu_2O film deposited by MOCVD at 400˚C. This film was deposited on ZnO coated glass substrate at a total pressure of 2 Torr for 28 minutes.

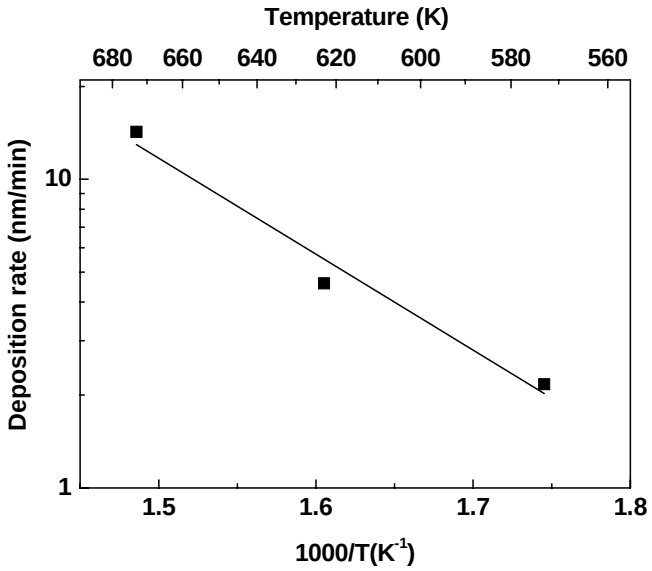

Figure 4.3. Arrhenius plot of the Cu_2O deposition rate at a deposition pressure of 2 Torr. The linear line is the fitted line.

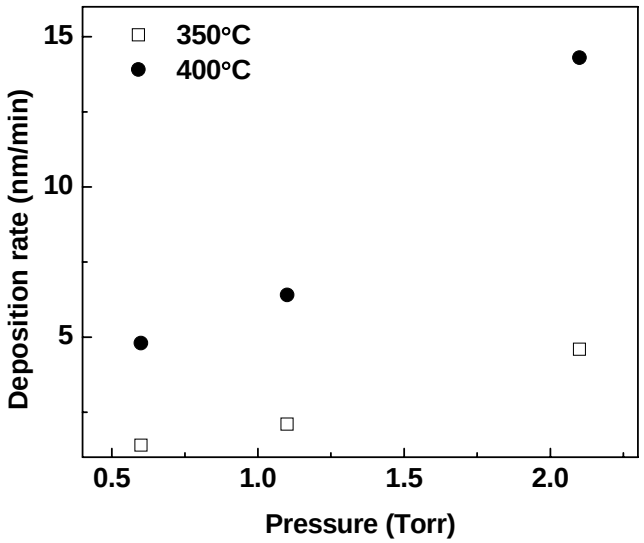

Figure 4.4. The plot of deposition rate versus process pressure. The films were deposited at two substrate temperature, 350 and 400˚C.

If the deposition is limited by dissociative adsorption of $Cu(hfac)_2$ the deposition rate should also increase with increasing partial pressure of $Cu(hfac)_2$. We increased the partial pressure of $Cu(hfac)_2$ by reducing the pumping speed with a butterfly valve while keeping the flow rates of all gases constant; this increases the deposition pressure and consequently the partial pressure of all gases including the precursor $Cu(hfac)_2$. Indeed, the deposition rate increased with pressure at constant temperature as shown in Figure 4.4.

Figure 4.5 shows the morphology and optical absorbance of the Cu_2O films deposited at temperatures ranging from 300˚C to 400˚C. Deposition durations were adjusted such that all the films in Figure 4.5 have similar thicknesses: films deposited at 300, 350 and 400˚C were 222 nm, 208 nm, and 243 nm thick, respectively. Cross sectional SEM images [Figure 4.5 (d) - (f)] show that the films deposited at low temperature (300˚C) are rough but become denser and smoother with increasing substrate temperature. The rough surface at low temperature may be a result of slow surface diffusion of the precursor adsorbate that eventually leads to Cu_2O. The rough surface affects the optical appearance of the film. The films deposited at 350˚C and 400˚C are semitransparent in the visible [Figure 4.5 (b) and (c)] but the film deposited at 300˚C [Figure 4.5 (a)] is opaque due to scattering. Even though all the films are similar in thickness, the film deposited at low temperature (300˚C) looks optically thicker [Figure 4.5 (a) - (c)] because of light scattering by the rough surface. Figure 4.5 (g) shows the optical absorbance of the films in Figure 4.5 (a) - (f). The films deposited at 350˚C and 400˚C start to absorb light at around 600 nm.

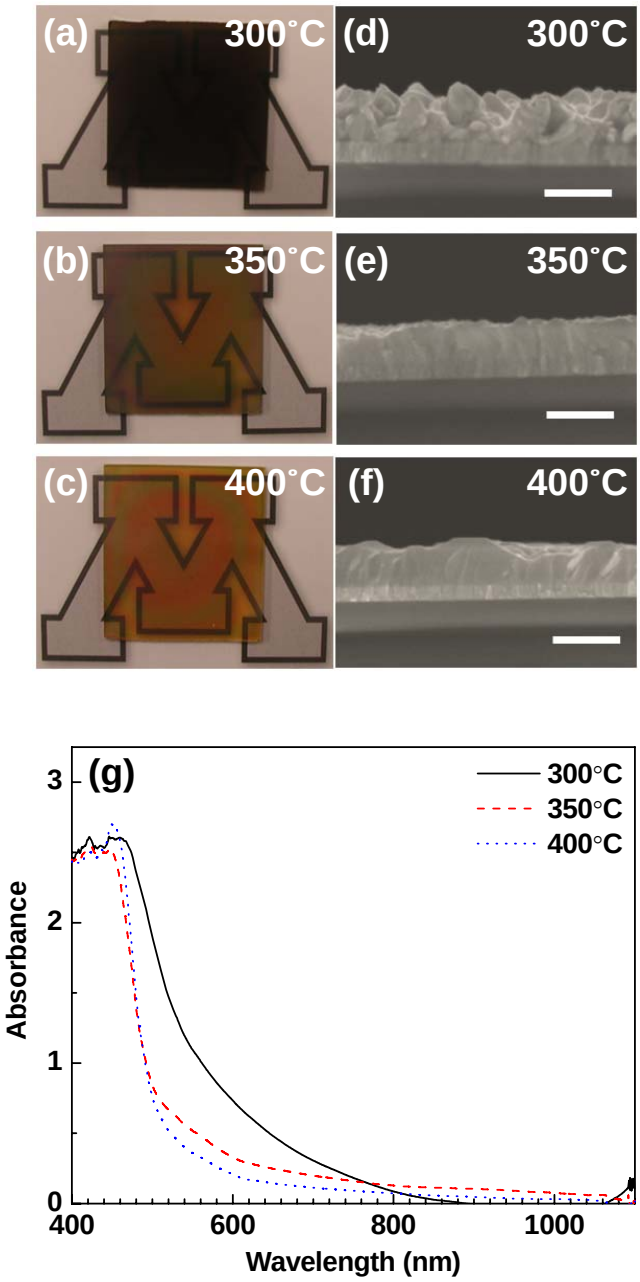

Figure 4.5. (a) - (c) Digital photographs and (d) - (f) cross sectional SEM images of Cu_2O films deposited at substrate temperatures of 300 (a, d), 350 (b, e) and 400˚C (c, f), respectively. Scale bars are 500 nm. (g) Optical absorbance of the films shown in (a) - (f).

The Tauc plot (Fig. 4.6) generated from the absorption data in Figure 4.5 (g) indicates that the optical band gap of the deposited films are around 2 - 2.2 eV near the value expected for Cu_2O which has a band gap of 2.17 eV. The absorption curve in the 2.0 - 2.2 eV range seems to have fine structure which may be resolved if the absorption measurements are done at low temperature but are smeared out at room temperature.

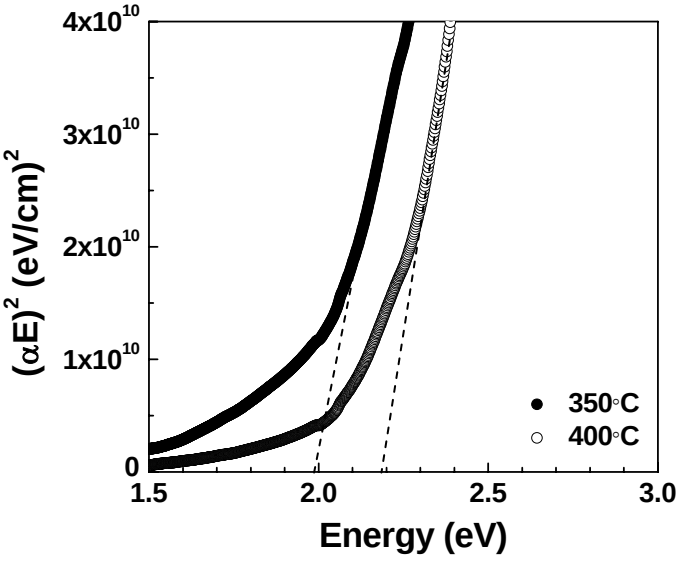

Figure 4.6. Tauc plot generated from the absorption data in Figure 4.5 for films deposited at 350˚C and 400˚C.

XRD peaks of all the Cu_2O films deposited at different substrate temperatures show only the ZnO (0002) and Cu_2O (220) diffraction peaks (Figure 4.7) and this indicates that Cu_2O grows on ZnO by MOCVD with preferred orientation and $(220)_{Cu_2O} \parallel (0002)_{ZnO}$. This orientation is different than those reported for other deposition methods

such as sputtering and electrodeposition, which result in films where $(111)_{Cu_2O}$ || $(0002)_{ZnO}$.[11,17]

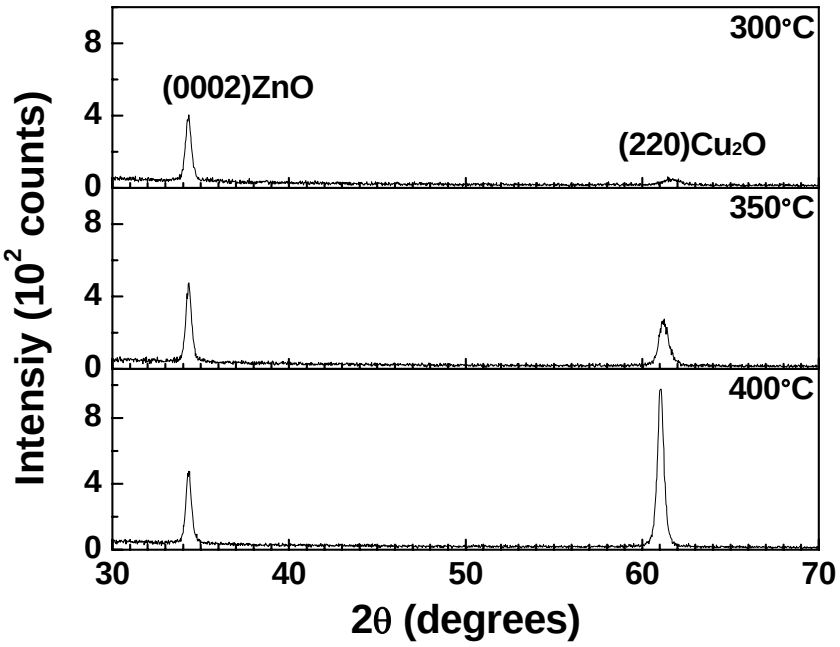

Figure 4.7. XRD peaks from the films deposited at different substrate temperatures 300, 350 and 400˚C. All the films were deposited under a total pressure of 2 Torr and the film thicknesses were made similar (222 nm, 208 nm and 243 nm respectively) by adjusting the deposition times.

Cu_2O grain size was estimated from the full width half maximum (FWHM) of the (220) XRD peak. Figure 4.8 (a) shows that the grain size increases with deposition temperature. However care is require in estimating the grain size from XRD because the XRD peak width is affected by both grain size and stress. Decreasing XRD peak width

may be due to both increasing the grain size and decreasing stress. To investigate the film stress, Cu_2O lattice constant was determined from the location of the (220) diffraction peak. The equilibrium Cu_2O bulk lattice parameter is 4.267Å. It was found that the lattice parameter of the Cu_2O films was closest to this equilibrium value when the films were deposited at 300^oC but the lattice parameter increased with increasing deposition temperature. At low temperature, the films are made up of small grains and the stress due to lattice mismatch at the interface is relaxed. At high substrate temperature, grains grow larger, crystallinity improves and epitaxy yields a smooth and oriented film with $(220)_{Cu_2O} \parallel (0002)_{ZnO}$. The increase in the intensity of the Cu_2O (220) diffraction with increasing substrate temperature (Figure 4.7) also indicates that high deposition temperature results in well oriented crystalline films. However this improvement in grain size and crystallinity increases the stress in the film. Figure 4.8 (a) shows that the lattice constant increases above the equilibrium value with increasing temperature. The film deposited at 400˚C shows ~ 0.5 % strain. Thus, the narrowing of the XRD peak is largely due to the increased grain size and not due to strain relaxation. In fact, increasing strain likely counteracts the narrowing of the XRD peak so that the grain size estimates are lower bounds.

Figure 4.8 (b) and (c) show the dependence of the carrier mobility, carrier concentration and Cu_2O film resistivity on the deposition temperature. While carrier concentration does not vary significantly with the deposition temperature, the carrier mobility increases by a factor of ten as the deposition temperature is increased from 300˚C to 400˚C. Consequently, the resistivity decreases with increasing deposition temperature. The carrier mobility in polycrystalline thin films with small grains is usually

limited by frequent scattering of the carriers at the grain boundaries. Consistent with this expectation, the increase in the carrier mobility correlates with increase in grain size and concomitant reduction in grain boundary scattering at higher deposition temperatures.

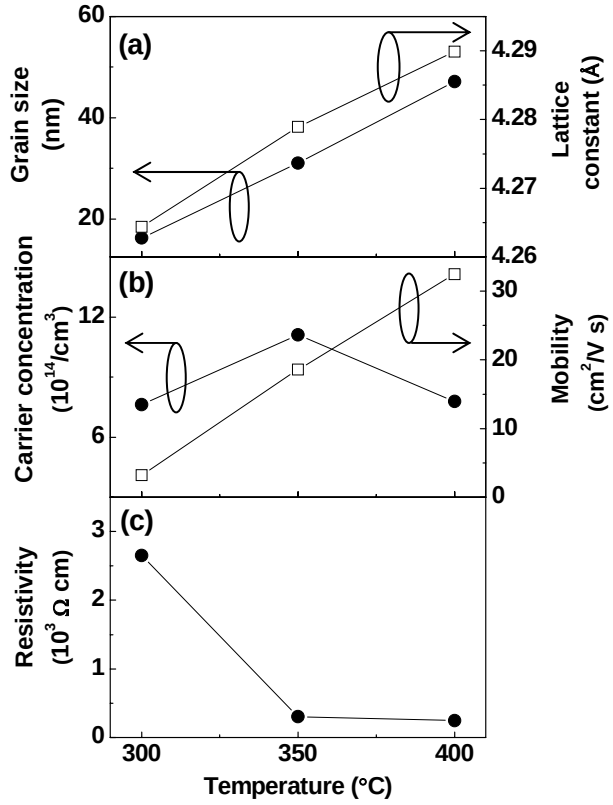

Figure 4.8. (a) Grain size and lattice parameter of the Cu_2O films as a function of deposition temperature. Equilibrium lattice constant of Cu_2O is 4.267Å. (b) Carrier concentration, carrier mobility and (c) resistivity as a function of deposition temperature.

It was discovered that the Cu_2O film properties depend on the film thickness. The XRD patterns from different thickness Cu_2O films deposited at the same substrate

temperature (350˚C) all show the same preferred orientation, $(220)_{Cu_2O} \parallel (0002)_{ZnO}$ (Figure 4.9) but the grain sizes and the Cu_2O lattice parameters determined from these XRD peaks decrease with increasing film thickness [Figure 4.10 (a)]. In particular, the lattice parameter approaches the equilibrium value for bulk Cu_2O as the film thickness increases. It appears that the stress in the films relaxes with increasing film thickness.

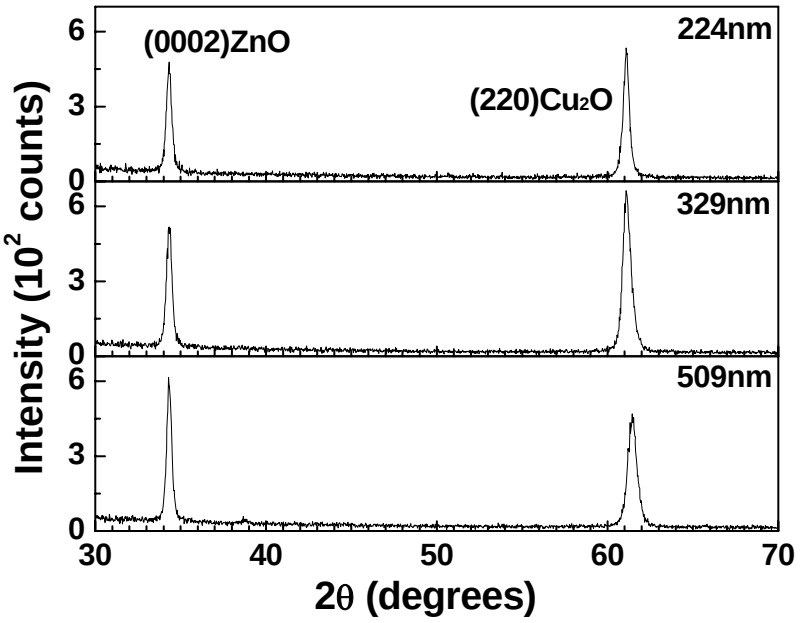

Figure 4.9. XRD from Cu_2O films deposited at the same temperature (350˚C) as a function of film thickness.

Generally, grain size is expected to increase with increasing film thickness in polycrystalline thin films but Cu_2O films deposited by MOCVD show the opposite trend. Thin Cu_2O films deposited at high temperature (~ 400˚C) have large grains and the film

develops high stress to maintain the epitaxy and the textured structure on ZnO. As films get thicker this stress is released by forming small grains and the film develops a rough surface morphology. This morphological change with film thickness has profound effect on the electrical properties of the film. Specifically, the carrier mobility decreases with increasing thickness because the grain size decreases [Figure 4.10 (b)]. Consequently, the resistivity increases with increasing film thickness [Figure 4.10 (c)].

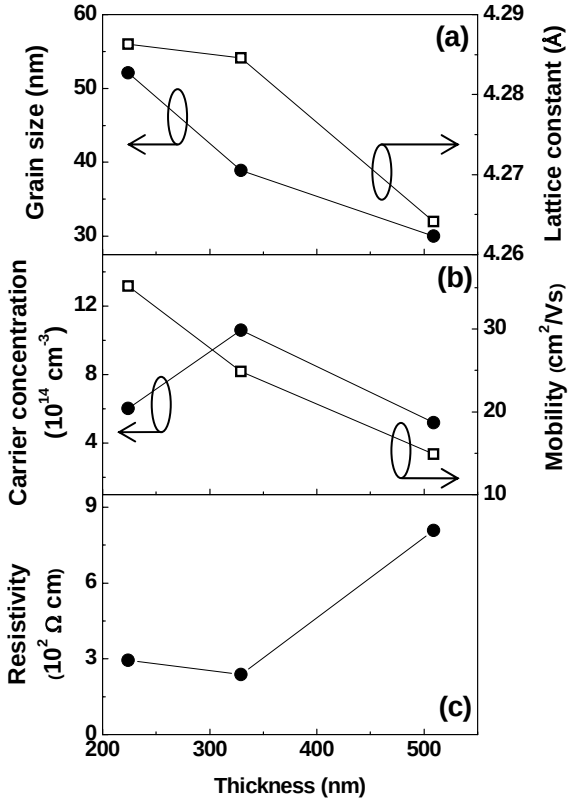

Figure 4.10. (a) Grain size and lattice parameter of the Cu_2O films as a function of film thickness. (b) Carrier concentration, carrier mobility and (c) resistivity as a function of film thickness. Deposition temperature was 350˚C for all films.

4.2.3 Conclusion

Cu_2O thin films were deposited by MOCVD on ZnO coated glass substrates from $Cu(hfac)_2$, oxygen gas and water vapor. The films are single Cu_2O phase (cubic cuprite structure) and exhibit preferred growth orientation on ZnO with $(220)_{Cu_2O} \parallel (0002)_{ZnO}$. The grain size increases with deposition temperature. The lattice parameter of the Cu_2O film also increases with increasing temperature and exceeds the bulk equilibrium value by as much as 0.5 %. At low deposition temperature (300˚C) the film has rough surface morphology but as the deposition temperature is increased, the films become smooth with large grains. However, the film is stressed to maintain epitaxial and textured structure on ZnO. Larger grains result in higher carrier mobility and consequently resistivity decreases with increasing deposition temperature. The grain size and lattice parameter of the films deposited at the same temperature decrease with increasing film thickness indicating that the film stress relaxes with increasing film thickness. Stress relaxation and smaller grains with increasing film thickness are accompanied by rough surface morphology and lower carrier mobility.

4.3 Heteroepitaxy of Cu_2O thin film on ZnO

The fact that Cu_2O films deposited on ZnO are textured with $(220)_{Cu_2O} \parallel (0002)_{ZnO}$ (Figure 4.7 and 4.9) also raises the possibility that the Cu_2O growth on ZnO is epitaxial with $(220)_{Cu_2O} \parallel (0002)_{ZnO}$. Further experiments discussed below show that this is indeed the case (*vide infra*). This textured structure is different from previously reported results where Cu_2O films deposited by sputtering and electrochemical methods showed that

$(111)_{Cu_2O}$ || $(0002)_{ZnO}$.[11,17] It appears that MOCVD produces a different interface and epitaxy than these other deposition methods.

The epitaxy between Cu_2O and ZnO is surprising because Cu_2O and ZnO have cubic (a = 4.27 Å) and wurtzite (a = 3.25Å and c = 5.21Å) crystal structures, respectively with large lattice mismatch. However, epitaxy is still possible because these materials may form an energetically favorable periodic coincidence lattice at the interface between them. Figures 4.11 (a) and (b) show the atomic arrangements of the Cu atoms on the Cu_2O (220) plane and of the oxygen atoms on the ZnO (0002) plane, respectively. We can infer from the XRD data in Figure 4.7 and 4.9 that these planes are parallel to each other and to the glass substrate surface.

Copper atoms on the Cu_2O (220) plane and oxygen atoms on the ZnO (0002) plane form $\sqrt{2}\, a_{Cu_2O} \times a_{Cu_2O}$ (a_{Cu_2O} = 0.427 nm) and $\sqrt{3}\, a_{ZnO} \times a_{ZnO}$ (a_{ZnO} = 0.325 nm) rectangular unit cells, respectively. The longer sides of these unit cells, $\sqrt{2}\, a_{Cu_2O}$ and $\sqrt{3}\, a_{ZnO}$, have a lattice mismatch of 7.28 %. However, $(a_{Cu_2O}/a_{ZnO}) \approx (4/3)$ and epitaxy with $(001)_{Cu2O}$ || $(1\bar{2}10)_{ZnO}$ would produce a periodically coincident lattice with small coincidence lattice mismatch, F_o, of 1.46 % [$F_o = (4a_{ZnO} - 3a_{Cu_2O})/4a_{ZnO}$]. In cases where $a_{film}/a_{substrate} = m/n$ with m and n positive integers and m = n + 1 an edge dislocation is created to allow lattice matching[21] and this would be the case here. Thus, these atomic arrangements in the Cu_2O (220) and ZnO (0002) planes suggest an epitaxial relation where $(001)_{Cu_2O}$ || $(1\bar{2}10)_{ZnO}$. A proof of this hypothesis is shown in next.

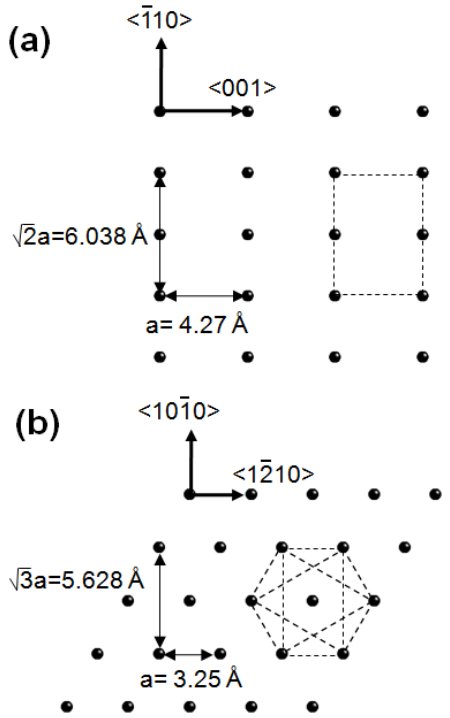

Figure 4.11. Atomic arrangements of (a) copper atoms on Cu_2O (220) plane and (b) oxygen atoms on ZnO (0002) plane.

To conclusively determine the epitaxial relationship between Cu_2O and ZnO, we prepared an epitaxial ZnO film on single crystalline sapphire (a-plane) by plasma enhanced MOCVD (PEMOCVD) from zinc acetylacetonate hydrate [$Zn(acac)_2$] and oxygen gases. The plasma deposition system was the same as that described in section 2.5. Plasma was generated over the substrate by applying radio frequency (rf) power to the ring electrode. $Zn(acac)_2$ was heated up to 100˚C in a copper boat and transported to the reactor by 200 sccm of Ar as carrier gas and 300 sccm of oxygen gas was delivered through a separate inlet. The substrate was heated up to 600˚C and pressure was kept at 3.6 Torr. The plasma was maintained during deposition by applying 20 W of rf-power to the ring electrode. Zinc oxide films grow on a-plane sapphire with c-axis perpendicular to

the substrate and with in-plane rotational alignment due to $[0001]_{ZnO} \parallel [11\bar{2}0]_{sapphire}$ and $[11\bar{2}0]_{ZnO} \parallel [0001]_{sapphire}$ epitaxy.[22] In this way, we could grow polycrystalline epitaxial ZnO thin films where the six-fold rotational symmetry of the ZnO crystals around their c-axis is retained across large areas.

To test the hypothesis for the epitaxial relation $(001)_{Cu_2O} \parallel (1\bar{2}10)_{ZnO}$, a cuprous oxide film was deposited on this aligned ZnO / Al_2O_3 substrate. Figure 4.12 shows the XRD pattern of Cu_2O/ZnO heteroepitaxial films grown on Al_2O_3 substrate and establishes that Cu_2O, ZnO and Al_2O_3 are aligned such that $(220)_{Cu_2O} \parallel (0002)_{ZnO} \parallel (11\bar{2}0)_{Al_2O_3}$; only the XRD peaks due to these planes are observed. This alignment is expected from the results presented so far and those in reference 22.

In-plane alignment in Cu_2O/ZnO heteroepitaxial films grown on Al_2O_3 was investigated by conducting ϕ-scans of the Cu_2O (200) and ZnO $(10\bar{1}1)$ diffractions. These diffractions are chosen for ϕ-scans because the zone axis of (220) and (200) planes in Cu_2O is ⟨001⟩ [Figure 4.13 (a)] and the zone axis of (0002) and $(10\bar{1}1)$ planes in ZnO is $\langle 1\bar{2}10 \rangle$ [Figure 4.13 (b)]. For these measurements, we set $(200)_{Cu_2O}$ perpendicular to the X-ray incident plane and fixed 2θ at 42.328˚ [$(200)_{Cu_2O}$ diffraction]. The substrate was then rotated to scan the angle ϕ across 360˚ (ϕ-scan). On the same sample, we conduct a second ϕ-scan where we set $(10\bar{1}1)_{ZnO}$ perpendicular to the X-ray incident plane and fixed 2θ at 36.29˚ [$(10\bar{1}1)_{ZnO}$ diffraction].

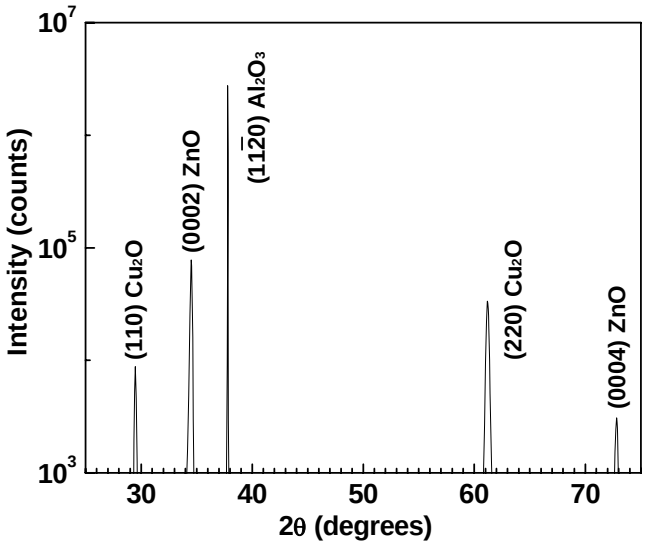

Figure 4.12. XRD from a Cu_2O film deposited by MOCVD on ZnO which itself was deposited on a-plane sapphire substrate by PEMOCVD. Cu_2O film was deposited at 400˚C and 2 Torr. ZnO film was deposited at 600˚C and 3.6 Torr.

These ϕ-scans [Figure 4.13 (c) and 4.13 (d)] show six peaks at identical angles for $(200)_{Cu_2O}$ and $(10\bar{1}1)_{ZnO}$ diffractions and conclusively show that $(001)_{Cu_2O} \parallel (1\bar{2}10)_{ZnO}$. Combining this result with those from 2θ scan, leads to the conclusion that, indeed, Cu_2O films grow on ZnO films epitaxially with $(220)_{Cu_2O} \parallel (0002)_{ZnO}; (001)_{Cu_2O} \parallel (1\bar{2}10)_{ZnO}$. Hence the hypothesis of the heteroepitaxy between Cu_2O and ZnO based on the atomic structure of the Cu_2O (220) surface and ZnO (0002) surface is proven to be true. The sharpness of the peaks and lack of other peaks in Figures 4.13 (c) and 4.13 (d) indicates nearly perfect alignment.

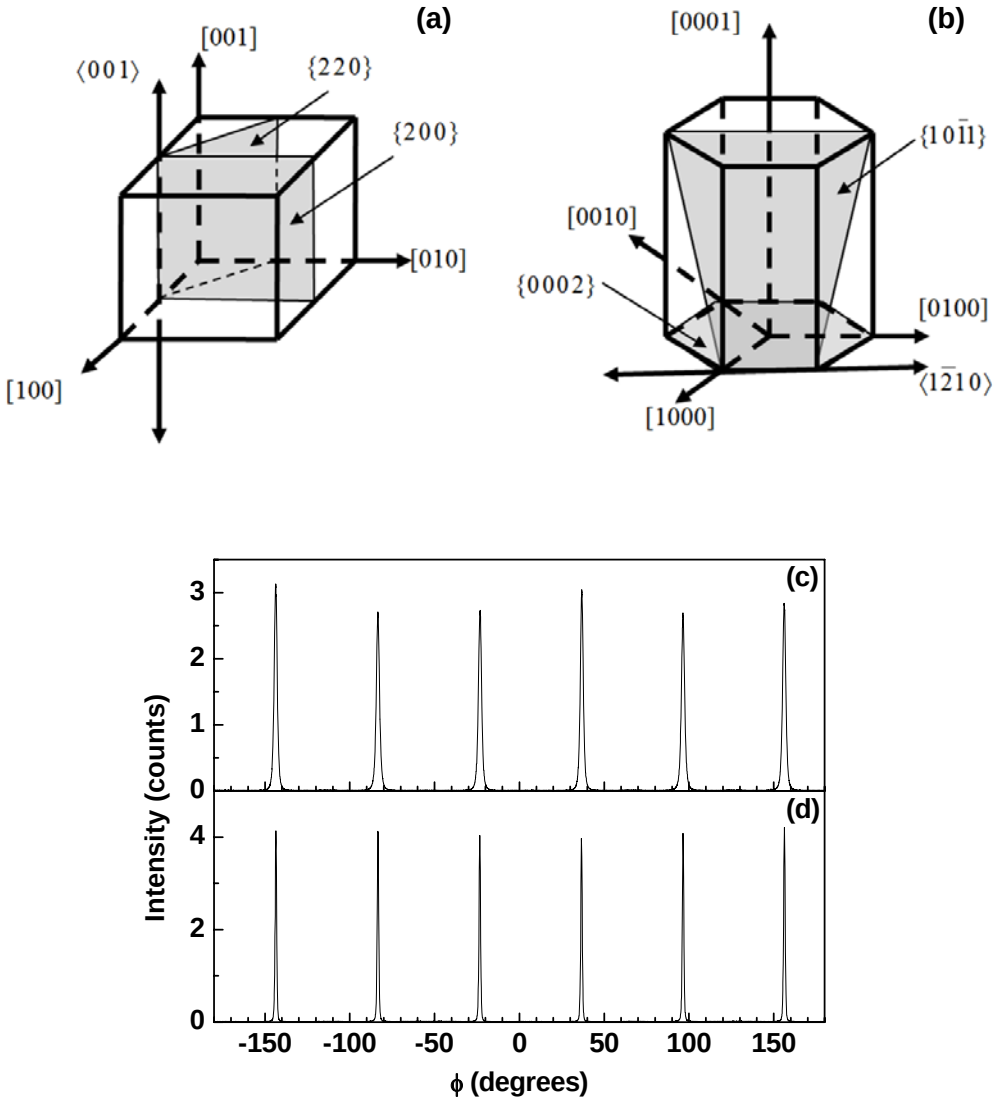

Figure 4.13. (a) Cubic Cu_2O and (b) hexagonal ZnO unit cells illustrating that the zone axis of the Cu_2O (220) and (200) planes is the ⟨001⟩ direction and that the zone axis of ZnO (0002) and (10$\bar{1}$1) planes is the ⟨1$\bar{2}$10⟩ direction. XRD ϕ-scan measurements (c) with 2θ fixed at 42.328˚ [Cu_2O (200) diffraction] and (d) at 36.29˚ [ZnO (10$\bar{1}$1) diffraction].

The six-fold rotational symmetry of the ZnO around the c-axis had been established before and is expected.[22] However, at first glance, six-fold rotational symmetry in ϕ-scan from cubic Cu_2O may seem surprising. The six peaks in the ϕ-scan from Cu_2O can be explained by considering the symmetry of the underlying ZnO and the possible ways in which $(220)_{Cu_2O} \parallel (0002)_{ZnO}$; $(001)_{Cu_2O} \parallel (1\bar{2}10)_{ZnO}$ epitaxy can be realized on polycrystalline ZnO films. Given a ZnO grain with in-plane allignment with respect to the sapphire substrate, the Cu_2O crystals can grow on this grain by alligning the rectangular unit cell shown in Figure 4.11(a) on the ZnO (0002) plane in three different directions separated rotationally by 60˚. These alignments are illustrated in Figure 4.11(b). Since the ZnO film is polycrystalline and a large number of grains are sampled during diffraction, all the possible orientations shown in Figure 4.11(b) are equally likely and give rise to the six peaks in the ϕ-scan.

References

[1] L. T. Drapak, Semiconductors **2**, 624 (1968).

[2] S. J. Pearton, W. H. Heo, M. Ivill, D. P. Norton, T. Steiner, Semicond. Sci. Tech. **19**, R59-R74 (2004).

[3] J. Ramirez-Ortiz, T. Ogurab, J. Medina-Valtierra, S. E. Acosta-Ortiz, P. Bosch, J. A. de los Reyes, V. H. Lara, Appl. Surf. Sci. **174**, 177-184 (2001).

[4] J. Herion, E. A. Niekisch, G. Scharl, Sol. Energ. Mater. **4**, 101 (1980).

[5] L. Papadimitriou, N. A. Economou, D. Trivich, Sol. Cells **3**, 73 (1981).

[6] L.C. Olsen, F. W. Addis, W. Miller, Sol. Cells **7**, 247 (1982-1983).

[7] A. E. Rakhshani, Solid State Electron. **29**, 7 (1986).

[8] C. A. Dimitriadis, L. Papadimitriou, N. A. Economou, J. Mater. Sci. Lett. **2**, 691 (1983).

[9] B. P. Rai, Sol. Cells **25**, 265 (1988).

[10] S. Ishizuka, S. Kato, Y. Okamoto, K. Akimoto, J. Cryst. Growth **237**, 616 (2002).

[11] M. Izaki, T. Shinagawa, K. Mizuno, Y. Ida, M. Inaba, A. Tasaka, J. Phys. D Appl. Phys. **40** 3326 (2007).

[12] A. Mittiga, E. Salza, F. Sarto, M. Tucci, R. Vasanthi, Appl. Phys. Lett. **88**, 163502 (2006).

[13] T. Minami, T. Miyata, K. Ihara, Y. Minamino, S. Tsukata, Thin Solid Films **494**, 47 (2006).

[14] S.S. Jeong, A. Mittiga, E. Salza, a. Masci, S. Passerni, Electrochim. Acta. **53**, 2226 (2008).

[15] H. Raebiger, S. Lany, A. Zunger, Phys. Rev. B **76**, 045209 (2007).

[16] H. Tanaka, T. Shimakawa, T. Miyata, H. Sato, T. Minami, Thin Solid Films **469-470**, 80 (2004).

[17] K. Akimoto, S. Ishizuka, M. Yanagita, Y. Nawa, G. K. Paul, T. Sakurai, Sol. Energy **80**, 715 (2006).

[18] S. Ishizuka, K. Suzuki, Y. Okamoto, M. Yanagita, T. Sakurai, K. Akimoto, N. Fujiwara, H. Kobayashi, K. Matsubara, S. Niki, Phys. Status Solidi C **1**, 1067 (2004).

[19] W. Shockley, H. J. Queisser, J. Appl. Phys. **32**, 510 (1961).

[20] G. G. condorelli, G. Malandrino, I. Fragala, Chem. Mater. **6** 1861 (1994).

[21] A. Trampert, K. H. Ploog, Cryst. Res. Technol. **35,** 793 (2000).

[22] J. B. Baxter, E. S. Aydil, J. Cryst. Growth **274**, 407 (2005).

Chapter 5

Cu_2O/ZnO heterojunction and photovoltaic application

5.1. Overview

In this chapter, current-voltage (*J-V*) characteristics of Cu_2O/ZnO heterojunction thin film solar cells are described. Carrier transport and recombination mechanism were investigated through the analysis of their current-voltage (*J-V*) characteristics in the dark and under various illumination intensities as a function of temperature between 100 K and 300 K. The temperature dependence of diode ideality factor, short circuit current and open circuit voltage within analytic models of this heterojunction was discussed and activation energy barriers for current flow were extracted. The Cu_2O/ZnO heterojunction solar cells were prepared by metal organic chemical vapor deposition (MOCVD) of Cu_2O thin films on ZnO sputtered on transparent conducting oxide (TCO) coated glass substrates. Activation energies extracted from temperature dependence of the saturation current reveals that interface recombination is the dominant carrier transport mechanism in these solar cells. Moreover, tunneling across an interfacial barrier plays an important role in current flow and TiO_2 buffer layer reduces tunneling. A high open circuit voltage at low temperature (~ 0.9 V at around 100 K) indicates that Cu_2O/ZnO heterojunction

solar cells have high potential as solar cells if the recombination and tunneling at the interface can be suppressed at room temperature.

5.2 Cu_2O/ZnO heterojunction solar cell fabrication

Cu_2O/ZnO heterojunction thin film solar cells were prepared on tin doped indium oxide (ITO) coated glass substrates by successive deposition of Al-doped ZnO (AZO) and undoped ZnO by magnetron sputtering followed by metal organic chemical vapor deposition (MOCVD) of Cu_2O. Radio frequency (RF) magnetron sputtering of ZnO and Al-doped ZnO was conducted at room temperature from undoped- and Al-doped-ZnO targets, respectively. An argon plasma maintained with 200 W of rf power at 5 mTorr was used for sputtering. The Al-doped ZnO layer thickness was kept constant at 200 nm but the effect of undoped ZnO thickness was examined by varying it between 65 nm and 200 nm. In one of the solar cells, 10 nm thick TiO_2 layer was deposited between the Cu_2O and a 65 nm thick ZnO film to examine the effect of a potential passivating buffer layer on the charge transport mechanism across the junction. This TiO_2 layer was deposited from Titanium(IV) isopropoxide ($Ti[OCH(CH_3)_2]_4$) and water vapor using atomic layer deposition (ALD) at a temperature of 180˚C (Cambridge NanoTech Inc., Savannah). The deposition rate was 1.9 Å/cycle.

Cuprous oxide (Cu_2O) films were deposited on these glass substrates, now coated with a stack of ZnO/AZO/ITO or TiO_2/ZnO/AZO/ITO, using MOCVD and Copper(II) hexafluoroacetylacetonate ($Cu(hfac)_2$) as the organometallic precursor. These film stacks are shown schematically with a real sample picture in Figure 5.1. The detail of the Cu_2O

MOCVD process was described in chapter 4. Briefly, solid $Cu(hfac)_2$ powder was placed in an enclosed copper boat heated to 65 ˚C. The $Cu(hfac)_2$ vapor was delivered into the deposition chamber by flowing argon through the boat as a carrier gas. The substrate was placed on a platen, which was maintained at 350 ˚C. Both water vapor and O_2 gas were used as oxidants.

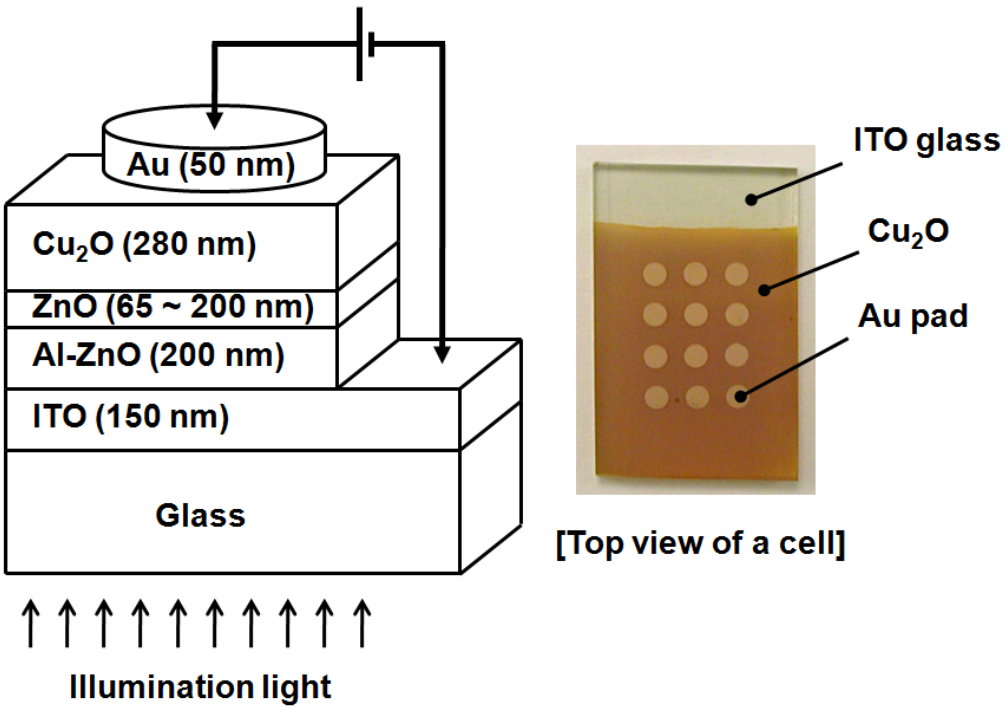

Figure 5.1. Schematic of Cu_2O/ZnO solar cell structure and a real sample picture. For the measurement of *J-V* characteristics, positive bias was applied to the Au pad in the forward bias case.

After the Cu_2O thin film deposition, gold pads were deposited by thermal evaporation for Cu_2O-side metal contacts therefore, the two electrodes for cells are ITO and Au. During the Au evaporation, metal mask with 2 mm diameter holes was used to define the shape and size of metal pads and this hole's size is the cell size. Morphology and thickness of the deposited films were examined using scanning electron microscopy (SEM). Typical thickness of the Cu_2O film in the solar cells discussed herein is 280 nm. A list of four representative solar cells that will be discussed and compared in this chapter is given in Table 5.1.

5.3 Solar cell characterization

5.3.1 Characterization background

The performance of solar cells which convert incident photon energy to electrical energy can be quantitatively analyzed by measuring the current-voltage (*J-V*) characteristics under illumination. The *J-V* characteristics of p-n junction type solar cells can be described by equivalent electrical circuit model shown in Figure 5.2. In the simplest case with infinite shunt resistance and zero series resistance, the *J-V* characteristics of the solar cell without illumination follow diode curve. If the diode is ideal and diffusion is the dominant carrier transport mechanism at the junction interface, its *J-V* characteristics can be described by the Shockley diode equation,

$$J = J_o\left[\exp\left(\frac{qV}{kT}\right)-1\right] \tag{5.1}$$

where, q is the electronic charge, kT is the thermal energy and J_o is the reverse saturation current, respectively. When the solar cell is illuminated, electron-hole pairs are generated and a photo current flows in the opposite direction of current flow under bias. This photo generated current shifts the dark J-V characteristics in the negative direction along the current axis by the amount of the photo current as shown in Figure 5.3. The point where the J-V characteristic crosses the x-axis (voltage axis) is called the open-circuit voltage (V_{oc}). This is the voltage of which the current in the external circuit is zero. The point where J-V curve crosses the y-axis (current-density axis) is called the short-circuit current (J_{sc}) which corresponds to the current when voltage is zero. An ideal solar cell will do work on an external load at a rate equal to the maximum power given by the product $|J_{sc} \times V_{oc}|$ but a real solar cell does work less than this amount. The real maximum power (P_{max}) will be the value which makes the product $|J \times V|$ maximum in the range between 0 and V_{oc} volts (and current density between 0 and J_{sc}). The ratio of P_{max} to $|J_{sc} \times V_{oc}|$ is called the fill factor (FF) of a solar cell.

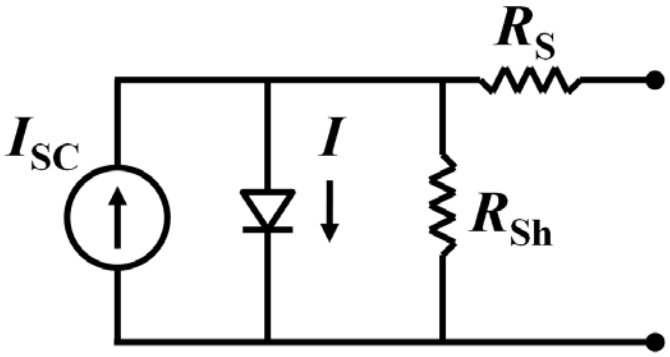

Figure 5.2. Schematic of a solar cell equivalent circuit.

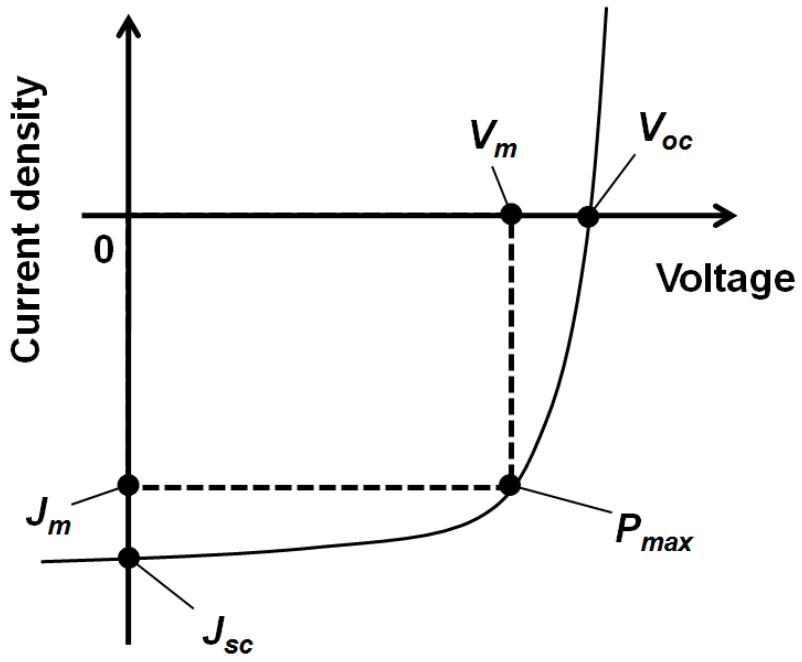

Figure 5.3. Illustration of a virtual *J-V* characteristic for a solar cell under illumination. V_m and J_m are the maximum voltage and maximum current density, respectively. Maximum power (P_{max}) is produced in the ranage $0 < V < V_{oc}$ and $0 < J < J_{sc}$. Fill factor is the ratio of $|J_m \times V_m|$ to $|J_{sc} \times V_{oc}|$.

The power conversion efficiency of a solar cell is given by

$$\eta = \frac{P_{\max}}{P_i} = \frac{FF \times J_{sc} \times V_{oc}}{P_i} \tag{5.2}$$

where, P_i is the illumination power density.

To investigate the dependence of conversion efficiency of solar cell on the incident light wavelength, incident-photon-to-current-conversion-efficiency (IPCE) is used. The IPCE, which is also referred to as the external-quantum-efficiency (EQE) is given by

$$\text{IPCE} = \frac{\text{electrons}/\text{sec}}{\text{photons}/\text{sec}} = \frac{\text{current}/(\text{charge of 1 electron})}{(\text{total power of photons})/(\text{energy of 1 photon})}$$

$$= \frac{I/e}{P_i(\lambda)/h\nu} = \frac{hcI}{e\lambda P_i(\lambda)} \tag{5.3}$$

$$= \text{IQE} \times \text{LHE}$$

where, *e* is the electronic charge, *h* is the Planck's constant, c is the speed of light, λ is the wavelength and ν is the frequency of the incident light. Therefore, IPCE can be determined from the measurements of incident power and photo generated current as a function of incident light wavelength. The IPCE can also be expressed as a product of internal-quantum-efficiency (IQE) and light-harvesting-efficiency (LHE). IQE is the measure of the generated carrier transport efficiency to the external load. LHE is expressed as

$$\text{LHE} = 1 - 10^{-A} \tag{5.4}$$

where, A is the optical absorbance of the solar cell.

5.3.2 Characterization equipment

The solar cells' *J-V* data were collected and recorded using a semiconductor parameter analyzer (Agilent Technologies, 4155C). For the temperature dependent *J-V* characteristics, the data were collected as a function of temperature between 100 K and 300 K in the dark and under illumination in a cryogenic microprobe station (Janis Research Company ST-500) with optical access through its bottom flange and through

the sample platen (Figure 5.4). A Xe-arc lamp in conjunction with a 0.125 m monochromator was used to illuminate the solar cells. The monochromator is equipped with both a 600 groove/mm grating and a mirror mounted on the same turret. For this work, the mirror was selected to illuminate the solar cells with the broadband AM1.5 spectrum (100 mW/cm^2). The AM1.5 spectrum was generated using commercially available filters (Newport Corp.) between the Xe-arc lamp and the monochromator. The output from the monochromator was directed and imaged onto the plane of the sample platen using mirrors and quartz lenses. The irradiance, $P_i(\lambda)$, was recorded at the plane of the sample platen, where the solar cell is placed, using a calibrated radiometry system that included a Thermopile sensing probe and a radiant power meter from Newport (70268 and 70260). The incident power was adjusted in the range from 2 to 200 mW/cm^2 using neutral density filters. The temperature of the cryogenic platen was measured at two locations and controlled using a combination of continuous liquid nitrogen flow and a heater. However, this temperature is not necessarily the same as the solar cell temperature due to heat transfer resistance between the solar cell and the cryogenic platen. Such high heat transfer resistance between the substrate and cooled platen is common under vacuum. To measure the solar cell temperature, an additional calibrated temperature sensor (Omega Engineering Inc., Resistance temperature detector) was used. It was attached directly on the surface of a second solar cell placed next to the solar cell being tested. The two solar cells were clamped in the same way to the cryogenic chuck so that monitoring the temperature of the second solar cell gives an accurate measure of the temperature of the solar cell being studied. All reported temperatures are those measured by this temperature sensor.

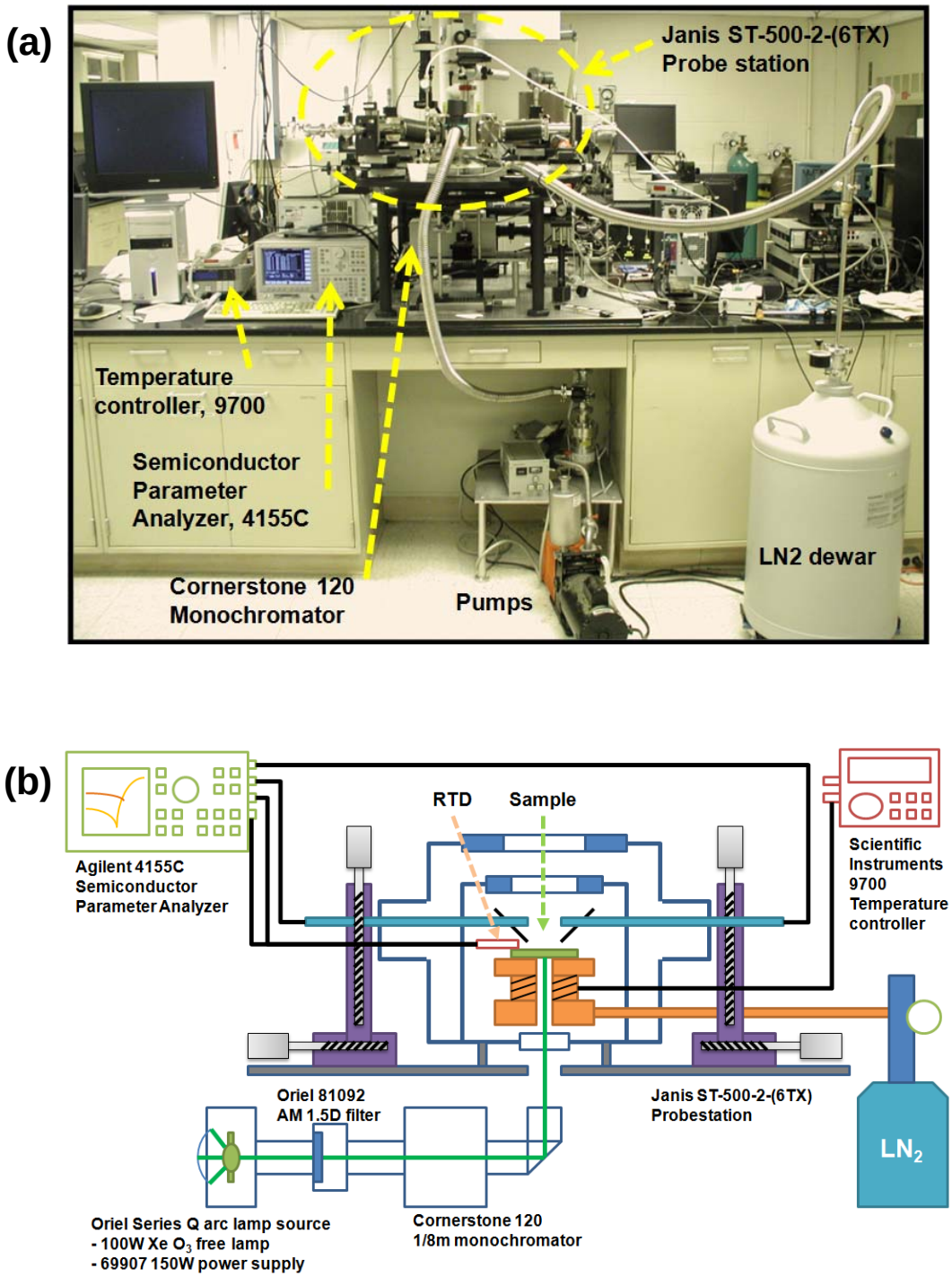

Figure 5.4. Equipment for measuring the temperature dependent *J-V* characteristics of solar cells. (a) is the photograph of the overall system. (b) is the schematic of the measurement set up.

5.4 Photovoltaic characterization for Cu_2O/ZnO solar cells

The photovoltaic characteristics of four different solar cells which have the structure of Au/Cu_2O/(TiO_2)/ZnO/Al-ZnO/ITO/Glass with different ZnO thicknesses (65 nm, 130 nm, 200 nm and 65 nm with 10 nm TiO_2 buffer layer) were investigated in the dark and under illumination at room temperature. The solar cells without undoped ZnO layer do not show electrical rectifying characteristics and the fact that sputtered ZnO layer at room temperature has high resistivity (> 10^7 Ω-cm, chapter 3) suggests that the thickness of ZnO has an important role in photovoltaic characteristics. One of the solar cells has TiO_2 layer between Cu_2O and ZnO to investigate buffer layer passivation.

The *J-V* curves for two solar cells with 65 nm and 130 nm thick ZnO in the dark and under illumination are shown in Figure 5.5. Other solar cells showed similar *J-V* characteristics. The figures of merit (V_{oc}, J_{sc}, FF, efficiency) for these solar cells are listed in Table 5.1. Several conclusions can be drawn from these *J-V* characteristics. First, the *J-V* characteristics under illumination show that these cells have small V_{oc} (0.19 ~ 0.34 V) and J_{sc} (0.64 ~ 0.74 mA/cm^2) and as a result, power conversion efficiencies are poor (below 0.1%). Second, the *J-V* characteristics of thin ZnO (65 nm) solar cells seem to follow the exponential diode curve (diode ideality factor is 2.7) but those of the thick ZnO solar cells (above 130 nm) seem to be limited by series resistance and currents do not rise exponentially as would be expected from a diode (diode ideality factor is above 7). Third, the curves in the dark and under illumination cross over each other in the forward bias region and this characteristic is most prominent in solar cells thicker ZnO films.

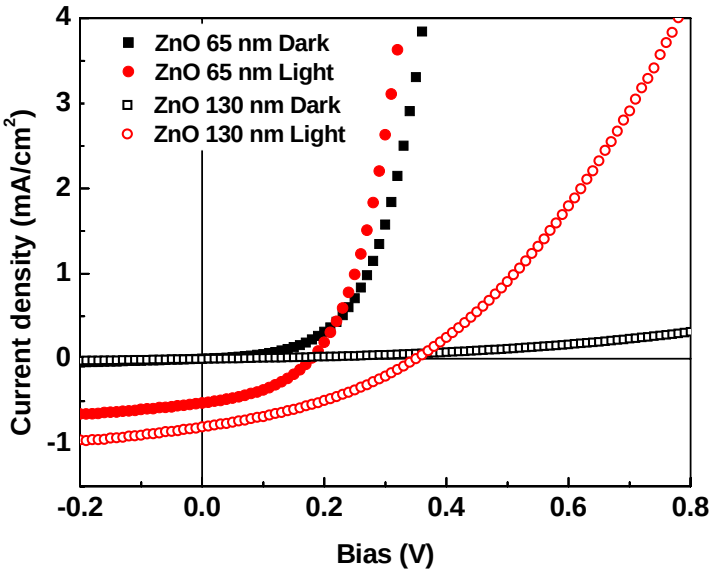

Figure 5.5. *J-V* characteristics of two Cu_2O/ZnO heterojunction solar cells. The cell structures are Au/Cu_2O/ZnO/Al-ZnO/ITO/Glass with 65 nm thick ZnO and 130 nm thick ZnO. The "Dark" and "Light" *J-V* characteristics were measured in the dark and the under illumination, respectively.

Table 5.1. The figures of merit for Cu_2O/ZnO heterojunction solar cells. The structure of solar cells is Au/Cu_2O/(TiO_2)/ZnO/Al-ZnO/ITO/Glass with different ZnO thicknesses (65 nm, 130 nm, 200 nm). A fourth cell had a 10 nm thick TiO_2 buffer layer between the Cu_2O and ZnO layers.

Solar Cell made with	V_{oc} (V)	J_{sc} (mA/cm^2)	FF	Efficiency (%)	Diode ideality factor (dark)
65 nm thick ZnO	0.19	0.64	0.39	0.05	2.7
130 nm thick ZnO	0.34	0.74	0.41	0.09	7.2
200 nm thick ZnO	0.34	0.71	0.34	0.08	7.4
65 nm thick ZnO + 10 nm thick TiO_2 buffer	0.24	0.66	0.39	0.06	2.7

The non ideal diode characteristics of thick ZnO cells may be due to the high resistivity of ZnO films and this will be discussed more in detail in the next section (temperature dependent *J-V* analysis). The crossing of the dark and light *J-V* characteristics has been reported in Cu(In,Ga)Se_2 (CIGS) thin film solar cells.[1,2,3] Although the underlying reasons are not clear, one of the suggested mechanisms is that the photo-generated carriers alter the electric field distribution and change carrier conduction during illumination.[4,5,6] It seems that illumination increases the conductivity of Cu_2O and ZnO and reduces the series resistance of the solar cells. This causes the cross-over.

To investigate the dependence of solar cell efficiency on incident light wavelength, IPCE was measured in the wavelength range between 350 nm and 700 nm for the solar cell with 130 nm thick ZnO and the results are shown in Figure 5.6. For the IPCE measurement, the monochromator grating was selected and scanned to control the wavelength of illumination light and the slit located at the exit of monochromator was adjusted to make ~ 10 nm bandpass. The IPCE exhibits a maximum of ~ 40 % around 400 nm and abruptly decreases as wavelength increases. The IQE shows the same trend as IPCE and this low IQE seems to limit the solar cell performance. The low IQE means that the photo-generated carriers do not contribute to short circuit current efficiently and the generated carriers may recombine before transport to the external load. Therefore, it is needed to investigate the carrier transport mechanism in this Cu_2O/ZnO heterojunction solar cell.

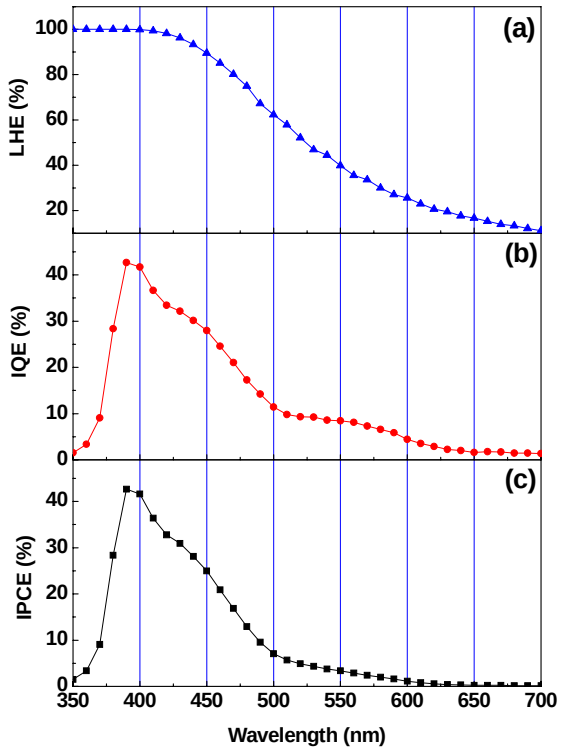

Figure 5.6. The spectrum of (a) LHE, (b) IQE and (c) IPCE of Cu_2O/ZnO solar cell with 130 nm thick ZnO.

5.5 Temperature dependent *J-V* characterization for Cu_2O/ZnO solar cells

5.5.1 Background on the theory of temperature dependent solar cell *J-V* characteristics

The current-voltage (*J-V*) characteristics of a p-n junction solar cell can be interpreted within the equivalent circuit (Figure 5.2) and in the ideal case, its *J-V*

characteristics can be described by the Shockley diode equation (Equation 5.1). In the Shockley diode model the reverse saturation current, J_o, flows by thermal generation of minority carriers followed by diffusion to the junction and, thus, depends on the band gap (E_g) of the semiconductor that forms the junction. For the Shockley model the J_o is given by

$$J_o = \frac{qD_p n_i^2}{L_p N_D} + \frac{qD_n n_i^2}{L_n N_A} = J_{oo} \exp\left(-\frac{E_g}{kT}\right) \tag{5.5}$$

where, N_D and N_A are the donor and acceptor concentrations on the n and p side of the junction, respectively, and D_j and L_i (j, i = n or p) are the diffusion coefficients and diffusion lengths of charge carrier j, respectively. In the last term of equation (5.5), the preexponential term, J_{oo}, is weakly temperature dependent compared with the exponential term. While Shockley's model provides an approximate framework, many of the assumptions in its derivation is often violated in real diodes. To take into account the nonidealities, diode ideality factor A is introduced and in the forward bias region, the J-V characteristics of p-n junction, equation (5.1), can be generalized as[7]

$$J = J_o \exp\left(\frac{qV}{AkT}\right) = J_{oo} \exp\left(-\frac{E_a}{AkT}\right) \exp\left(\frac{qV}{AkT}\right) \tag{5.6}$$

where, the activation energy, E_a, represents the barrier that must be overcome to generate charge carriers that contribute to the reverse saturation current and this value is equal to the band gap in ideal diodes. In equation 5.6, forward bias approximation was assumed, that is $\exp(qV/kT) >> 1$. The activation energy and diode ideality factor, E_a and A, provide insight into the phenomena occurring at the p-n junction such as tunneling and recombination. Typically, $1 \leq A \leq 2$ and A values larger than 2 indicate large series

resistances and/or the diode becoming less important in determining the *J-V* characteristics of the equivalent circuit in Figure 5.2.

The charge transport and recombination mechanism of solar cells under illumination can also be analyzed within the framework of this generalized model. The *J-V* characteristics of a solar cell under illumination is given by

$$J = J_{ol}\exp\left(\frac{qV}{A_l kT}\right) - J_{sc} = J_{ool}\exp\left(-\frac{E_a}{A_l kT}\right)\exp\left(\frac{qV}{A_l kT}\right) - J_{sc} \tag{5.7}$$

where, subscript "*l*" was inserted to distinguish the model parameters under illumination from those in the dark. The parameters under illumination may be different from those in the dark because photo-generated charge carriers may change the electric fields and conductivities of the semiconductors, which form the junction. In equation (5.7), J_{sc} is photo-generated short circuit current and a common relationship between short circuit current and the open circuit voltage (V_{oc}) follows the diode *J-V* characteristics by setting $J = 0$;[7,8]

$$V_{oc} = \frac{A_l kT}{q}\ln\left(\frac{J_{sc}}{J_{ol}}\right) + \frac{E_a}{q}. \tag{5.8}$$

Thus, if A_l is independent of temperature, a plot of V_{oc} versus T should be linear with intercept at T = 0 K equal to the activation energy divided by q, E_a/q. If there is no interfacial recombination and generation and if thermal generation of carriers across the band gap dominate the saturation current then E_a will be equal E_g; otherwise, E_a will be less than E_g. However, this method not only requires extrapolation of the data to 0 K but assumes that A_l is not a function of temperature. The diode ideality factor, A_l can be function of temperature, which introduces nonlinearities with temperature into equation

(5.8).[9] An alternative method relies on the determination of A_l and J_{ol} at each temperature by measuring J_{sc} as a function of V_{oc}.[7] Rearranging equation (5.7) and solving for ln J_{sc} in terms of V_{oc} yields

$$\ln J_{sc} = \frac{qV_{oc}}{A_l kT} + \ln J_{ol} \ . \tag{5.9}$$

Thus, assuming that A_l is a weak function of illumination intensity (equivalently, a weak function of J_{sc}) a plot of ln J_{sc} versus qV_{oc}/kT at each temperature should be linear with slope $1/A_l$ and intercept, ln J_{ol}. This information can be obtained at each temperature by collecting J-V characteristics at different illumination levels, thereby varying J_{sc}. Following, activation energy can be obtained from the temperature dependence of A_l and J_{ol}. Specifically, the relationship $J_{ol} = J_{ool} \exp(-E_a/A_l kT)$ is rearranged to give

$$A_l \ln J_{ol} = -\frac{E_a}{kT} + A_l \ln J_{ool}, \tag{5.10}$$

and E_a is calculated from the slope of the straight line which results when A_l ln J_{ol} is plotted versus $1/kT$.

While this analysis provides the activation energy E_a and the temperature dependence of the diode ideality factor, interpretation and insight into the physical origin of these values require higher level models and a quantitative picture of the energy band alignment and band bending at the junction. Conversely, such a picture can be hypothesized and its predictions compared to the measurements. This is done here after the discussion of the data analysis.

5.5.2. Analysis of *J-V* data for Cu_2O/ZnO solar cells

5.5.2.1. Space Charge Limited J-V characteristics in ZnO in the Dark

Figure 5.7 shows the dark *J-V* characteristics of two Cu_2O/ZnO solar cells made using a 65 nm thick ZnO film [Figure 5.7 (a)] and a 130 nm thick ZnO film [Figure 5.7 (b)] in the temperature range from 160 K to 295 K. The *J-V* characteristics of a third solar cell assembled using a 200 nm thick ZnO film was similar to that shown for the solar cell made with 130 nm thick ZnO [Figure 5.7 (b)]. If the *J-V* characteristics of these Cu_2O/ZnO solar cells follow Shockley's model, the semilog plots should show a linear region over several decades of current with slope q/AkT and $1 \leq A \leq 2$. However, as shown in Figure 5.7, only the solar cell made with a thin ZnO film (65 nm) shows a linear region across at least two decades of current [Figure 5.7 (a)]. Solar cells with thicker ZnO films [like Figure 5.7 (b)] have significant series resistance under dark and one cannot extract information about the diode ideality factor and saturation current activation energy from the *J-V* measurements.[10] The nonlinear semilog *J-V* characteristics and the small slope for solar cells with thick (> 65 nm) ZnO films [Figure 5.7 (b)] indicate that, in these cases, the charge carrier transport across the solar cell and the *J-V* characteristics is determined by carrier transport in the ZnO film rather than by the junction properties.

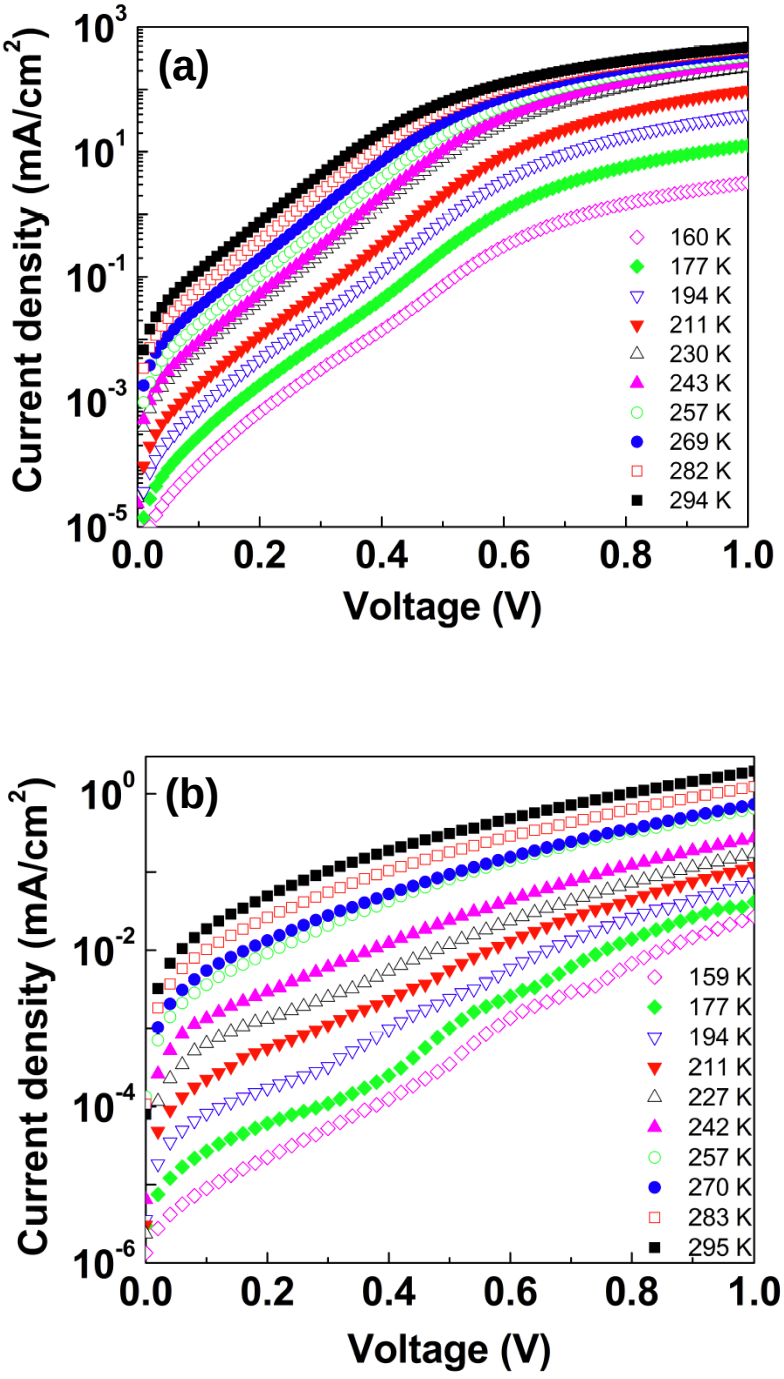

Figure 5.7. Dark *J-V* characteristics of Cu_2O/ZnO solar cells as a function of temperature between 160 K and 295 K. The thin film stack that comprised this solar cell was Au/Cu_2O/ZnO/AZO/ITO/Glass: (a) 65 nm thick ZnO (b) 130 nm thick ZnO.

An alternative analysis of the data in Figure 5.7 (b) is shown in Figure 5.8 (a) wherein the *J-V* characteristics is plotted on a log-log scale and fitted using a power law model rather than an exponential model. In the dark and in the low bias region (< 0.2 V), the *J-V* characteristics follow a power law, $J \sim V^m$, where m = 1 (Ohmic behavior). At higher bias (> 0.5 V) $m > 2$ and increases with decreasing temperature from ~ 5.5 at 295 K to 3 at 160 K. The power law dependence with high value of *m* and the temperature dependence of *m* are typical of space charge limited current (SCLC)[11] conduction mechanism. The fact that power law *J-V* characteristics is observed when the ZnO film thickness is increased suggests that the current is limited by the high resistivity (>10^7 Ω-cm) ZnO which behaves like an insulator with a trap distribution that decays exponentially into the forbidden band gap. Within the model developed by Rose,[11] $m \approx (T_c/T) + 1$ for $T_c > T$ where kT_c is the characteristic energy that describes how rapidly the trap density distribution decays into the forbidden gap below the conduction band edge. Figure 5.8 (b) shows a plot of *m* versus *1/T* and from the slope of the best fit line characteristic energy, kT_c is extracted as ~ 80 meV. The intercept, however, goes through - 0.24 instead of 1. Forcing the intercept to go through 1 and fitting the experimental data with this constraint gives kT_c = 56 meV. Either way, the conclusion is that traps distributed several *kT* below the conduction band exists. The density of these traps was estimated using the crossover method described by Kumar et al.[12] In this method, the space-charge-limited region of the temperature dependent *J-V* characteristics shown in Figure 5.8 (a) are fitted to a power law and the fits are extrapolated to higher voltages where they tend to intersect each other at a common potential called the crossover voltage, V_c. Such an analysis is shown in Figure 5.8 (c) for the data in Figure 5.8 (a).

Indeed the best fit lines to data between 159 and 242 K all intersect at V_c = ~ 3 V. The data for temperatures higher than 242 K intersect others at somewhat higher voltages but SCLC region for these temperatures are also less developed and the slope is lower. Based on a cross over voltage of ~ 3 V, a trap density of ~1.4×10^{17} cm^{-3} was estimated in ZnO films.

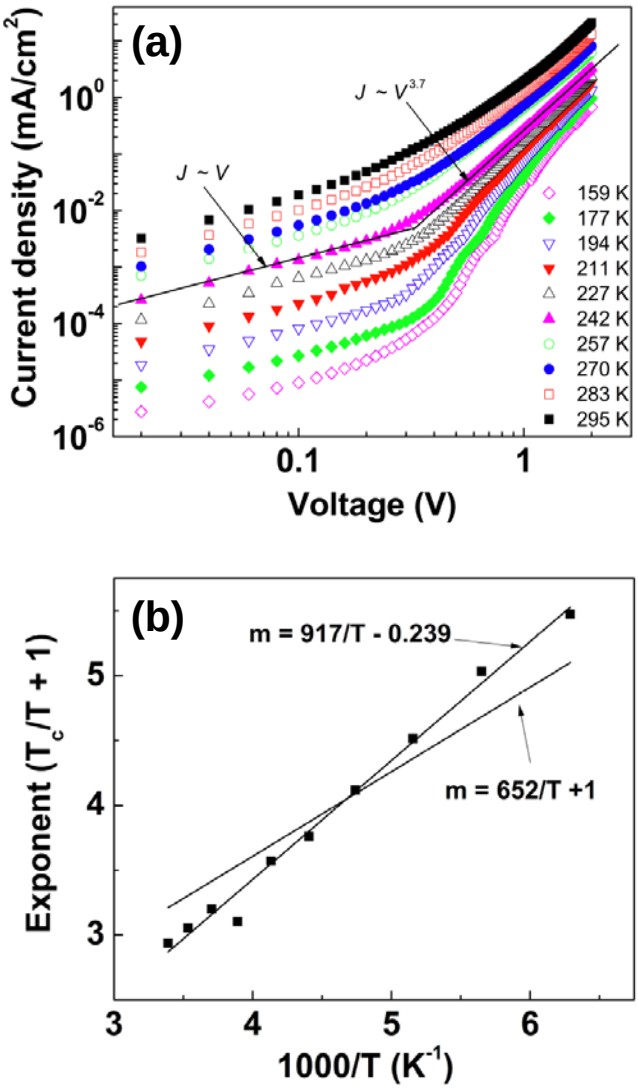

(Figure 5.8 (a) and (b) are shown above and (c) and (d) continued on next page)

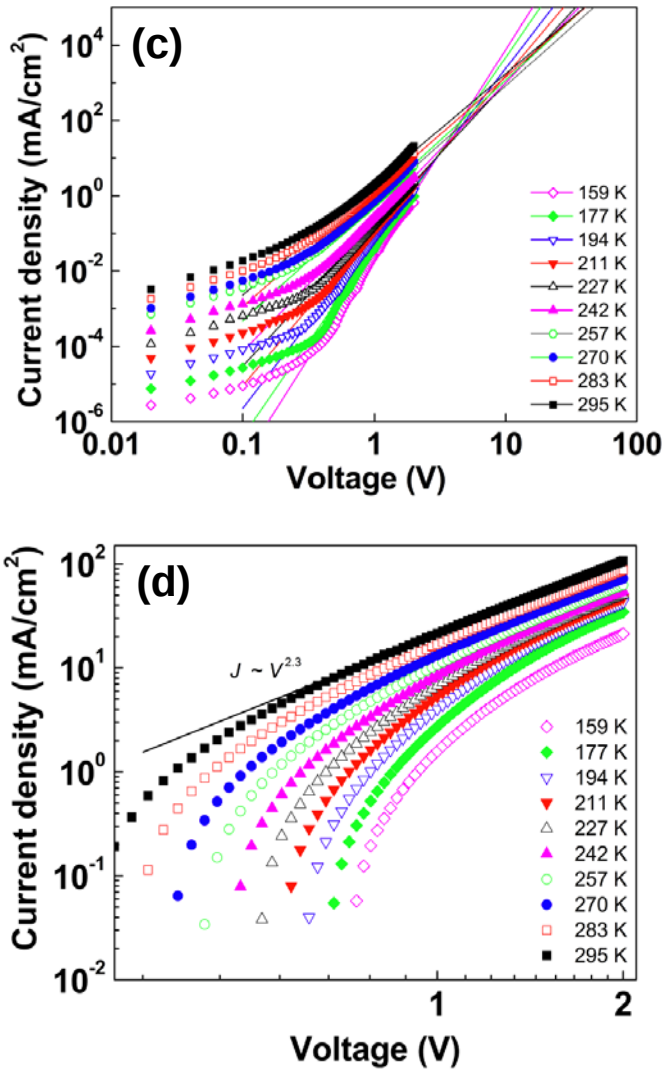

Figure 5.8. (a) Dark *J-V* characteristics (log - log scale) of a Cu_2O/ZnO solar cell with 130 nm thick ZnO as a function of temperature. The solid lines are power law fits to the data: fits for only one set of data is shown in (a). The behavior is ohmic at low bias values with $J \sim V$. The exponent, m, in the power law fits depends on the temperature at high bias values as shown in (b). (c) The "crossover" plot for the data in (a): all power law fits are shown as lines and intersect at the crossover voltage. (d) *J-V* characteristics (log - log scale) of the same solar cell in (a) but under illumination. The solid line is the power law fit to one set of data at 295 K. Fits for other sets are not shown for clarity but the exponent, m, in the power law fits is nearly independent of temperature in the high bias region.

Figure 5.8 (d) shows the *J-V* characteristics of the same solar cell discussed in Figures 5.7 (b) and 5.8 (a) on a log-log plot but under 100 mW/cm^2 AM 1.5 illumination. The *J-V* characteristic under illumination is very different from that measured in the dark. In particular the power law fit in the high bias region (> 1 V) yields a temperature independent exponent that is closer to 2 (m ~ 2.3), the value predicted by the SCLC theory without traps.[13] Although the exponent, m, is still slightly higher than 2, the *J-V* characteristic under illumination seems to be determined by trap-free SCLC theory because the photogenerated carriers fill the traps and the current flows as it would in a trap-free material.

5.5.2.2. *J-V* characteristics under illumination

Under illumination, the photoconductivites of both ZnO and Cu_2O are large enough that the balance between the diode and photogenerated current dominate the *J-V* characteristics at lower bias. Consequently, the diode nonideality factor A_l can be extracted from a plot of log J_{sc} versus V_{oc} [Equation (5.9)]. Figure 5.9 shows such a plot for the solar cell made with Cu_2O deposited on a 130 nm thick ZnO film (the solar cell discussed in Figure 5.8). To construct this plot, the short circuit current was varied by changing the illumination intensity at each temperature and extracted the diode ideality factor, A_l, from the slopes ln J_{sc} versus qV_{oc}/kT as a function of temperature. Indeed, a

plot of ln J_{sc} versus qV_{oc}/kT at each temperature for all solar cells investigated in this study were linear and resembled the typical plot shown in Figure 5.9.

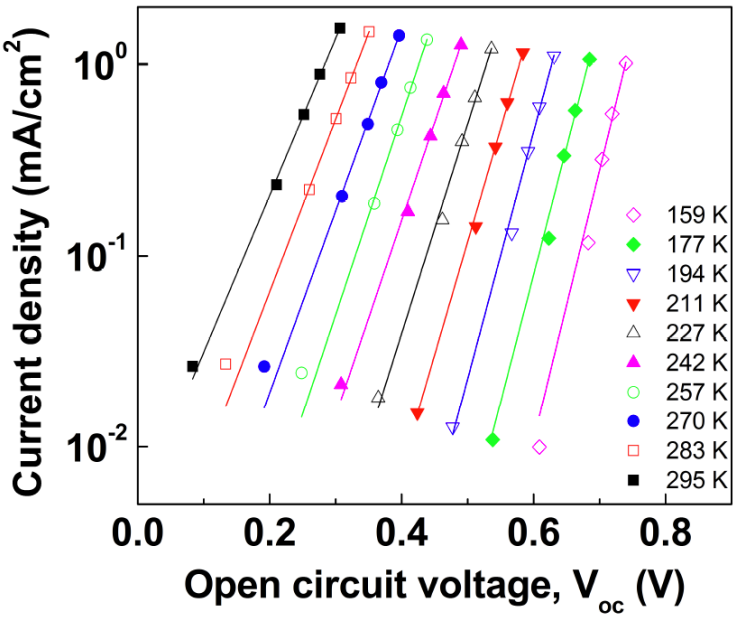

Figure 5.9. Semi-log plot of short circuit current (J_{sc}) versus open circuit voltage (V_{oc}) as a function of temperature and illumination intensity for a Cu_2O/ZnO heterojunction solar cell with 130 nm thick ZnO layer. Solid lines are fits to the data using equation (5.9) to extract A_l and J_{ol}.

Activation energies were extracted using both equation (5.8) and equation (5.10) and these two methods will be referred to as the "intercept" and the "slope" methods, respectively. In the intercept method, E_a is obtained from the $T = 0$ intercept of the V_{oc} versus T plot by extrapolation and such plots are shown for several Cu_2O/ZnO solar cells in Figure 5.10 (a). These data were collected while the solar cells were illuminated with 100 mW/cm^2 AM 1.5 radiation. Although all the data from different solar cells appears linear in the measured temperature range (100 K - 300 K), V_{oc} begin to deviate from linearity in the low temperature region and extrapolation to $T = 0$ K will introduce some error to the extracted activation energy. In the slope method, E_a is calculated from the slope of the line that results when $A_l \ln J_{ol}$ is plotted versus $1/T$. Such plots are shown in Figure 5.10 (b) for the same solar cells analyzed in Figure 5.10 (a). Indeed plots of $A_l \ln J_{ol}$ versus $1/kT$ are linear and the slopes of the lines in Figure 5.10 (b) allow the calculation of activation energies. The activation energies extracted by both methods are summarized in Table 5.2. When compared, the activation energies extracted using the intercept and slope methods are only slightly different from each other and agree to within 10% or better. However, the slope method is more reliable because of the uncertainty in extrapolation of V_{oc} to $T = 0$ K in the intercept method.

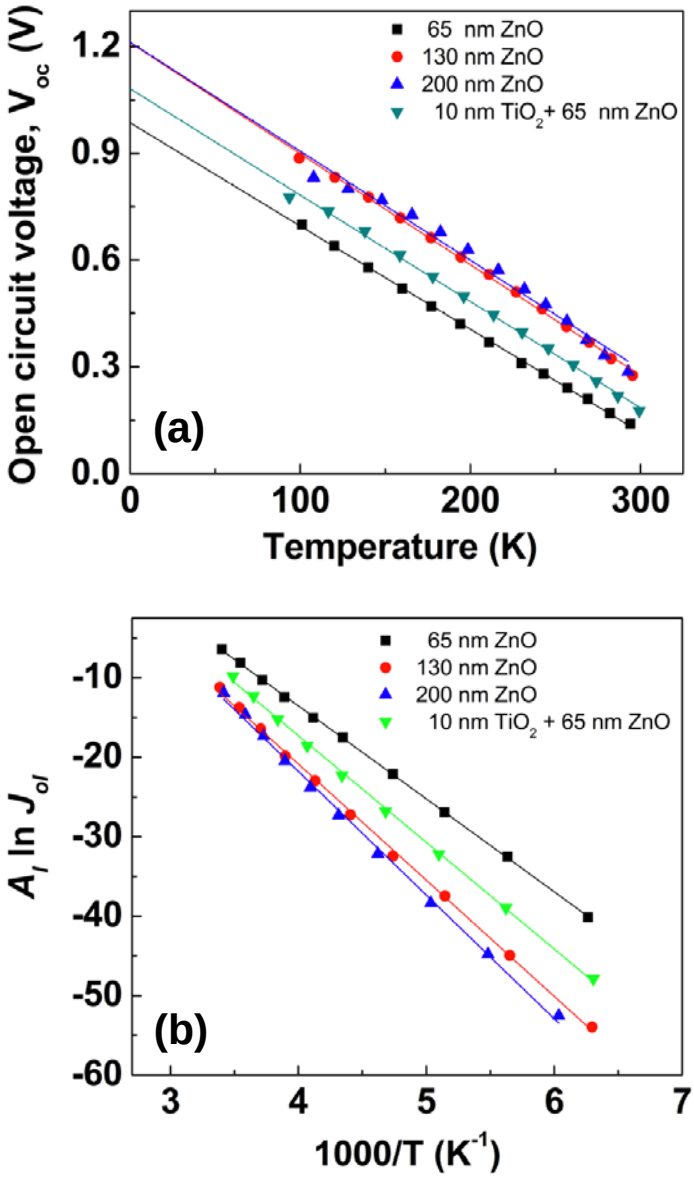

Figure 5.10. (a) Open circuit voltage (V_{oc}) as a function of temperature for solar cells listed in Table 5.2. The lines are linear fits to the data and show extrapolation of V_{oc} to T = 0 K to determine the activation energy in equation (5.8) from the T = 0 K intercept. (b) The plot of the $A_l \ln J_{ol}$ versus reciprocal temperature for the same solar cells as in (a). The lines are fits to the data using equation (5.10). The activation energy for each cell is determined from the slopes of these lines.

Table 5.2. Extracted saturation current activation energies for Cu_2O/ZnO solar cells. The structure of solar cells is Au/Cu_2O/(TiO_2)/ZnO/Al-ZnO/ITO/Glass with different ZnO thicknesses, 65 nm, 130 nm, 200 nm and TiO_2 10 nm + ZnO 65 nm. The last sample has TiO_2 buffer layer between Cu_2O and ZnO layers.

Solar Cell made with	E_a (eV) from intercept	E_a (eV) from slope
65 nm thick ZnO	0.99	1.01
130 nm thick ZnO	1.21	1.26
200 nm thick ZnO	1.21	1.34
65 nm thick ZnO + 10 nm thick TiO_2 buffer	1.08	1.16

5.5.3 Interpretation of the *J-V-T* analysis

Several significant conclusions about recombination and transport across the Cu_2O/ZnO heterojunction can be drawn from the analysis in the previous section. These conclusions are (1) current transport across the Cu_2O/ZnO junction is by recombination at interfacial electronic states and (2) tunneling also plays a role.

5.5.3.1 Interfacial recombination

First, the activation energies extracted from the analysis in Figure 5.10 range from 0.99 to 1.34 eV, much smaller than the band gap of the Cu_2O absorber layer (E_g = 2.17 eV). This unequivocally indicates that current transport across the Cu_2O/ZnO interface must involve charge recombination at interfacial electronic states in the forbidden band gap.[7,14] In this case, the measured activation energy gives clues about the Fermi levels

and band bending near the interface. Next, band bending at the Cu_2O/ZnO junction and an interpretation of the measured activation energy are discussed.

Since Cu_2O is the absorber material, a well-designed Cu_2O/ZnO heterojunction solar cell must be asymmetrically doped to place the wider depletion region in the Cu_2O layer. Indeed the electron concentrations in the ZnO film in our solar cells are higher (~ 10^{17} cm^{-3}) than hole concentrations in the Cu_2O layer (~ 10^{15} cm^{-3}) and form an asymmetrically doped p-n heterojunction. At such an interface, the concentration of electrons exceed that of holes and the recombination current is limited by the supply of holes from the Cu_2O side which must overcome the barrier established by band bending in the depletion region. The interface recombination current in this case is given by

$$J = qs_i p_i \exp\left(\frac{qV}{kT}\right) \tag{5.11}$$

where, s_i and p_i are the interface recombination velocity and the hole concentration at the interface, respectively. The hole concentration at the interface is due to holes that can overcome the barrier established due to band bending and is given by

$$p_i = N_v \exp\left(-\frac{q\phi_D}{kT}\right) \tag{5.12}$$

where N_v is the effective density of states in the valence band and $\phi_D = (E_F - E_v)/q$ is the so-called diffusion potential, the difference between the Fermi level and the valence band edge at the interface. Substitution of equation (5.12) into (5.11) yields

$$J = qs_i N_v \exp\left(-\frac{q\phi_D}{kT}\right)\exp\left(\frac{qV}{kT}\right). \tag{5.13}$$

Comparison of equations (5.7) and (5.13) with $A_l = 1$ would lead to the conclusion that the measured activation energy, E_a is the energy difference between Fermi level and the

valence band edge at the interface as shown in Figure 5.11. Indeed, assuming that the Cu_2O/ZnO junction is an ideal abrupt heterojunction at thermal equilibrium and using the known measured values of electron affinities, band gaps and carrier densities in ZnO and Cu_2O, E_a is estimated approximately ~ 1 - 1.1 eV as shown in Figure 5.11.[15,16,17] This value is approximately in the range of extracted activation energies. Thus, it is concluded that the interface recombination is the dominant current flow mechanism across the Cu_2O/ZnO heterojunction where the rate limiting step is diffusion of holes against the barrier established by band bending to recombine with electrons trapped in interfacial states. This mechanism is shown as path 1 in Figure 5.11.

5.5.3.2 Tunneling

A remaining issue is that, the diode ideality factor, A_I is not equal to one. A temperature dependent value of A_I indicates that tunneling may be involved in the interfacial recombination. One possible tunneling mechanism is depicted as path 2 in Figure 5.11 wherein a hole tunnels across the barrier due to band bending to recombine with a trapped electron. Another clue that tunneling is involved comes from the quantitative temperature dependence of the diode ideality factor. If the diode ideality factor is independent of temperature then the *J-V* characteristic is governed by diffusion and recombination either at the interface or in the depletion region of the junction. However, if the diode ideality factor depends on temperature then tunneling may be implicated. In particular, if the diode ideality factor is proportional to *1/T* then the argument of the exponent in equation (5.6) and the current become independent of

temperature indicating that tunneling plays a role in current flow. Thus, when tunneling is present a plot of A_l or A_d versus $1/T$ will be linear.

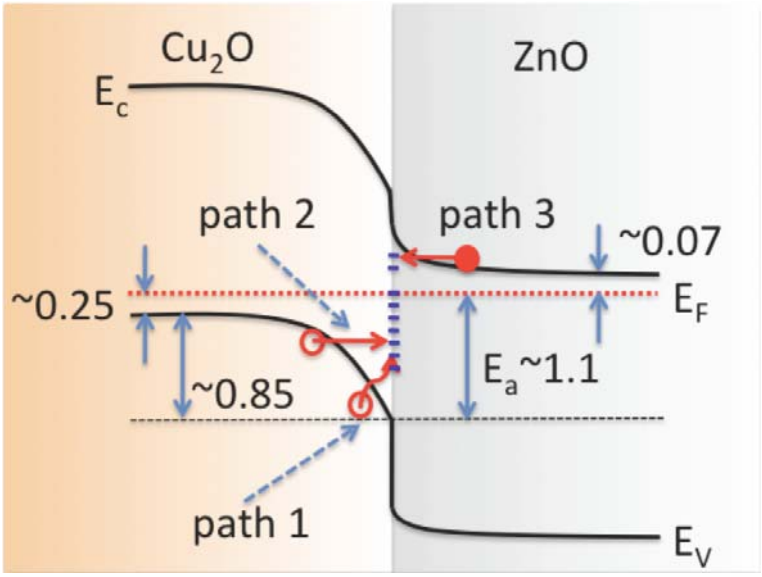

Figure 5.11. Band diagram of the Cu_2O/ZnO heterojunction. E_C, E_V, E_F, and E_a are the conduction-band-edge, valence-band-edge, Fermi-level, and activation energies, respectively. Most of the band bending is shown to be on the Cu_2O side because of lower doping in Cu2O compared to the ZnO side. Paths 1 and 2 indicate two possible hole recombination pathways through interface defects. Activation energy (E_a) is the barrier that the holes have to overcome to recombine. The approximate energy levels are based on the properties of bulk Cu_2O and ZnO. Electron affinities: 3.2 eV (Cu_2O)[15] and 4.2 eV[16] (ZnO); band gaps: 2.17 eV[17] (Cu_2O) and 3.44 eV[17] (ZnO); dielectric constants: 7.11[17] (Cu_2O) and 7.8[17] (ZnO), electron effective mass: $0.275m_o$[17] (ZnO) and hole effective mass in $0.58m_o$[17] (Cu_2O) - where m_o is free electron mass. Measured carrier concentrations of ~10^{15} cm^{-3} (Cu_2O) and ~2×10^{17} cm^{-3} (ZnO) were used.

Figure 5.12 (a) shows the temperature dependence of the dark current diode ideality factors for solar cells made with 65 nm thick ZnO film with and without a TiO_2 buffer layer. The diode ideality factor shows a clear linear dependence on *1/T* for the solar cell that was made without the TiO_2 film. When a thin TiO_2 buffer layer is used the diode ideality factor in the dark becomes independent of temperature at high temperatures (low *1/T*) but is still linear with *1/T* at low temperatures. This indicates that recombination via tunneling is reduced in presence of the buffer layer so that, at high temperature, activated surface recombination becomes dominant. As temperature is lowered, the activated recombination process slows down and tunneling becomes important again. The two processes, recombination via tunneling and activated recombination, can occur together and exist in parallel across the junction region.

A quantitative analytical model that attempts to describe tunneling at a junction was introduced by Padovani and Stratton[18] who were studying tunneling across a Schottky barrier. Within this model, the diode ideality factor can be described by

$$A = \frac{E_{oo}}{kT} \coth\left(\frac{E_{oo}}{kT}\right) \tag{5.14}$$

where, E_{oo} is a characteristic tunneling energy which depends on the doping concentration in the semiconductor comprising a Schottky diode, $E_{oo}=(e\hbar/2)(N_A/m^*\varepsilon)^{1/2}$.

E_{oo} is related to the tunneling probability. Thermionic field emission (tunneling) is dominant when $E_{oo} \sim kT/q$ and thermionic emission (no tunneling) is dominant when $E_{oo} << kT/q$.[19] The line in Figure 5.12 (a) is a fit of equation (5.14) to the data for the diode

ideality factor of the solar cell made with 65 nm thick ZnO without the TiO_2 buffer layer. The characteristic tunneling energy, E_{oo}, is 54 meV. This value is difficult to explain by invoking hole tunneling in Cu_2O as shown in path 2 in Fig. 5.11 and using bulk acceptor densities that are on the order of 10^{15} cm^{-3}. Estimate of E_{oo} with bulk properties of Cu_2O and using acceptor densities in the 10^{15} cm^{-3} range always yields values that are much smaller than 54 meV. Either there is a region of very high acceptor density near the Cu_2O-ZnO interfacial region or tunneling is on the ZnO side where the donor densities are higher. This would be consistent with Zhang et al.'s proposal[20] that the recombination current in Cu_2O-ZnO flows by tunneling of electrons from the ZnO conduction band into interfacial trap states (path 3 in Figure 5.11).

Figure 5.12 (b) shows the diode ideality factors for all solar cells listed in Table 1 as a function of temperature while they are under illumination. Under illumination, the diode ideality factors for solar cells made using 130 nm and 200 nm thick ZnO layers are independent of temperature indicating that tunneling is absent. Tunneling is still present in the solar cell made using thinner (65 nm) ZnO film. That presence of tunneling depends on the ZnO film thickness supports the previous conclusion that the tunneling is on the ZnO side. That the tunneling is eliminated under illumination is consistent with the proposal that the tunneling is into interfacial traps: under illumination interfacial traps are filled which would eliminate tunneling.

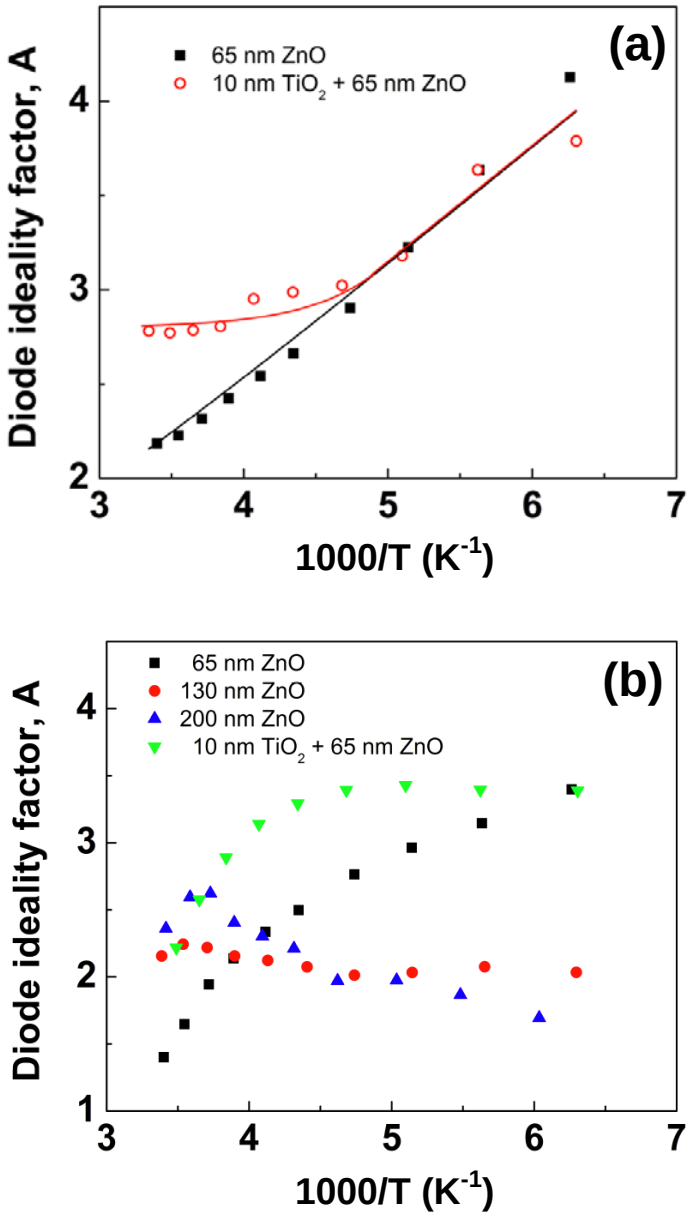

Figure 5.12. (a) Diode ideality factor versus reciprocal temperature for *J-V* characteristics acquired in the dark from solar cells made using 65 nm thick ZnO with and without a 10 nm thick TiO_2 buffer layer. The solid line for the solar cell without the buffer layer is a fit to equation (5.16). The solid line for the solar cell with the buffer layer is drawn to guide the eye. (b) Diode ideality factor versus reciprocal temperature for *J-V* characteristics acquired under 100 mW/cm^2 illumination from solar cells listed in Table 5.2.

5.5.3.3 Auger depth profile

It is well known that copper can diffuse readily even at low temperature. To evaluate possible metal interdiffusion at the ITO-ZnO and the Cu_2O-ZnO interfaces, the variation of Cu, Zn, and In throughout the solar cell film stack was measured using depth profiling by Auger spectroscopy. In this film the Cu_2O and ZnO film thicknesses were 280 nm and 65 nm respectively. Figure 5.13 shows the Cu, Zn and In depth profiles. The sputtering rate is material and composition dependent and no attempt was made to calibrate the sputtering rate. From the approximate locations of the interfaces and ex situ measurements of the film thickness, it was estimated that each sputtering cycle removes ~ 2.5 nm/cycle in Cu_2O and ~ 1.3 nm/cycle in ZnO. Clearly, there is significant interdiffusion of Zn and Cu at the Cu_2O-ZnO interface. The initial Cu_2O-ZnO interface seems to be where the maximum in the Zn and minimum in the Cu concentration occur. There could be preferential segregation at this interface and abundance of Zn due to the lattice mismatch and grain boundaries. While it may seem that the Cu is diffusing up a concentration gradient into ZnO this is likely due to differences in the partition coefficient for Cu in ZnO and Cu_2O, i.e., chemical potential gradients drive the diffusion of Cu into ZnO. Clearly, Cu diffuses all the way into ZnO and even ITO. The width of the transition region is ~ 25 cycles which corresponds to a thickness of ~50 nm much thicker than the roughness of the interface. Thus, the observed gradients are clearly due to diffusion and not due to interfacial roughness. Copper can be a p-type dopant and diffusion of Cu into ZnO can compensate the n-type ZnO film. On the other hand Zn is an n-type dopant in Cu_2O and can compensate the p-type film. This interdiffusion and compensation may be responsible for the low open circuit voltages observed in Cu_2O-

ZnO heterojunction solar cells.

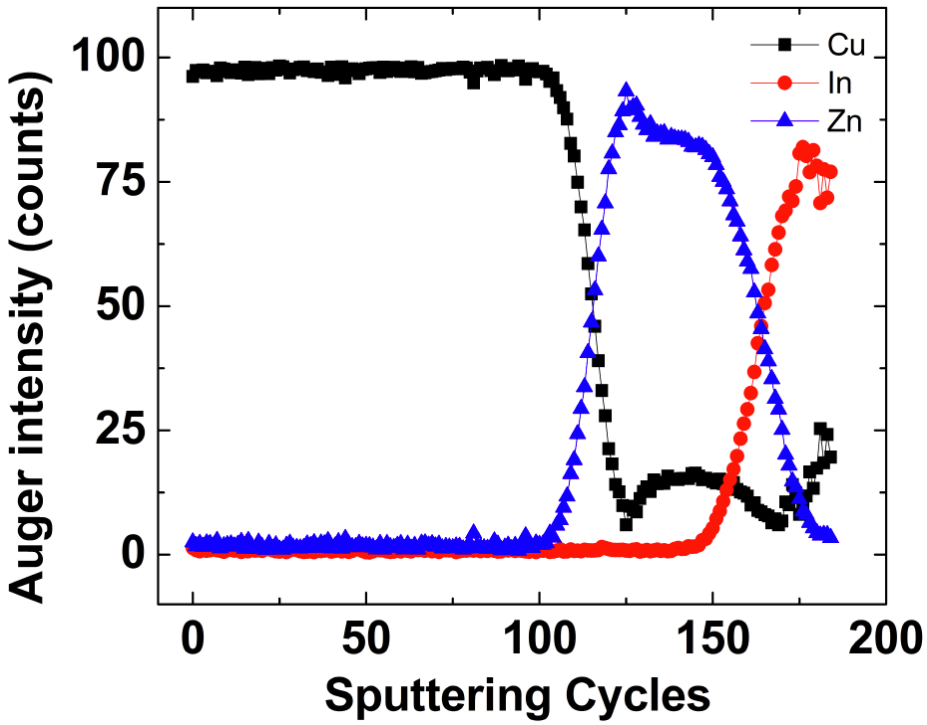

Figure 5.13. Copper, zinc and indium concentration profile measured using Auger depth profiling.

References

[1] A. Rothwarf, Sol. Cells **2**, 115 (1980).

[2] A. Kylner, J. Appl. Phys. **85**, 6858 (1999).

[3] G. Friesen, E. D. Dunlop, R. Wendt, Thin Solid Films **387**, 239 (2001).

[4] K. Leschkies, T. J. Beatty, M. S. Kang, D. Norris, E. S. Aydil, ACS Nano **3**, 3638 (2009).

[5] C. G. Walle, J. Phys. Condens. Matter. **20**, 064230 (2008).

[6] R. R. Potter, J. R. Sites, IEEE T. Electron Dev. **31**, 571 (1984).

[7] V. Nadenau, U. Rau, A. Jasenek, H. W. Schock, J. Appl. Phys. **87**, 584 (2000).

[8] M. Turcu, O. Pakma, U. Rau, Appl. Phys. Lett. **80**, 2598 (2002).

[9] S. S. Hegedus, J. Appl. Phys. **63**, 5126 (1988).

[10] M. -K. Han, P. Sung, W. A. Anderson, IEEE Elect. Dev. Lett. **EDL-3**, 121 (1982).

[11] A. Rose, Phys. Rev. **97**, 1538 (1955).

[12] V. Kumar, S. C. Jain, A. K. Kapoor, J. Poortmans, R. Mertens, J. Appl. Phys. **94**, 1283 (2003).

[13] P. Mark, W. Helfrich, J. Appl. Phys. **33**, 205 (1962).

[14] Richard H. Bube, *Photoelectronic Properties of Semiconductors* (Cambridge University Press, Cambridge, 1992) pp. 256.

[15] S. S. Jeong, A. Mittiga, E. Salza, A. Masci, S. Passerini, Electrochim. Acta **53**, 2226 (2008).

[16] H. Kobayashi, H. Mori, T. Ishida, Y. Nakato, J. Appl. Phys., **77**, 1301 (1995).

[17] Otfried Madelung, *Semiconductors : Data Handbook* (Springer, 3rd edition, 2004).

[18] F. A. Padovani, R. Stratton, Solid State Electronics, **9**, 695 (1966)

[19] A. Gumus, A. Turut, N. Yalcin, J. Appl. Phys., **91**, 254 (2002)

[20] D. K. Zhang, Y. C. Liu, Y. L. Liu, H. Yang, Physica B, **351**, 178-183 (2004).

Chapter 6

Summary and future direction

6.1 Summary

Among the metal oxides which exhibit a variety of functional properties depending on their crystal structure and bonding between the metal cation and oxygen, I focused on zinc oxide (ZnO) and cuprous oxide (Cu_2O). ZnO is always an n-type semiconductor either due to oxygen vacancies[1] or unintentional hydrogen incorporation,[2] and its wide band gap (~ 3.4 eV) makes it a suitable window layer in solar cells. On the other hand, Cu_2O always shows p-type conductivity, which is usually attributed to Cu vacancies.[3] The band gap of Cu_2O (~ 2.2 eV), its high absorption coefficient[4] and long minority carrier diffusion length,[5] make it an attractive absorber material in solar cells. In addition to their optical and electrical properties, the facts that they are benign environmentally, abundant on earth and cheap motivated this research to apply these materials for thin film solar cell applications.

The main topics of my research are (1) the properties of ZnO thin films deposited by metal organic chemical vapor deposition (MOCVD), plasma enhanced CVD (PECVD) and sputtering, (2) the properties of Cu_2O thin films deposited by MOCVD and (3) Cu_2O/ZnO heterojunction and solar cell applications.

ZnO thin films deposited by MOCVD from zinc acetylacetonate ($Zn(C_5H_7O_2)_2$, $Zn(acac)_2$) shows textured structure with $[0002]_{ZnO}$ parallel to the substrate normal on various substrates including amorphous glass, silicon, sapphire (a-plane). The film morphology is usually columnar with rough surface because of the anisotropic growth rate of ZnO $[(0001) > (10\bar{1}1) > (10\bar{1}0)]$. However, the ZnO films deposited on r-plane sapphire show epitaxy with $(11\bar{2}0)_{ZnO} \| (\bar{1}\bar{1}02)_{Al_2O_3}$ and $[0001]_{ZnO} \perp [11\bar{2}0]_{Al_2O_3}$ and the surface is smooth when deposited at low temperature (below 500˚C). X-ray diffraction (XRD) results show that the films deposited at high temperature (above 600˚C) have high quality (small full width half maximum (FWHM) of θ-2θ scan and rocking curve) but have poles grow out of surface. The films deposited at low temperature have stress to maintain the epitaxy but this stress is relieved by growing poles at high deposition temperature. These poles are suppressed by two step temperature deposition such that the films are grown at low temperature at first and then continued at high temperature.

ZnO films deposited by magnetron sputtering with undoped ZnO target have same textured structure ($[0002]_{ZnO}$ is parallel to substrate normal) as MOCVD. The grain size increases with oxygen partial pressure increase but the deposition rate reduces. Post annealing treatments such as thermal annealing and oxygen plasma exposure increases grain size and relieve film stress and this annealing effect is prominent in thin film case than thick film. From the investigation of the crystal structure dependence on annealing temperature, it was found that the film stress is not relieved below 150˚C and the annealing effect increases rapidly with temperature and saturated above 350˚C. The grain sizes also are not affected by annealing temperature below 150˚C and then increase

monotonously along with annealing temperature. The RMS roughness of films deposited at room temperature is ~ 3 nm and oxygen plasma has increases the roughness to ~ 8 nm. The electrical resistivity of films deposited at room temperature is above the limit of the measurement unit (~ 10^7 Ω-cm) and high deposition temperature (350˚C) reduces the resistivity by ~ 4 orders.

Cu_2O thin films were deposited on ZnO coated glass substrates by MOCVD using copper(II) hexafluoroacetylacetonate [$Cu(C_5HF_6O_2)_2$], oxygen gas and water vapor. The Cu_2O films are single phase with optical band gap, around 2 eV. XRD shows that Cu_2O thin films grow on ZnO with preferred $(220)_{Cu_2O} \parallel (0002)_{ZnO}$ orientation, textured structure on glass substrate. The grain size and stress of Cu_2O films increase with substrate temperature, and this structural property change results in the increase of electrical mobility. The property dependence on film thickness shows that grain size and film stress are inversely proportional to film thickness and as a result, mobility decrease. The Cu_2O films also has in-plane rotational alignment with the epitaxial relationship, $(220)_{Cu_2O} \parallel (0002)_{ZnO}$; $[001]_{Cu_2O} \parallel [1\bar{2}10]_{ZnO}$. Coincidence lattice model is invoked to explain this epitaxial relation.

Cu_2O/ZnO heterojunction thin film solar cells were fabricated based on MOCVD deposited Cu_2O and sputtered ZnO. The carrier transport and recombination mechanisms at the heterojunction were investigated by analyzing the temperature dependent *J-V* characteristics under dark and varying levels of illumination. The saturation current activation energies varied between 0.99 eV to 1.34 eV depending on how the solar cell was prepared. The activation energies are smaller than the band gap of Cu_2O (2.2 eV) and this reveals that interface recombination is the dominant carrier transport mechanism

in these solar cells. Tunneling plays an important role in interface recombination and tunneling characteristic energy is 54 meV. A buffer layer at the interface can reduce tunneling and improvements in the performance of Cu_2O/ZnO heterojunction solar cells will require suppression recombination and tunneling at the interface.

6.2 Future direction

The analysis of carrier transport mechanism through Cu_2O/ZnO heterojunction suggests that the suppression interface recombination and tunneling will improve the solar cell performance. Thin TiO_2 buffer layer shows an effect on reducing tunneling. Buffer layer at the junction interface can change the transport mechanism by passivating interface defects and modifying band alignment therefore, finding effective buffer layer in Cu_2O/ZnO heterojunction is important. The buffer layer should have appropriate electronic properties to make favorable band alignment and in this point of view, zinc sulfide (ZnS) can be a good candidate. Figure 6.1 shows the band diagram of Cu_2O, ZnS and ZnO. The smaller electron affinity and the larger band gap of ZnS than ZnO have a possibility to produce larger build-in potential at the interface between Cu_2O and ZnS because ZnS may have larger fermi-level difference with Cu_2O than ZnO. ZnS does not make any additional absorption loss of incident light compared to solar cells without ZnS. Because of the larger band gap of ZnS than ZnO, the illuminated light through ZnO layer will not be absorbed in ZnS layer. In addition to the electronic and optical properties, ZnS is also non toxic and cheap material therefore, it is a promising buffer layer for Cu_2O/ZnO heterojunction solar cell.

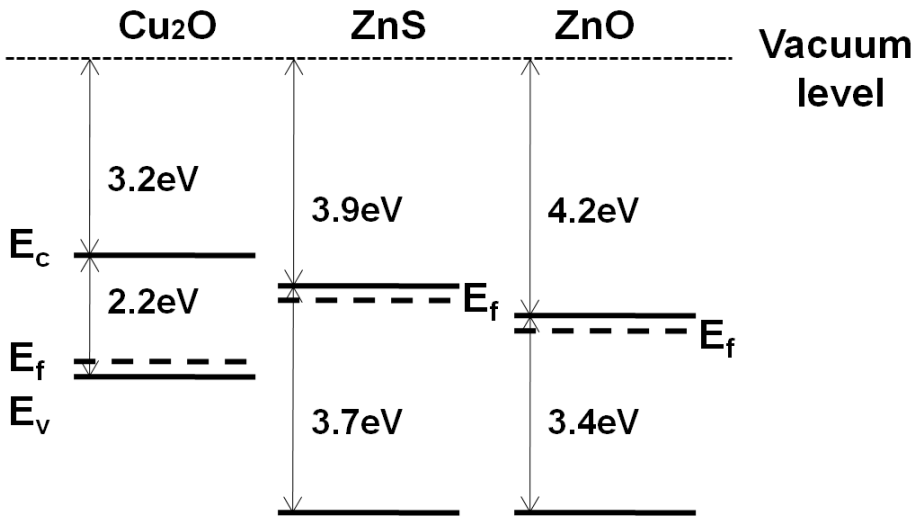

Figure 6.1. Band gap diagram of Cu_2O, ZnS and ZnO. E_c, E_f and E_v are the conduction band edge, fermi-level and valence band edge, respectively. The dopant binding energy is arbitrarily selected therefore the positions of E_f are arbitrary. The electron affinity and band gap of each materials are come from the references 6,7,8,9.

Solar cell performance can be improved by making use of nano-structure. The use of nano-structure provides several advantages for solar cells. First, nano-structure can improve light harvesting efficiency (LHE) because light scattering can be occurred within nano-structure and this may enhance the duration time of light in the material, hence light absorption can be increased. Recently, the improvement of light absorption in solar cells utilizing nano-structures (nano-wire, nano-dome etc.) is reported by several groups.[10,11,12] Second, carrier transport can be improved because nano-structures have large surface area compared to flat film which can enlarge junction interface areas. If the photogenerated current density is same, the nano-structured solar cell will produce larger

total current than flat film solar cell. Nano-structured solar cell based on Cu_2O/ZnO heterojunction is reported by a few groups.[13,14] Hsueh et. al. reported a nano-wire solar cell based on Cu_2O/ZnO heterojunction in which Cu_2O was deposited on ZnO nano-wires. Although they tried to make use of nano-wire, the deposited Cu_2O did not penetrate between the nano-wires and just stacked on top of the wire ends therefore Cu_2O film contacts ZnO only at the end of ZnO wire tips. In this structure, the cell cannot seem to make use of the full advantage of nano-structure. This may be due to the fact that they used sputtering to deposit Cu_2O on ZnO wire. The test deposition of Cu_2O by MOCVD on ZnO nano-wire shows that the deposited Cu_2O penetrated between wires as shown in Figure 6.2. Therefore, nano-structured Cu_2O/ZnO solar cell by CVD is a potential subject.

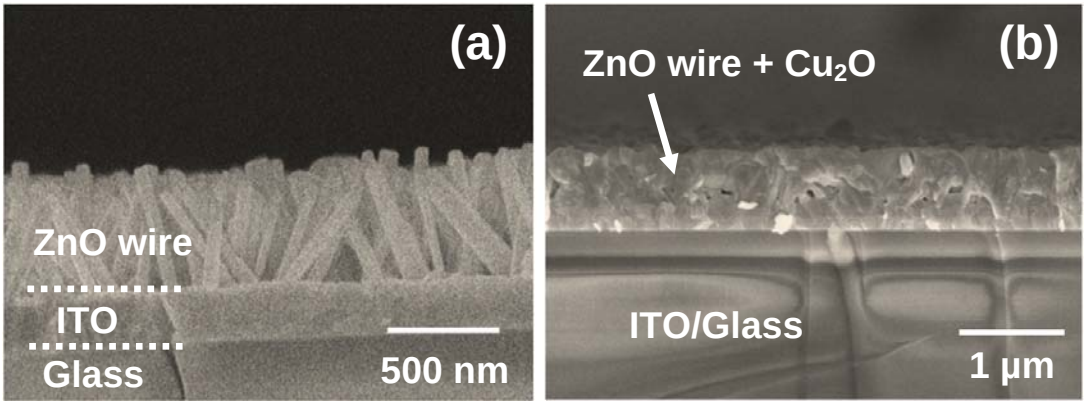

Figure 6.2. Cross sectional SEM image of ZnO nanowires grown on ITO coated glass substrate with and without Cu_2O film deposited by MOCVD. (a) is the ZnO nanowires grown on ITO glass before the Cu_2O deposition. (b) is the after the Cu_2O deposition.

References

[1] D. C. Look, J. W. Hemsky, J. R. Sizelove, Phys. Rev. Lett. **82**, 2552 (1999).

[2] Chris G. Van de Walle, Phy. Rev. Lett. **85**, 1012 (2000).

[3] M. Nolan, S. D. Elliott, Phys. Chem. Chem. Phys. **8**, 5350 (2006).

[4] A. E. Rakhshani, Solid-State Electronics, **29**, 7 (1986).

[5] C. A. Dimitriadis, L. Papadimitriou, N. A. Economou, J. Mater. Sci. Lett. **2**, 691 (1983).

[6] S. S. Jeong, A. Mittiga, E. Salza, A. Masci, S. Passerini, Electrochimica Acta **53**,226 (2008).

[7] H. Kobayashi, H. Mori, T. Ishida, Y. Nakato, J. Appl. Phys., **77**, 1301 (1995).

[8] Otfried Madelung, *Semiconductors : Data Handbook* (Springer, 3rd edition, 2004).

[9] M. M. Islam, S. Ishizuka, A. Yamada, K. Sakurai, S. Niki, T. Sakurai, K. Akimoto, Sol. Energ. Mat. Sol. C. **93**, 970 (2009).

[10] M. D. Kelzenberg, S. W. Boettcher, J. A. Petykiewicz, D. B. Turner-Evans, M. C. Putnam, E. L. Warren, J. M. Spurgeon, R. M. Briggs, N. S. Lewis, H. A. Atwater, Nat. Mater. **9**, 239 (2010).

[11] C. H. Peters, A. R. Guichard, A. C. Hryciw, M. L. Brongersma, M. D. McGehee, J. Appl. Phys. **105**, 124509 (2009).

[12] J. Zhu, C. Hsu, Z. Yu, S. Fan, Y. Cui, Nano lett. **10**, 1979 (2010).

[13] T. J. Hsueh, C. L. Hsu, S. J. Chang, P. W. Guo, J. H. Hsieh, I. C. Chen, Scripta Mater. **57**, 53 (2007).

[14] B. D. Yuhas, P. Yang, J. Am. Chem. Soc. **131**, 3756 (2009).

Bibliography

A. E. Rakhshani, Solid State Electron. **29**, 7 (1986).

A. Gumus, A. Turut, N. Yalcin, J. Appl. Phys. **91**, 254 (2002).

A. Kylner, J. Appl. Phys. **85**, 6858 (1999).

A. Mittiga, E. Salza, F. Sarto, M. Tucci, R. Vasanthi, Appl. Phys. Lett. **88**, 163502 (2006).

A. Ohtomo, A. Tsukazaki, Semicond. Sci. Tech. **20**, S1 (2005).

A. O. Musa, T. Akomolafe, M. J. Carter, Sol. Energ. Mat. Sol. C. **51**, 305 (1998).

A. Rose, Phys. Rev. **97**, 1538 (1955).

A. Trampert K. H. Ploog, Cryst. Res. Technol. 35, 793 (2000). A. Rothwarf, Sol. Cells **2**, 115 (1980).

B. Angadi, H. C. Park, H. W. Choi, J. W. Choi, W. K. Choi, J. Phys. D Appl. Phys. **40**, 1422 (2007).

B. Claflin, D. C. Look, S. J. Park, G. Cantwell, J. Cryst. Growth **287**, 16 (2006).

B. Cao, W. Cai, H. Zeng, G. Duan, J. Appl. Phys. **99**, 73516 (2006).

B. D. Yuhas, P. Yang, J. Am. Chem. Soc. **131**, 3756 (2009).

B. P. Rai, Sol. Cells **25**, 265 (1988).

B. P. Zhang, N. T. Binh, K. Wakatsuki, N. Usami, Y. Segawa, Appl. Phys. A **78**, 25 (2004).

B. S. Li, Y. C. Liu, Z. S. Chu, D. Z. Shen, Y. M. Lu, J. Y. Zhang, X. W. Fan, J. Appl. Phys. **91**, 501 (2002).

B. S. Li, Y. C. Liu, D. Z. Shen, Y. M. Lu, J. Y. Zhang, X. G. Kong, X. W. Fan, Z. Z. Zhi, J. Vac. Sci. Technol. A **20**, 265 (2002).

C. A. Dimitriadis, L. Papadimitriou, N. A. Economou, J. Mat. Sci. Lett. **2**, 691 (1983).

C. A. Wolden, T. M. Bames, J. B. Baxter, E. S. Aydil, J. Appl. Phys. **97**, 43522 (2005).

Chris G. Van de Walle, Phy. Rev. Lett. **85**, 1012 (2000).

C. G. Walle, J. Phys. Condens. Matter. **20**, 64230 (2008).

C. H. Bates, W. B. White, R. Roy, Science **137**, 993 (1962).

C. H. Peters, A. R. Guichard, A. C. Hryciw, M. L. Brongersma, M. D. McGehee, J. Appl. Phys. **105**, 124509 (2009).

C. N. R. Rao, B. Raveau, Transition Metal Oxides, Wiley-VCH, New York, 1998.

D. C. Kim, B. H. Kong, H. K. Cho, D. J. Park, J. Y. Lee, Nanotechnology **18**, 15603 (2007).

D. C. Look, Mat. Sci. Eng. B **80**, 383 (2001).

D. C. Look, J. W. Hemsky, J. R. Sizelove, Phys. Rev. Lett. **82**, 2552 (1999).

D. K. Zhang, Y. C. Liu, Y. L. Liu, H. Yang, Physica B, **351**, 178-183 (2004).

David P. Norton, Mater. Sci. Eng. R **43**, 139 (2004).

E. Mirica, G. Kowach, P. Evans, H. Du, Cryst. Growth Des. **4**, 147 (2004).

F. A. Padovani, R. Stratton, Solid State Electronics **9**, 695 (1966).

G. Friesen, E. D. Dunlop, R. Wendt, Thin Solid Films **387**, 239 (2001).

G. G. condorelli, G. Malandrino, I. Fragala, Chem. Mater. **6**, 1861 (1994).

G. P. Pollack, D. Trivich, J. Appl. Phys. **46**, 163 (1975).

G. Xiong, J. Wilkinson, B. Mischuck, S. Tuzemen, K. B. Ucer, R. T. Williams, Appl. Phys. Lett. **80**, 1195 (2002).

H. Kobayashi, H. Mori, T. Ishida, Y. Nakato, J. Appl. Phys. **77**, 1301 (1995).

H. Karzel, W. Potzel, M. Köfferlein, W. Schiessl, M. Steiner, U. Hiller, G. M. Kalvius, D. W. Mitchell, T. P. Das, P. Blaha, K. Schwarz, M. P. Pasternak, Phys. Rev. B **53**, 11425 (1996).

H. Raebiger, S. Lany, A. Zunger, Phys. Rev. B **76**, 45209 (2007).

H. Tanaka, T. Shimakawa, T. Miyata, H. Sato, T. Minami, Thin Solid Films **469-470**, 80 (2004).

I. Volintiru, M. Creatore, B. J. Kniknie, C. I. M. A. Spee, M. C. M. Sanden, J. Appl. Phys. **102**, 43709 (2007).

J. B. Baxter, E. S. Aydil, J. Cryst. Growth **274**, 407 (2005).

J. B. Mooney, S. B. Radding, Annu. Rev. Mater. Sci. **12**, 81 (1982).

J. F. Wager, Science **300**, 1245 (2003).

J. Herion, E. A. Niekisch, G. Scharl, Sol. Energ. Mater. **4**, 101 (1980).

J. H. Park, S. J. Jang, S. S. Kim, B. T. Lee, Appl. Phys. Lett. **89**, 121108 (2006).

J. J. Loferski, J. Appl. Phys. **27**, 777 (1956).

J. Q. Xie, J. W. Dong, A. Osinsky, P. P. Chow, T. W. Heo, D. P. Norton, S. J. Pearton, X. Y. Dong, C. Adelmann, C. J. Palmstrom, Mater. Res. Soc. Symp. P. **891**, 407 (2006).

J. Ramirez-Ortiz, T. Ogurab, J. Medina-Valtierra, S. E. Acosta-Ortiz, P. Bosch, J. A. de los Reyes, V. H. Lara, Appl Surf. Sci. **174**, 177-184 (2001).

J. Zhu, C. Hsu, Z. Yu, S. Fan, Y. Cui, Nano lett. **10**, 1979 (2010).

K. Akimoto, S. Ishizuka, M. Yanagita, Y. Nawa, G. K. Paul, T. Sakurai, Sol. Energy **80**, 715 (2006).

K. Ellmer, G. Vollweiler, Thin Solid Films **496**, 104 (2006).

K. Ellmer, J. Phys. D Appl. Phys. **33**, R17 (2000).

K. Ellmer, J. Phys. D. Appl. Phys. **34**, 3097 (2001).

K. Koike, I. Nakashima, K. Hashimoto, S. Sasa, M. Inoue, M. Yano, Appl. Phys. Lett. **87**, 112106 (2005).

K. Leschkies, T. J. Beatty, M. S. Kang, D. Norris, E. S. Aydil, ACS Nano **3**, 3638 (2009).

L. C. Olsen, F. W. Addis, W. Miller, Sol. Cells **7**, 247 (1982-1983).

L. Papadimitriou, N. A. Economou D. Trivich, Sol. Cells **3**, 73 (1981).

L. T. Drapak, Semiconductors **2**, 624 (1968).

M. Chen, Z. L. Pei, C. Sun, J. Gong, R. F. Huang, L. S. Wen, Mater. Sci. Eng. B **85**, 212 (2001).

M.Chen, Z. L. Pei, X. Wang, C. Sun, L. S. Wen, J. Vac. Sci. Technol. A **19**, 963 (2001).

M. Chen, Z. L. Pei, X. Wang, Y. H. Yu, C. Sun, L. S. Wen, J. Phys. D Appl. Phys. **33**, 2538 (2000).

M. D. Kelzenberg, S. W. Boettcher, J. A. Petykiewicz, D. B. Turner-Evans, M. C. Putnam, E. L. Warren, J. M. Spurgeon, R. M. Briggs, N. S. Lewis, H. A. Atwater, Nat. Mater. **9**, 239 (2010).

M. Izaki, T. Shinagawa, K. Mizuno, Y. Ida, M. Inaba, A. Tasaka, J. Phys. D Appl. Phys. **40**, 3326 (2007).

M. K. Han, P. Sung, W. A. Anderson, IEEE Elect. Dev. Lett. **EDL-3**, 121 (1982).

M. Kim, Y. Hong, J. Yoo, G. Yi, G. Park, K. Kong, H. Chang, Phys. Stat. Sol. (RR) **2**, 197 (2008).

M. Liu, H. K. Kim, Appl. Phys. Lett. **84**, 173 (2004).

M. M. Islam, S. Ishizuka, A. Yamada, K. Sakurai, S. Niki, T. Sakurai, K. Akimoto, Sol. Energ. Mat. Sol. C. **93**, 970 (2009).

M. Nolan, S. D. Elliott, Phys. Chem. Chem. Phys. **8**, 5350 (2006).

M. Ohring, Materials Science of thin films, Academic press, USA, 2002.

M. Turcu, O. Pakma, U. Rau, Appl. Phys. Lett. **80**, 2598 (2002).

N. Tsuji, H. Komiyama, K. Tanaka, J. J. Appl. Phys. **29**, 835 (1990).

Otfried Madelung, Semiconductors : Data Handbook, Springer, 3rd edition, 2004.

P. Kung, C. J. Sun, A. Saxler, H. Ohsato, M. Razeghi, J. Appl. Phys. **75**, 4515 (1994).

P. Mark, W. Helfrich, J. Appl. Phys. **33**, 205 (1962).

Q. Ma, Z. Ye, H. He, L. Zhu, J. Wang, B. Zhao, Mater. Lett. **61**, 2460 (2007).

R. G. Gordon, MRS Bull. **52**, August (2000).

R. G. Gordon, Mater. Res. Soc. Symp. P. **426**, 419 (1996).

Richard H. Bube, Photoelectronic Properties of Semiconductors (Cambridge University Press, Cambridge, 1992) pp. 256.

R. L. Hoffman, B. J. Norris, J. F. Wager, Appl. Phys. Lett. **82**, 733 (2003).

R. R. Potter, J. R. Sites, IEEE T. Electron Dev. **31**, 571 (1984).

R. Swanepoel, J. Phys. E Sci. Instrum. **16**, 1214 (1983).

R. Triboulet, 10th European Workshop on MOVPE, Lecc (Italy) 11 Aug June (2003).

R. T. Downs, K. L. Bartelmehs, G. V. Gibbs, Am. Mineral. **78**, 1104 (1993).

S. Brehme, F. Fenske, W. Fuhs, E. Nebauer, M. Poschenrieder, B. Selle, I. Sieber, Thin Solid Films **342**, 167 (1999).

S. B. Krupanidhi, M. Sayer, J. Appl. Phys. **56**, 3308 (1984).

Satischandra B. Ogale, Thin films and Heterostructures for oxide electronics, Chapter 10, 303 (Springer, 2005).

S. Ishizuka, K. Suzuki, Y. Okamoto, M. Yanagita, T. Sakurai, K. Akimoto, N. Fujiwara, H. Kobayashi, K. Matsubara, S. Niki, Phys. Status. Solidi. **1**, 1067 (2004).

S. Ishizuka, S. Kato, Y. Okamoto, K. Akimoto, Appl. Phys. Lett. **80**, 950 (2002).

S. Ishizuka, S. Kato, Y. Okamoto, K. Akimoto, J. Cryst. Growth **237**, 616 (2002).

S. J. Pearton, W. H. Heo, M. Ivill, D. P. Norton, T. Steiner, Semicond. Sci. Tech. **19**, R59-R74 (2004).

S. S. Hegedus, J. Appl. Phys. **63**, 5126 (1988).

S. S. Jeong, A. Mittiga, E. Salza, A. Masci, S. Passerni, Electrochim. Acta. **53**, 2226 (2008).

T. ITO, H. Yamaguchi, K. Okabe, T. Masumi, J. Mater. Sci. **33**, 3555 (1998).

T. J. Hsueh, C. L. Hsu, S. J. Chang, P. W. Guo, J. H. Hsieh, I. C. Chen, Scripta Mater. **57**, 53 (2007).

T. Minami, MRS Bull. **38**, August (2000).

T. Minami, T. Miyata, K. Ihara, Y. Minamino, S. Tsukata, Thin Solid Films **494**, 47 (2006).

U. Ozgur, Ya. I. Alivov, C. Liu, A, Teke, M. A. Reshchikov, S. Dogan, V. Avrutin, S. J. Cho, H. Morkoc, J. Appl. Phys. **98**, 41301 (2005).

V. Kumar, S. C. Jain, A. K. Kapoor, J. Poortmans, R. Mertens, J. Appl. Phys. **94**, 1283 (2003).

V. Nadenau, U. Rau, A. Jasenek, H. W. Schock, J. Appl. Phys. **87**, 584 (2000).

V. Tvarozek, K. Shtereva, I. Novotny, J. Kovac, P. Sutta, R. Srnanek, A. Vincze, Vacuum **82**, 166 (2008).

W. Shockley, H. J. Queisser, J. Appl. Phys. **32**, 510 (1961).

W. Y. Ching, Y. N. Xu, K. W. Wong, Phys. Rev. B **40**, 7684 (1989).

Y. Chen, D. M. Bagnall, H. Koh, K. Park, K. Hiraga, Z. Zhu, T. Yao, J. Appl. Phys. **84**, 3912 (1998).

Y. J. Kim, H. J. Kim, Mater. Lett. **21**, 351 (1994).

Y. Nakano, S. Saeki, T. Morikawa, Appl. Phys. Lett. **94**, 22111 (2009).

Y. W. Heo, S. J. Park, K. Ip, S. J. Pearton, D. P. Norton, Appl. Phys. Lett. **83**, 1128 (2003).

Z. Li, W. Gao, Mater. Lett. **58**, 1363 (2004).